The Pennsylvania State University

The Graduate School

College of Earth and Mineral Sciences

SYNTHESIS AND CHARACTERIZATION OF NICKEL MANGANITE THIN FILMS FOR APPLICATION IN UNCOOLED MICROBOLOMETERS

A Thesis in

Materials Science and Engineering

by

Heidi M. Schulze

© 2008 Heidi M. Schulze

Submitted in Partial Fulfillment
of the Requirements
for the Degree of

Masters of Science

August 2008

The thesis of Heidi M. Schulze was reviewed and approved* by the following:

Susan E. Trolier-McKinstry
Professor of Ceramic Science and Engineering
Thesis Adviser

Mark W. Horn
Associate Professor of Engineering Science

Elizabeth C. Dickey
Professor of Materials Science and Engineering

Tom N. Jackson
Robert E. Kirby Chair
Professor of Electrical Engineering

Joan M. Redwing
Professor of Materials Science and Engineering
Associate Head for Graduate Studies, Materials Science and Engineering

*Signatures are on file in the Graduate School.

ABSTRACT

The nickel manganite thermistor thin films were studied as potential candidates for application in uncooled microbolometers, where low temperature processing, high TCR coupled with low noise, and property stability of the material are required. The phase formation within the nickel manganite materials system was studied with respect to annealing conditions (air, argon, oxygen, and engineered low pO_2 from residual organics) through the synthesis of chemical solution deposited (acetate and acetylacetonate-based solutions) thin films over a wide range of compositions (Mn/Mn+Ni = 0.14 to 0.9) and temperatures (300 to 1030°C). Thin films were structurally characterized using X-ray diffraction and transmission electron microscopy (TEM) analysis and electrically characterized through determination of the temperature coefficient of resistance (TCR), resistivity, and activation energy.

It has been shown that reducing atmospheres favor the spinel phase at low temperatures, while oxygen is required to crystallize thermodynamically stable phases with higher oxidation states on the Mn. The annealing atmospheres can be controlled either globally (via the furnace ambient) or locally (by leaving residual organics following the pyrolysis step) to control phase formation.

Low temperature synthesis of the thermistor films is important to enable compatibility of the material with CMOS integration. Single-phase metastable cubic spinel films (Mn/Mn+Ni = 0.5 to 0.8) annealed in argon at 400°C for 5 hours exhibit TCR values ranging from -3.8 to -4.5 %/K and resistivity values on the order of 10,000 Ωcm. Metastable spinel films show excellent stability when heat-treated at 400°C for long times.

Cubic spinel was also formed above 730°C with comparable properties to the bulk, including TCR values between -3.3 and -4.5 %/K and resistivities around 1000 Ωcm. The small lattice parameters of the films indicate a cation-deficient spinel structure. Due to the low processing temperatures possible, dense films could be prepared within the spinel phase field. Thus, decomposition into the NiO phase and a Mn – rich spinel, which is problematic in bulk ceramics, will not occur in such spinel thin films. For films prepared outside of the single-phase field, phase separation cannot always be detected using X-ray diffraction (due to the possibility of coherent straining or to the very small crystallite size). In such cases, transmission electron microscopy was useful in identifying decomposition.

Single-phase spinel films (TCR = -3.6 to -4.1 %/K) were compared to single-phase bixbyite films (TCR = -3.1 to -3.3 %/K) synthesized between 630°C and 930°C. The bixbyite phase exhibits lower TCR and lower resistivity, 400-1600 Ωcm, compared to spinel, 3500-21,000 Ωcm. Composite films (achieved by controlling the pyrolysis to create a low local pO_2) during annealing exhibit intermediate values (TCR = -3.0 to -3.8 %/K and resistivity = 470-6600 Ωcm).

TABLE OF CONTENTS

Page

LIST OF FIGURES

Page

LIST OF TABLES

ACKNOWLEDGEMENTS

I would like to thank Hideki Ogihara and Ichiro Fujii for countless translations, Raja Bharadwaja for helping me with electrical measurements, Nik Podraza for assisting with the spin-spray equipment, Jing Lee and David Saint-John for TEM analysis, Raegan Johnson for ordering chemicals and a positive attitude, Pum Bintachitt for always asking when will I defend, Dan Tinberg for answering many questions, Song Won Ko and Jackie Lee for teaching me the sol-gel method, Mark Angelone for FESEM training, Maria Klimkiewicz for always being willing to assist in SEM focusing, Nichole Wonderling for helping with the XRD machines, Tim Klinger for numerous repairs, everyone at MRL, the STM group, my parents and friends for their support, and especially Dr. Susan Trolier-McKinstry for her insightfulness and encouragement.

This research was sponsored by the U.S. Army Research Office and U.S. Army Research Laboratory and was accomplished under Cooperative Agreement Number W911NF-0-2-0026. The views and conclusions contained in this document are those of the authors and should not be interpreted as representing the official policies, either expressed or implied, of the Army Research Office, Army Research Laboratory, or the U.S. Government. The U.S. Government is authorized to reproduce and distribute reprints for Government purposes notwithstanding any copyright notation hereon.

Chapter 1

INTRODUCTION TO THE THESIS

1.1 Background

Different negative temperature coefficient of resistance materials are currently being used to fabricate uncooled microbolometer focal plane arrays (FPA) for IR (infrared) detection devices such as night-vision goggles, infrared cameras, and heads-up displays in vehicles. Materials include vanadium oxides (VO_x), polycrystalline silicon (Si), amorphous silicon (α-Si), polycrystalline silicon germanium (SiGe), and amorphous silicon carbide (α-SiC_x) [1, 2]. Alternative material systems with improved properties, simpler processing, and compatibility with well-developed fabrication methods are being investigated. This thesis focuses on the processing and characterization of multicomponent nickel manganese oxides as candidate microbolometer materials.

Materials with either positive or negative temperature coefficients of resistance (PTC or NTCR, respectively) can be used as temperature sensors. For example, nickel manganite ceramics with the spinel crystal structure are extensively utilized as bulk thermistors. Nickel manganite spinels have a high temperature coefficient of resistance (TCR) and reasonably low resistivities (10s to 10000s Ωcm) [3, 4]. Its TCR (-2 to -6.5 %/K) exceeds those of the vanadium oxides (~ -2 %/K), α-Si (-2 to -3 %/K), and SiGe alloys (-2 to -4 %/K) [2, 4, 5, 6]. Bulk manganite perovskite structured materials have also been investigated for NTC thermistor applications [7, 8]. TCR values for $YNi_xMn_{1-x}O_3$ ceramics, where x = 0.4-0.5, range between -3.9 %/K and -5 %/K with corresponding resisitivities between 1400 and 42000 Ωcm [7]. Doping yttrium manganite ($YMnO_3$) with iron produces NTC materials with higher resistivities, 4000 to $1x10^9$ Ωcm [8]. In contrast, yttrium barium copper oxide (YBCO = $YBa_2Cu_3O_7$) is a PTC material that is used in cooled bolometers because of its superconducting transition [5]. Likewise, PTC thermistors based on ferroelectrics such as $BaTiO_3$ are also known [6]. The nickel manganite system is sensitive at room temperature and has a high TCR, making it an excellent candidate for further investigation into use in uncooled microbolometer applications.

1.2 Thesis Objectives

The primary goal of this thesis was to determine if a nickel manganite spinel thin film is a viable candidate to act as the detector material for an uncooled infrared microbolometer. From a technological standpoint, there are several key parameters that had to be determined to make such an assessment: the achievable TCR and resistivity, the noise, the required processing temperature (which is desired to be low in order to be compatible with CMOS, complementary metal-oxide semiconductor, integration), and property stability. Thus, in thin film form, the electrical properties, including TCR, resistivity, and activation energy were compared to the bulk as well as other IR detection material systems. Different processing routes were examined. The aging of the films was also studied to examine the stability over time and through heat treatments. Scientifically, the primary goals were to determine the structure-composition-property-processing relationships that controlled the observed behavior.

Chapter 2

LITERATURE REVIEW

2.1 Infrared Detection

2.1.1 Application

IR (infrared) detection technology is employed in a wide range of applications in a variety of areas, from medical to military to manufacturing. Radiation can be detected either quantitatively or qualitatively. Radiometry is the quantitative determination of the absolute amount of radiation present via temperature (pyrometry) or as a spectral distribution (spectroscopy). Thermal imaging, on the other hand, typically relies on qualitative detection of radiation, in which images are obtained using thermal contrast [1].

Applications of thermal imaging systems are vast. Situations that can be readily improved by thermal imaging include driver awareness at night or in foggy conditions, and firefighting. Military applications include battlefield surveillance, minefield detection, missile location, and camouflage detection. In the medical field, IR detection can be used to analyze blood flow, observe muscular functions for physical therapy, image wounds or burns, determine body temperature, or locate tumors. Industrial applications include monitoring equipment, circuit boards, piping, furnaces, insulation coverage, and more [1].

2.1.2 Detectors

A radiation detector must have the ability to convert the energy associated with incident electromagnetic radiation into an electrical signal. There are two main types of detectors that can be classified by their operating mechanisms: photon and thermal detectors. Photon detectors depend on the wavelength of the incident radiation [9]. Thermal detectors are wavelength independent because the signal does not depend on the photon nature of the radiation [9]. Most photon detectors require a cooling system, especially when used to detect long wavelengths (>3 μm), while most thermal detectors operate at room temperature even for far IR radiation [9]. The cooling of detectors reduces thermal generation of charge carriers, but adds to the system bulk and weight, and tends to increase system cost [9, 10].

2.1.2.1 Photon Detectors

A photon detector, also known as a quantum detector, is based on the direct interaction between photons and electrons in the semiconducting material [10]. Radiation is absorbed into the material through interaction with electrons. The interactions can either be with electrons bound to lattice atoms, bound to impurity atoms, or with free electrons. The optical excitation causes a change in the electronic energy distribution, which allows for different electrical outputs depending on the amount of radiation. For an intrinsic photon detector, photons are absorbed to create electron – hole pairs if their energy is greater than that of the band gap. The production of the electron – hole pairs changes the electrical conductivity. Examples of materials that exhibit this behavior include PbS, InSb, and $Hg_{1-x}Cd_xTe$. In an extrinsic detector, an impurity is present in the band gap and the electron is excited from within the band gap to the conduction band. Extrinsic materials and their impurities include Si:In, Si:Ga, Ge:Cu, and Ge:Hg. Alternatively, the photoemission effect can be used in Schottky barrier detectors. The movement of electrons between a semiconductor to a metal causes the Fermi levels of the metal and the semiconductor to line up, creating a potential barrier or a Schottky barrier. The potential barrier is used to detect photons that have energy lower than that of the band gap of the semiconductor. Materials include PtSi and IrSi [9].

2.1.2.2 Thermal Detectors

The IR thermal detector works on the concept that the absorbed radiation changes the temperature of the material, which in turns changes a physical property of the material. The detector consists of two main physical parts, the radiation absorber and the temperature sensor. The absorber converts the incident radiant flux, ϕ_s, into heat, and is characterized by a thermal impedance, $\mathscr{L}_{th}$; Equation 2.1 shows the thermal impedance, which has units of [K/W]. It is a function of the temperature difference between the detector and the surroundings, T_d, measured in either degrees Kelvin or Celcius [K or °C] and radiant flux, measured in watts [W] [1].

$$\mathscr{L}_{th} = T_d/\phi_s \qquad \text{Equation 2.1}$$

The transducer is characterized by its thermal responsivity, $\mathscr{R}_{th}$. Its function is to convert the heat absorbed by the probe into a measurable quantity. Equation 2.2 shows that the responsivity [V/K] is a function of the output voltage, measured in volts [V] and the temperature difference between the detector and the surroundings, T_d [K or °C] [1].

$$\mathscr{R}_{th} = V/T_d \qquad \text{Equation 2.2}$$

Absorption of the radiation causes the detector element to experience a temperature change, which in turn causes one of the physical characteristics of the component to vary, such as resistance in the case of thermistors. Types of thermal detectors include thermocouples, thermopiles, pyroelectric detectors, and resistive or capacitive bolometers [1].

Thermocouples are temperature sensors that consist of two electrically conductive materials that are combined at two junctions to form a circuit. A voltage is produced at each junction and the potential difference can be measured as a function of temperature. One junction is kept cold as a reference while the other acts as the probe and is called the hot junction. This detector demonstrates the Seebeck effect. The electrical potential depends on the two types of conductive material used and the temperature difference between the two joints. Thermopiles consist of many thermocouples connected in series. Among the materials used in thermocouples are nickel, antimony, bismuth, chromium, copper, silver, tellurium, platinum, and their alloys [1, 11].

Pyroelectric detectors use a ferroelectric material that exhibits a spontaneous polarization whose value is a function of temperature [1]. Pyroelectric detector materials include lead zirconate titanate, $Ba_{1-x}Sr_xTiO_3$, as well as several of the tungsten bronzes [12].

Resistive bolometers are based on the concept that in an electrically conductive material, temperature determines the concentration and/or the mobility of carriers [1]. There are two types of bolometer detectors, the metal strip bolometer and the thermistor bolometer [11]. The radiation sensitive materials include pure metals, such as nickel or platinum for the metal strip detectors and semiconducting metal oxides for thermistor bolometers. Metal bolometers have a positive temperature coefficient (PTC) of about 0.3 to 0.4 %/K [11]. The metal strips must be very thin in order to have a minimal heat capacity. Thermistor bolometers are typically made from a semiconducting thin film. Manganese, nickel, vanadium, and cobalt oxide compounds, or amorphous silicon or silicon germanium usually make up the IR sensing element. Thermistor materials usually have high negative temperature coefficients (NTCs) around – 1 %/K to – 4 %/K [11].

A microbolometer refers to a device that is fabricated by micromachining in order to create the micron-sized pixel structure that makes up a focal plane array (FPA) [13]. It consists of three main parts: a detector, the supports, and read-out circuitry. The detector membrane's function is to absorb incident radiation and heat a temperature sensitive material. The membrane must be thermally isolated from the read-out circuitry below. To optimize the absorption of the incident radiation, a reflective metallic layer is often deposited onto the surface of the (appropriately isolated) read-out circuitry [1].

Membrane supports are necessary after the removal of the sacrificial layer. Often, the membrane is supported between two metallic legs. A microbridge structure is created as shown in Figure 2.1.

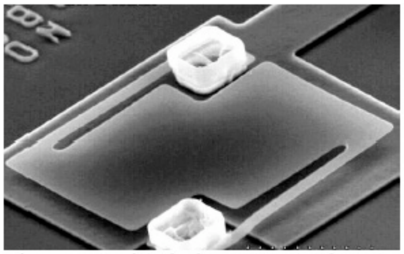

Figure 2.1: A single pixel (48 μm x 48 μm) from an α:Si microbolometer FPA [Source: A. J. Syllaios, T. R. Schimert, R. W. Gooch, W. L. McCardel, B. A. Ritchey, J. H. Tregilgas. "Amorphous Silicon Microbolometer Technology," Mat. Res. Soc. Symp. Proc. 609 (2000): A14.4.1-A14.4.6.]

The read-out circuitry is typically CMOS. The purpose of the circuitry is to measure the variation in resistance as a potential is applied across the electrodes. For many cameras, each microbridge structure is about 50x50 μm. A lithographic resolution of a micron is required. The whole structure is typically packaged to provide a vacuum enclosure to minimize thermal losses by convection [1]. Figure 2.2 shows an array on a silicon wafer.

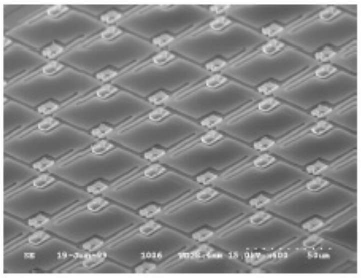

Figure 2.2: α:Si FPA created on a silicon wafer (a single pixel is 48 μm x 48 μm) [Source: A. J. Syllaios, T. R. Schimert, R. W. Gooch, W. L. McCardel, B. A. Ritchey, J. H. Tregilgas. "Amorphous Silicon Microbolometer Technology," Mat. Res. Soc. Symp. Proc. 609 (2000): A14.4.1-A14.4.6.]

There are both cryogenically cooled and uncooled FPAs. The uncooled are much lower in cost and simpler in design. Typical materials used in cooled FPA include $Hg_{1-x}Cd_xTe$ (mercury cadmium telluride) and InSb (indium antimony) [15].

As shown from the emission spectrum in Figure 2.3, for an infrared detector to be able to detect objects near room temperature, it must be sensitive in the 8-14 μm wavelength range. A room temperature object begins to radiate at 2 μm and peaks at about 10 μm.

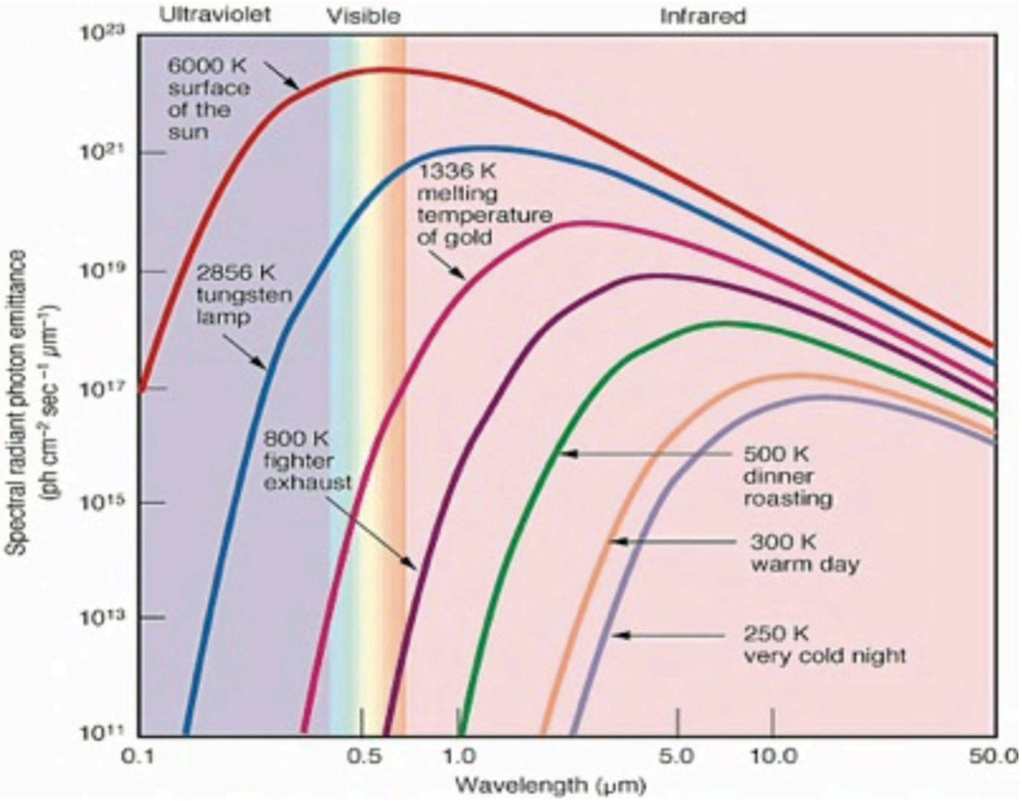

Figure 2.3: Electromagnetic radiation spectra from a blackbody over the wavelength range from 0.1-50 μm [Source: MICRO-EPSILON <www.micro-epsilon.us/>.]

2.2 Thermistor Materials

Thermistors are temperature sensitive resistors and are characterized by their TCR values. TCR values may be positive (PTC) or negative (NTC). NTCs usually show a more gradual change in resistance over a broader range in temperature compared to PTCs [10]. The TCR is measured in %/K and is defined in Equation 2.8 as the ratio of the rate of change in resistance with respect to temperature to the resistance at a specific temperature [4].

$$\text{TCR} = \alpha = 1/R^{*}dR/dT \qquad \text{Equation 2.8}$$

R_1 is usually measured at 25°C and R_2 is measured at a temperature between 50°C and 100°C [4]. In this study, NTC thermistors were explored for uncooled thermal sensors.

The first NTC material discovered was Ag_2S, as reported by Faraday in 1833. In the 1930's oxide materials including Fe_3O_4 were shown to possess a characteristic large NTCR. Later in that decade the range of NTC oxides expanded to NiO and CoO, then to multicomponent oxide systems such as $NiO\text{-}Co_2O_3\text{-}Mn_2O_3$ and $NiO\text{-}Mn_2O_3$ [4]. Researchers at Philips in Holland explained the mechanism responsible for the change in resistivity with temperature in semiconducting oxides [4]. Bell Telephone Laboratories began the initial development of a thermistor detector [11]. Thermistors made their first appearance as a commercial product at the end of World War II as sensors in temperature measurement devices and as automatic regulators of electrical signals in circuits [17]. Bulk thermistors were two-terminal semiconductor devices as shown in Figure 2.4.

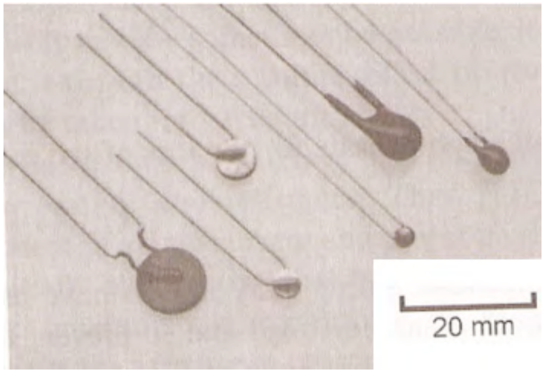

Figure 2.4: Bulk NTC thermistors [Source: R. C. Buchanan. Ceramic Materials for Electronics 3rd Ed. New York: Marcel Dekker, 2004.]

Most of the commercial NTC materials are now based on mixed oxide compounds with the spinel structure, such as Fe_3O_4-$ZnCr_2O_4$, Fe_3O_4-$MnCr_2O_4$ or manganese oxides with Ni, Co, or Cu [6].

2.2.1 The Spinel Structure

The spinel structure (AB_2O_4) is named for the mineral spinel, $MgAl_2O_4$. This structure consists of two main types of cubic building blocks within the unit cell, rocksalt-like and diamond-like, which leads to cation occupancy of both tetrahedral (AO_4) and octahedral (BO_6) sites as shown in Figure 2.5.

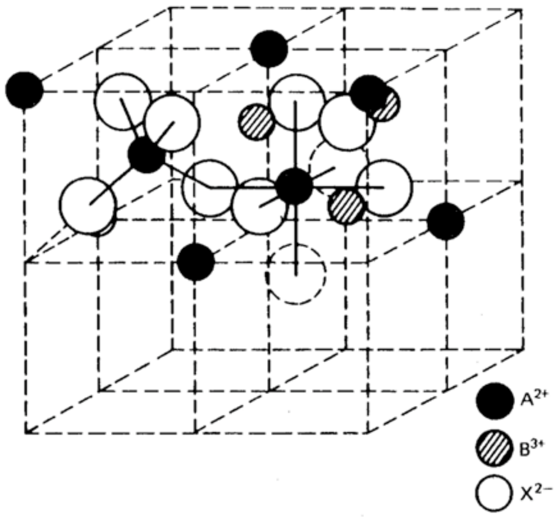

Figure 2.5: The cubic spinel crystal structure [Source: R. C. Buchanan. Ceramic Materials for Electronics 3rd Ed. New York: Marcel Dekker, 2004.]

The unit cell can be divided into eight building blocks, four of each, which alternate. The oxygen ions form a cubic close-packed structure. The cation occupancy defines whether a given material with the spinel structure will be normal, inverse, or disordered. In a normal spinel, the 2^+ ions (A) sit on the tetrahedral sites while the 3^+ ions (B) occupy the octahedral sites. In the inverse spinel, equal amounts of 2^+ and 3^+ ions sit on the octahedral sites while the remaining 3^+ ions sit on the tetrahedral sites [18]. The mineral spinel, $MgAl_2O_4$ has a normal structure, while $NiFe_2O_4$ could be written $Fe(NiFe)O_4$, (where the parentheses denote the octahedral sites) to show that it has the inverse structure [4]. There are also spinels that are partially inverse [4]. $MnFe_2O_4$ can be written as $Mn^{2+}{}_{0.8}Fe^{3+}{}_{0.2}(Mn^{2+}{}_{0.2}Fe^{3+}{}_{1.8})O_4$; clearly it lies in between an inverse and a normal arrangement [4]. In this intermediate structure 8/10 of all the Mn^{2+} cations sit on tetrahedral sites and 2/10 occupy octahedral sites [4]. The amount of inversion present in the structure can be defined as ν, known as the degree of inversion [19]. A value of 1 for the degree of inversion represents a structure that is completely inverse. A value of 0 would represent a structure that is normal. $\nu = 0.2$ in $MnFe_2O_4$ so it is 20% inverse [4].

2.2.2 Conduction in Nickel Manganite

In nickel manganites, it is believed that the conduction results from thermally activated hopping [20, 21]. The electrical conduction is associated with the transfer of charge *and* a lattice distortion between the multivalent manganese ions, Mn^{3+} and Mn^{4+}, located on equivalent octahedral sites in the spinel lattice [20, 22, 23]. The combination of charge transfer and the lattice distortion (or surrounding polarization field) is referred to as a polaron [23, 24, 25]. This conduction is termed hopping conduction or small polaron conduction.

2.2.2.1 Polaron Conduction

Small and large polarons have different transport properties. In the following description of each type of polaron, it is assumed that the charge involved is an electron, though hopping via holes is also possible. Large polarons are associated with a larger deformation of the lattice; the distortion is on the scale of several lattice constants and therefore, the polarization field is thought of as a continuum [23]. Transport mechanisms are similar to those of band conduction, but instead of electronic bands there are large polaron bands. The effective mass of the electron is greater because the mass of the phonons is associated with it [23]. The small polaron model can be used to describe conduction in ionic semiconductors where there is a strong interaction between the electron and the lattice [23]. Due to this strong interaction, the mobility of the electron is very small; therefore, it is known as being "self-trapped" in its own polarization field [23, 26]. The electron can move via two different transport mechanisms: tunneling and hopping between adjacent lattice sites [23]. Small polaron hopping is found in oxides with transition metals (NiO, MnO, $BaTiO_3$, Fe_3O_4) [27]. In order for hopping to exist, like ions in a material must be present on equivalent lattice sites and have different oxidation states [6]. In nickel manganite oxides, the small polaron hopping mechanism is found [20, 21, 22, 27, 28, 29, 30, 31, 32, 33].

The hopping of small polarons between lattice sites leads to a thermally activated mobility [22]. Thus, even if the carrier concentration is constant, there is a thermal activation to the electrical conductivity, as shown in Equation 2.9, where σ is the conductivity.

$$\sigma = \sigma_o \exp(-E_a/kT) \qquad \text{Equation 2.9}$$

The temperature independent conductivity is σ_o, k is Boltzmann's constant, E_a is the activation energy and T is the temperature [6].

2.2.2.2 Conduction Mechanisms

In the nickel manganites, conduction is believed to occur due to electron hopping between Mn^{3+} and Mn^{4+} ions [22, 27, 28, 30, 31, 32], resulting in a small polaron [20, 21, 33]. The small polaron pathways are defined by the mixed valence Mn^{3+} and Mn^{4+} cations located on the octahedral sites [20]. Electrons are self-trapped in localized states [26]. The trapped electron causes the positive ions surrounding it to move closer and the negative ions to be repelled; it polarizes its surroundings [23]. A lattice distortion surrounding the trapped electron forms. The electron cannot move unless the distortion it caused moves along with it [26]. In regards to a nickel manganite spinel, there are two sources of distortion: the Jahn-Teller effect observed with the Mn^{3+} cations, and size differences associated with cation valence.

When an electron or hole becomes self-trapped, it can be considered to be in a potential well [23]. An activation energy, E_a, is required for the electron to escape the well as shown in Equation 2.9. The hopping of the trapped electron is thermally activated [23]. At room temperature, the electrical conductivity in this material does not solely depend on the Mn^{3+} and Mn^{4+} concentration and hopping distance, but also the positioning of the manganese ions with respect to one another [34]. In order for hopping to occur, a Mn^{4+} ion must be near a Mn^{3+} ion.

2.2.3 The Nickel Manganese Oxide System

Nickel manganese oxides are one of the main material systems used to fabricate and manufacture bulk thermistors. In 1964 Wickham mapped out the bulk phase diagram for the nickel manganite system as shown in Figure 2.6 [35].

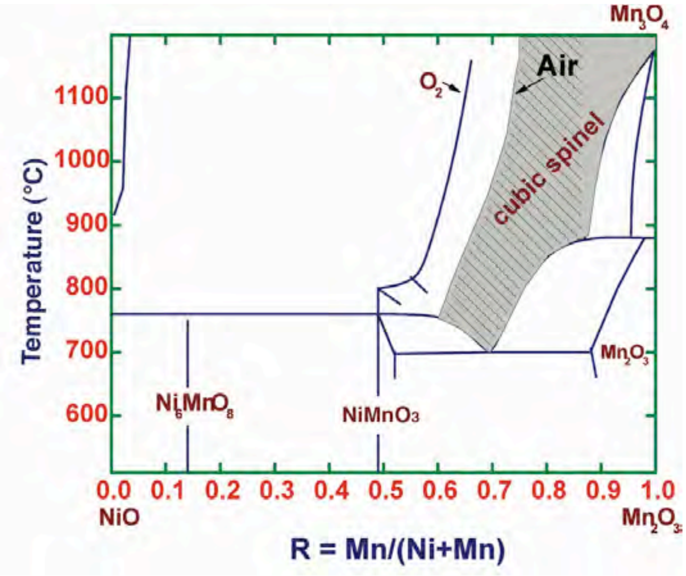

Figure 2.6: The phase diagram for the nickel manganite system, as proposed in 1964 [35]

The grey-hatched region represents where cubic spinel forms when synthesized in air. The spinel phase field is larger when a higher oxygen partial pressure is used. The large region immediately to its left is a dual phase region of spinel and NiO, a rocksalt structure. Two line compounds are present below 760°C, an ilmenite structure, $NiMnO_3$ and another cubic phase, Ni_6MnO_8. The far right of the phase diagram shows the Mn_2O_3, bixbyite structure forming at lower temperatures. At higher temperatures on the right side a tetragonal spinel forms, Mn_3O_4.

An expanded phase diagram was reported in 1989 by Tang and Goodenough [36]. The powders were prepared in the same fashion as Wickham, using nickel and manganite acetates in an oxalate route where the compound $Ni_xMn_{3-x}(C_2O_4)_3$*$6H_2O$ undergoes thermal decomposition [35, 36]. The Tang work demonstrates a metastable single-phase region of cubic spinel below 400°C between the compositions 0.6<x<1.2 (Figure 2.7) [36].

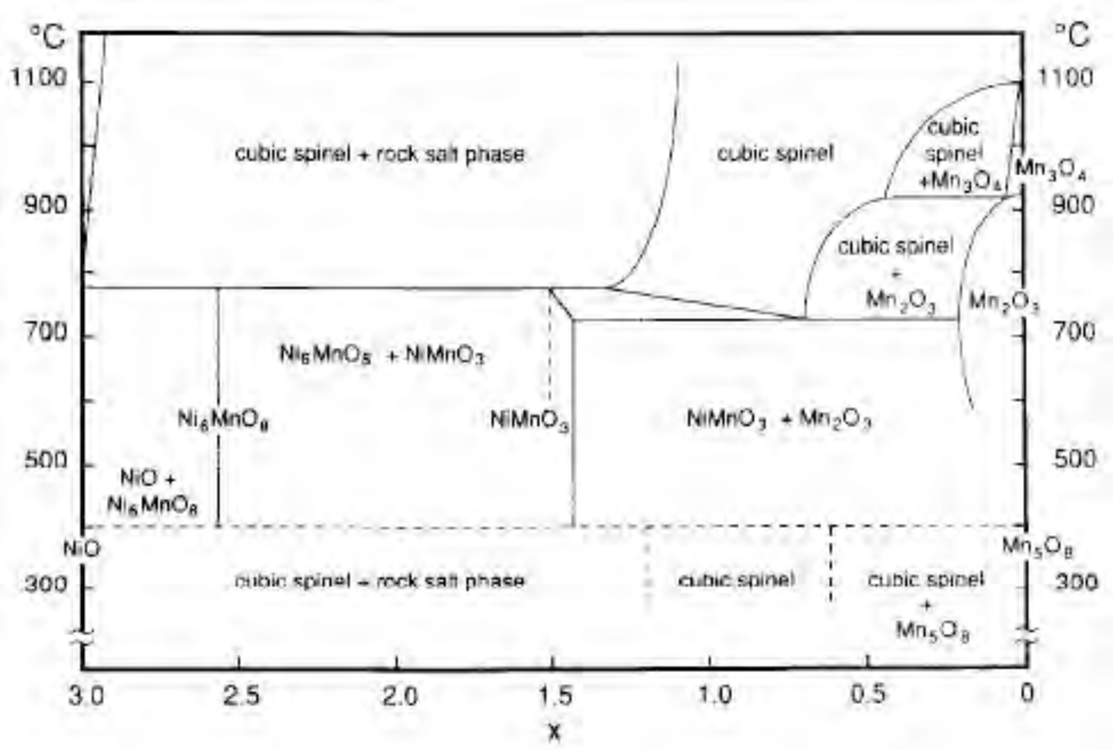

Figure 2.7: Phase diagram for thermal decomposition of $Mn_{3-x}Ni_x(C_2O_4)_3*6H_2O$ as mapped in 1989 [Source: X. Tang, A. Manthiram, and J. Goodenough. "$NiMn_2O_4$ Revisited," Journal of the Less-Common Metals. 156 (1989): 357-368.]

Typical NTC spinel thermistors are processed at elevated temperatures (e.g. 850-1250°C via decomposition of oxalate precursors) in order to achieve the thermodynamically stable high temperature form of spinel (in contrast to the low temperature spinel phases which contain cation vacancies) [20, 36, 37]. In contrast, below 750°C a metastable spinel phase can form, particularly if the local oxygen partial pressure is low [36, 37, 38]. These materials will subsequently convert irreversibly into $NiMnO_3$ and α-Mn_2O_3 in air or an oxygen rich atmosphere [36, 37, 38]. However, when the powders are heat-treated in an inert atmosphere above 400°C, the cation-deficient spinel will be retained until 600°C [36]. A tetragonal spinel has been observed to form as low as 200°C during longer soaks, while the cubic spinel begins to form at 300°C [38, 39]. To achieve relatively good crystallinity of the low temperature spinel, longer heat treatments are required, up to 60 hours [38]. Above 750°C a stoichiometric high temperature spinel forms [36]. The range between 0.6<x<1.2 shows the composition range which produces only the low temperature spinel phase, therefore the majority of the compositions studied in this thesis fall within that range. A combined phase diagram is shown in Figure 2.8.

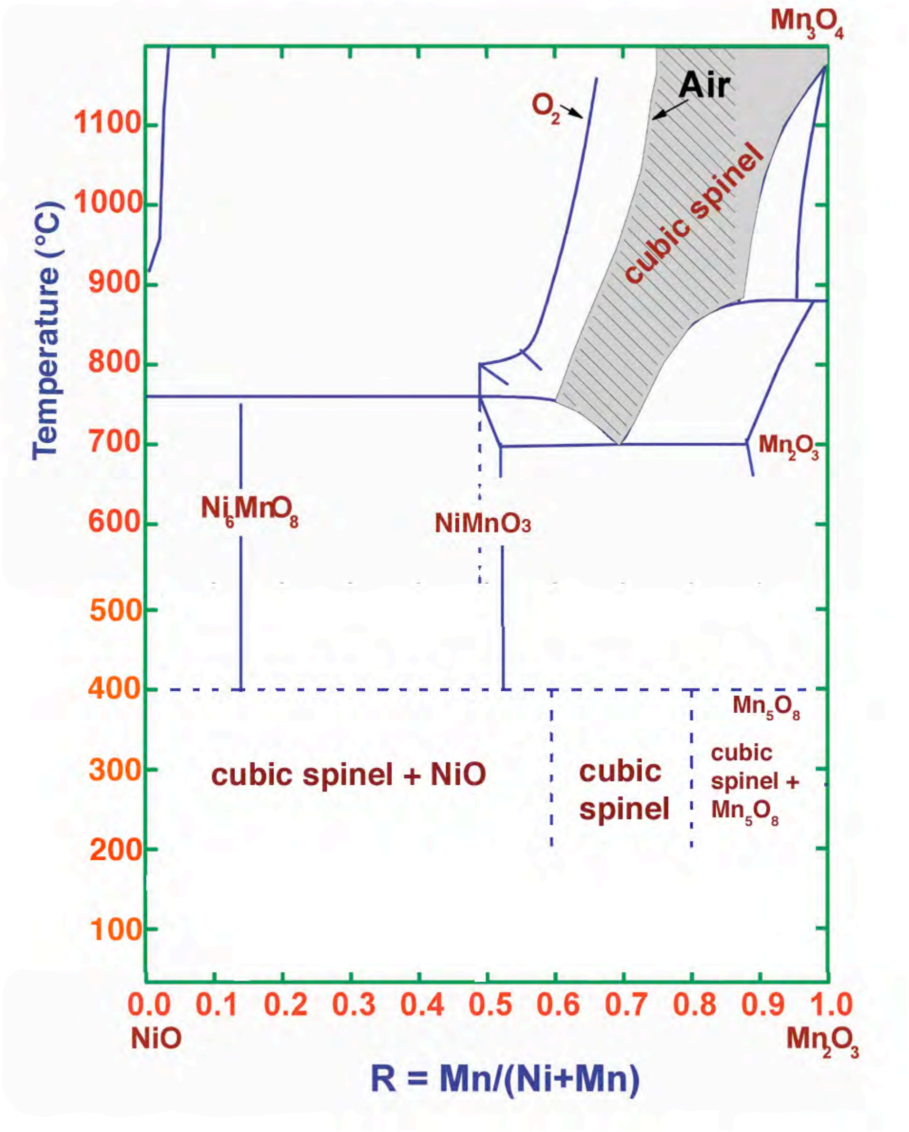

Figure 2.8: Phase diagram showing the metastable low temperature spinels in the nickel manganite system [35, 36]. Metastable regions are marked with dashed lines.

2.2.3.1 Cubic Spinel $NiMn_2O_4$

Nickel manganite spinel ($NiMn_2O_4$) has a cubic lattice with a lattice parameter of 8.4Å and belongs to the space group, $Fd\overline{3}m$. It is not categorized as either a normal or inverse spinel, but as an intermediate structure between the two types [4, 40]. Stoichiometric Mn_3O_4 is an insulating normal spinel; the Mn^{2+} cations sit on tetrahedral sites and the Mn^{3+} cations sit on the octahedral sites [4]. When this is doped with Ni, the Ni^{2+} cations will tend to occupy the octahedral sites due to its large octahedral site preference [4]. Some of the Mn ions on the octahedral sites must change oxidation state from 3+ to 4+ to maintain electrical neutrality [4]. The octahedral site now incorporates Mn ions of two oxidations states as well as Ni^{2+} cations as follows: $Ni^{2+}{}_xMn^{4+}{}_xMn^{3+}{}_{1-2x}Mn^{3+}$ [4]. The addition of Ni provides like ions of different oxidation states on equivalent lattice sites, and so promotes hopping conduction [4]. The exact oxidation states for the Ni and Mn cations in the spinel structure depend heavily on the atmosphere and temperature during synthesis.

Fritsch et al. reported the distribution of cations in the spinel structure using neutron diffraction [27]. It was found that the manner in which samples are cooled after sintering affects the Ni site occupancy. A $Ni_{0.8}Mn_{2.2}O_4$ sample sintered at 1160°C and cooled at a rate of -5°C/min showed the following distribution of cations (where the brackets denote the octahedral site):

$$Mn^{2+}{}_{0.89}Mn^{3+}{}_{0.09}Ni^{2+}{}_{0.02}[Ni^{2+}{}_{0.78}Mn^{3+}{}_{0.53}Mn^{4+}{}_{0.69}]O^{2-}{}_4$$

The same composition was again fired at 1160°C and then quenched at 900°C to give:

$Mn^{2+}_{0.913}Ni^{2+}_{0.087}[Ni^{2+}_{0.713}Mn^{3+}_{0.574}Mn^{4+}_{0.713}]O^{2-}_{4}$

Thus, after slow cooling, there is only a very small amount of Ni cations on the tetrahedral sites, since Ni^{2+} prefers to sit on the octahedral sites. When quenched, more Ni cations remain located on the tetrahedral sites, suggesting that the degree of inversion decreases at elevated temperatures [27, 41]. This was confirmed by Boucher et al., who measured the degree of inversion, as illustrated in Figure 2.9 [41].

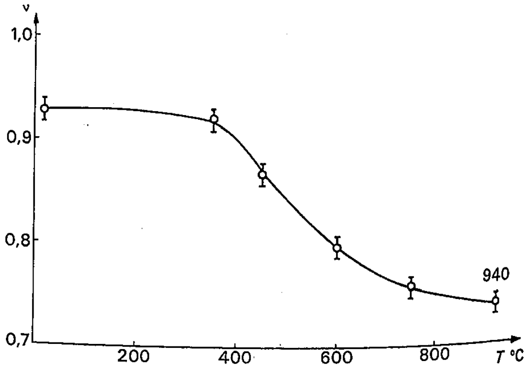

Figure 2.9: Plots shows the decrease in inversion, ν, in nickel manganite spinels as a function of temperature [Source: B. Boucher, R. Buhl, and M. Perrin. "Etude cristallographique du manganite spinelle cubique $NiMn_2O_4$ par diffraction de neutrons," Acta Crystallographica Section B – Structural Crystallography and Chrystal Chemistry. B 25 (1969): 2326-2333.]

Schmidt et al. suggests the chemical formula should be written $NiMn_2O_{4+\delta}$ [28, 40]. However, it seems unlikely that an excess of oxygen could be accommodated in a spinel structure, since it has a close-packed arrangement of oxygen atoms. It is likely that this is simply an artifact of cation vacancies, rather than excess oxygen. Cation vacancies have been reported in spinels formed below 750°C [36, 37, 38, 42].

2.2.3.2 Ilmenite $NiMnO_3$

The mineral ilmenite has a chemical formula of $FeTiO_3$ and belongs to the space group $R\overline{3}$ [43]. Its isomorph $NiMnO_3$ has a rhombohedral structure with a lattice parameter of about 5.34 Å and an alpha angle of about 54°. The structure contains octahedrally coordinated Ni^{2+} and Mn^{4+} cations situated within the unit cell as pictured in Figure 2.10 [43].

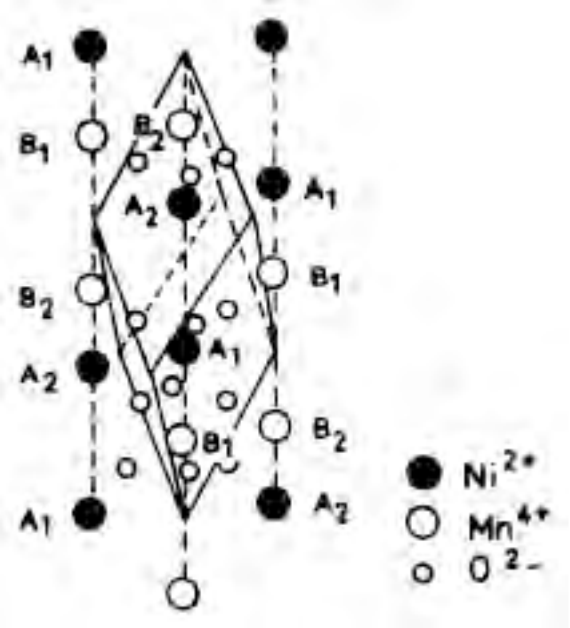

Figure 2.10: Unit cell of ilmenite $NiMnO_3$ [Source: M. Pernet, J. Joubert, and B. Ferrand. "Etude par diffraction neutronique de l'ilmenite ferrimagnetique $NiMnO_3$," Solid State Communications. 16 (1975): 503-308.]

The oxygen atoms sit in a nearly close packed arrangement. Its structure can also be described as having 2/3 of the octahedral sites occupied in a hexagonally close packed lattice of oxygen ions [44].

$NiMnO_3$ is ferrimagnetic with a Curie temperature of about 430 K [43, 44]. It has been synthesized from oxalates, as mentioned above, and from a hydrothermal reaction of

NiO and MnO_2 at 700°C and 3000 atm of pressure [45]. Measured activation energies for conduction change from low to high temperatures. Up to about 75°C $E_a = 0.44$ eV while above that it increases to $E_a = 0.7$ eV [44]. Ilmenite structured materials have been studied to evaluate their catalytic performance [46, 47].

2.2.3.3 Ni_6MnO_8

Ni_6MnO_8 has the same structure as Mg_6MnO_8, which evolved from the rocksalt structure of MgO [44]. One eighth of the Mg ions in MgO are replaced by Mn^{4+} and one eighth of the Mg sites are vacant [44]. The other 6/8 of the octahedral sites are occupied by Ni^{2+} [48]. It belongs to the space group Fm3m where the Ni^{2+} and Mn^{4+} ions are octahedrally coordinated in a cubic lattice with a lattice parameter of 8.38 Å [48].

Ni_6MnO_8 was studied along with other metallic oxides to be used in oxygen sensors [48]. The activation energy for conduction (due to polaron hopping) Ni_6MnO_8 was found to be about 0.43 eV and did not change as a function of temperature [44].

2.2.3.4 Bixbyite Mn_2O_3

Bixbyite, α-Mn_2O_3, has mainly been studied for its magnetic properties [49]. It also has been examined for use in NTC thermistor applications mainly because doped Mn_3O_4 and ferrite materials have been heavily researched over the years [50]. Bixbyite has a slightly more complicated crystal structure around room temperature because a distortion occurs at 302K [49, 51, 52]. Above 302 K it has an undistorted cubic lattice, belonging to the Ia3 space group [51, 52]. Below 302 K it is orthorhombically distorted to the Pcab space group [51, 52]. Table 2.1 shows the lattice parameters as a function of temperature [51].

Table 2.1: Lattice constants of α-Mn_2O_3 as a function of temperature: above 302 K α-Mn_2O_3 has a cubic lattice [Source: S. Geller and G. Espinosa. "Magnetic and Crystallographic Transitions in Sc^{3+}, Cr^{3+}, and Ga^{3+} Substituted Mn_2O_3," Physical Review B. 1 (1971): 3763-3769.]

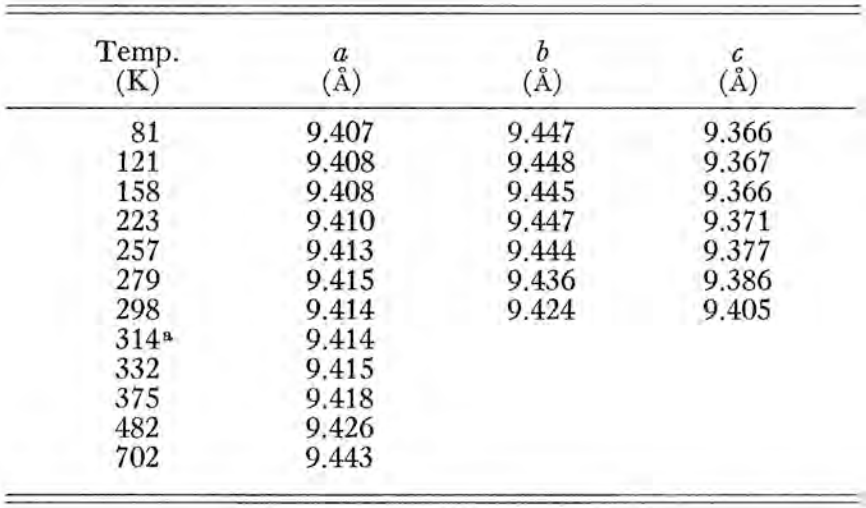

Temp. (K)	*a* (Å)	*b* (Å)	*c* (Å)
81	9.407	9.447	9.366
121	9.408	9.448	9.367
158	9.408	9.445	9.366
223	9.410	9.447	9.371
257	9.413	9.444	9.377
279	9.415	9.436	9.386
298	9.414	9.424	9.405
314[a]	9.414		
332	9.415		
375	9.418		
482	9.426		
702	9.443		

It was proposed by Geller that α-Mn_2O_3 does not exhibit the corundum structure due to the Jahn-Teller distortion that occurs with the Mn^{3+} cation [51].

Mn_2O_3 has a room temperature resistivity that is two orders of magnitude lower than Mn_3O_4 [50, 53] which depends on the relative humidity (See Table 2.2) [53].

Table 2.2: Resistance values of two manganese oxides taken at room temperature after different exposure times to different relative humidities (RH) [53]

	20% RH	**80% RH**	**20%RH**
Mn_2O_3	$5x10^7$ Ω	$1x10^6$ Ω	$5x10^7$ Ω
Mn_3O_4	$2x10^9$ Ω	$5x10^6$ Ω	$2x10^9$ Ω
	0-10 minutes	10-20 minutes	20-30 minutes

Mn_2O_3 converts into Mn_3O_4 above 900°C [50]. Mn_3O_4 is an insulator, but when the Mn^{3+} is substituted with a divalent or monovalent ion, a pair of Mn^{3+} and Mn^{4+} ions are created on octahedral sites [50]. This pair allows for hopping conduction to occur.

2.2.4 Phase Decomposition

As would be expected based on the phase diagram (See Figure 2.11), nickel manganite spinel has been observed to decompose at elevated temperatures (>900°C) and low oxygen partial pressures [35, 36].

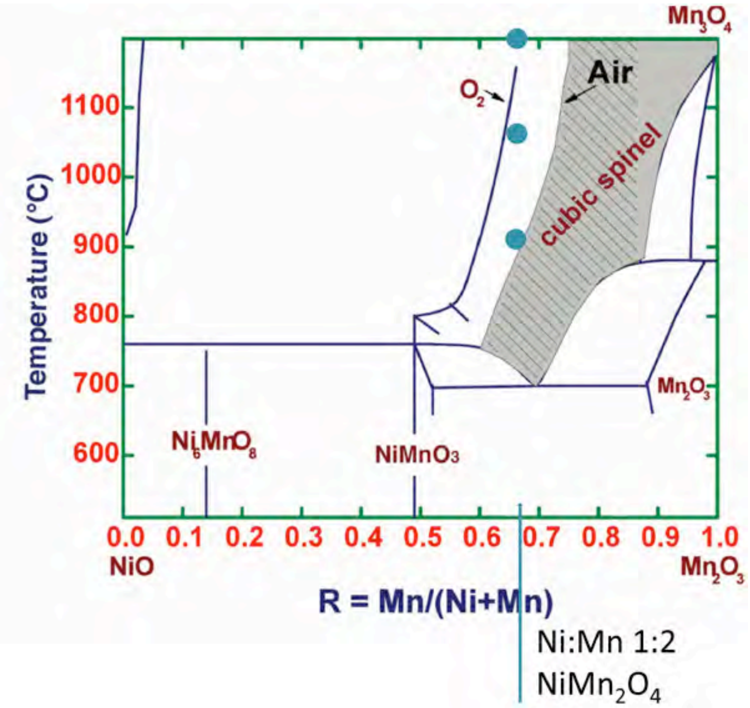

Figure 2.11: Nickel manganite phase diagram highlighting with blue dots the compositions synthesized by Reaney et al. to show phase decomposition [35, 54]

Equation 2.10 illustrates the loss of oxygen and decomposition of single-phase spinel in air above 1100°C as observed by Larson, Arnott, and Wickham [22].

$$NiMn_2O_4 - 1/3O_2 \rightarrow NiO + 2/3Mn_3O_4 \qquad \text{Equation 2.10}$$

This reaction can occur at lower temperatures in a reduced oxygen partial pressure environment. Reaney and colleagues observed that $NiMn_2O_4$ (Ni:Mn ratio of 1:2) decomposed into a Ni-rich rocksalt structured compound and a Mn-rich spinel [20, 54, 55]. Bulk samples were heat-treated at 1050°C and 1200°C as labeled in Figure 2.11 [54]. An endothermic reaction at 907°C, coupled with a 1.25% weight loss was observed. This is the temperature $NiMn_2O_4$ believed to decompose [54]. When the analysis was performed in an oxygen rich environment the reaction didn't occur until 946°C [54].

It was proposed that with increased temperature the Mn^{3+} cations tend to concentrate into clusters. Ni^{2+} prefers to sit on octahedral sites, but as the clustering of Mn continues, the Ni in the spinel is displaced to the energetically unfavorable tetrahedral sites. When the driving force is great enough, the Ni^{2+} precipitates into a rocksalt NiO phase [54]. An increase in Mn concentration on octahedral sites leads to a decrease in inversion, which ultimately causes a tetragonal distortion of the lattice [54]. Thus, changes in the degree of inversion of the spinel structure are correlated with decomposition in the material.

2.2.5 Aging in Nickel Manganites

The electrical properties of nickel manganese oxides are known to change over time during heat treatments [34, 54]. This process is called aging. It has been observed that the resistance of the thermistor material increases as a function of time [4, 56, 57, 58, 59, 60, 61, 62, 63]. It is assumed that the number of "conductive pathways" through the material decreases while the concentration of lattice imperfections increase [56, 57]. A systematic series of experiments on samples with different electrodes demonstrated that the electrode– semiconductor interface is not responsible for aging [4]. Instead, the aging is a function of the thermistor composition [4].

Macklen describes three mechanisms that may cause instability in the electrical properties of nickel manganite based materials. The first is the possibility of a change in oxygen content. However, experiments run in different oxygen atmospheres showed no effect on aging [4]. The second mechanism involves the movement of cations within the structure without altering the overall chemical composition, changing the degree of inversion of the spinel [4]. It is possible that Ni will diffuse between lattice sites, slowly changing the effective carrier concentration [4]. The third mechanism to explain aging would be a change in carrier concentration and mobility associated with the electronic states on the crystallite surfaces [4].

The aging coefficient is defined in Equation 2.11, where R_o is the resistance value at 25°C before annealing and R is the value measured at 25°C after heat treatment at 150°C for 500 hours (temperature and time conditions can vary) [59].

$$\Delta R/R\ (\%) = [(R-R_o)/R_o]*100 \qquad \text{Equation 2.11}$$

Table 2.3 compiles data on aging of bulk thermistors at a variety of temperatures. In general, it is clear that aging does exist and it is a problem for property reliability. It is also shown that stability can be improved by changing composition.

Table 2.3: Summary of bulk compositions aged at various times and temperatures

Ref	Composition	T (°C)	Hrs	%ΔR/R	Conditions
59	$Cu_{0.3}Ni_{0.66}Mn_{2.04}O_4$	150	500	5.4	
56	$Mn_{1.93}Ni_{0.66}Cu_{0.41}O_4$	125	200	6.0-10.0	depending on cool rate
	$Mn_{1.87}Ni_{0.66}Cu_{0.46}O_4$+3.6%Ba	125	200	1.8-5.6	depending on cool rate
54	$NiMn_2O_4$	400	8	12.0-26.0	single phase vs slow cooled
60	$Cu_{0.1}Ni_{0.8}Co_{0.2}Mn_{1.9}O_4$	125	500	5.5	
	$Cu_{0.8}Ni_{0.1}Co_{0.2}Mn_{1.9}O_4$	125	500	7.0	
	$Cu_{0.1}Ni_{0.1}Co_{1.6}Mn_{1.2}O_4$	125	500	8.5	
61	$Mn_{2.46}Ni_{0.54}O_4$	150	500	1.0	
	$Mn_{1.96}Ni_{0.54}Fe_{0.5}O_4$	150	500	17.0	
	$Mn_{1.46}Ni_{0.54}FeO_4$	150	500	2.0	
34	$Mn_{1.89}Ni_{0.66}Cu_{0.45}O_4$	125	500	24.0	
62	$Mn_{2.4}Ni_{0.5}In_{0.1}O_4$	150	550	4.3	
	$Mn_{2.36}Ni_{0.54}In_{0.1}O_4$	150	550	2.0	
	$Mn_{2.32}Ni_{0.58}In_{0.1}O_4$	150	550	0.8	
	$Mn_{2.28}Ni_{0.62}In_{0.1}O_4$	150	550	1.3	
	$Mn_{2.24}Ni_{0.66}In_{0.1}O_4$	150	550	1.0	
63	$Cu_{0.1}Ni_{0.8}Co_{0.2}Mn_{1.9}O_4$	170	500	2.5	different sintering conditions
	$Cu_{0.1}Ni_{0.8}Co_{0.2}Mn_{1.9}O_4$	170	500	7.0	
	$Cu_{0.1}Ni_{0.8}Co_{0.2}Mn_{1.9}O_4$	170	500	21.0	
57	$Cu_{0.1}Ni_{0.8}Co_{0.2}Mn_{1.9}O_4$	125	500	5.5	

For $Cu_{0.3}Ni_{0.66}Mn_{2.04}O_4$ prepared from a mixed oxalate route, this coefficient was 5.4% after 500 hours [59]. Metz performed the same measurement except at 125°C for 500 hours and reported 24% for a $Mn_{1.89}Ni_{0.66}Cu_{0.45}O_4$ composition [34]. It has been found that the aging rate of spinel thermistors is a function of the phase content. Samples processed so that they are single phase show less change in resistance (ΔR/R) over time (+10% over 8 hours), while the slowly cooled, multiphase specimens showed a greater change in resistance over time (+26% over 8 hours) [20, 54].

More recent work has dealt specifically with improving aging by doping. Iron increases aging rates while indium makes the spinel more thermodynamically stable [61, 62]. At least part of this difference is believed to be due to the fact that Fe has multiple oxidation states, while indium has a single oxidation state, 3+, and forms single-phase spinel when incorporated into the structure [62]. Depending on the concentration of copper incorporated into the spinel structure, either improvements in stability can occur (<1% CuO) or increased aging can result (10-20% CuO) [4]. With less than 1% copper oxide only a 1% change in resistance was observed over a year, while with an addition of 10-20% CuO, the resistance increased about 5-10% over a year [4].

The processing conditions of the thermistor play a large role in its stability [54, 56, 63]. When the sample is quenched after sintering, the stability in resistance is improved compared to a sample that was slowly cooled [56, 63, 64]. For samples aged at 400°C, it is believed that the decomposition of spinel into NiO is reversed and Ni^{2+} cations re-enter the spinel structure, changing the resistance [54]. Samples with higher concentrations of NiO decomposition show higher aging coefficients, while a single phase sample or one containing trace amounts of NiO exhibit improved aging coefficients [63].

The majority of the literature on aging in thermistor materials deals with bulk ceramics. Kukuruznyak examined the aging in $Ni_{0.48}Co_{0.24}Cu_{0.6}Mn_{1.68}O_4$ spinel thin films made from acetylacetonate solution with and without borosilicate doping as shown in Figure 2.12 [58].

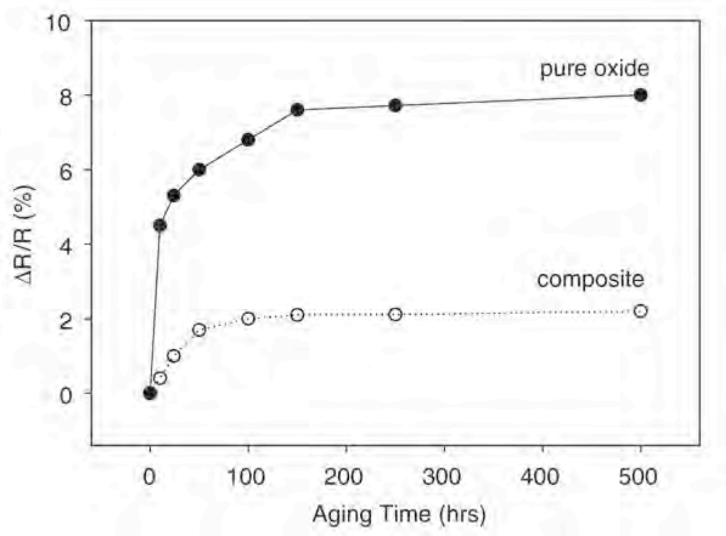

Figure 2.12: Aging of nickel manganite spinel thin films for 500 hours at 150°C [Source: D. A. Kukuruznyak, J. G. Moyer, and F. S. Ohuchi. “Improved aging characteristics of NTC thermistor thin films fabricated by a hybrid sol-gel-MOD process,” J. Am. Ceram. Soc. 89 (2006): 189-192.]

Samples of the base oxide and others doped with 5 wt% B_2O_3 and 5 wt% SiO_2 to give $Ni_{0.48}Co_{0.24}Cu_{0.6}Mn_{1.68}O_4*0.22SiO_2*0.15B_2O_3$ were annealed at 500°C. The aging results at 150°C are similar to those of bulk materials; in the first 100 hours the ΔR/R increased significantly and then leveled out and remained constant between 200-500 hours. The base composition showed a much greater change (over 7%) than the doped film (less than 2%) during the first 100 hours [58].

2.2.6 Nickel Manganite Thin Films

Spinel thin films have been prepared using different processing routes including sputtering [29] and metal organic decomposition (MOD) [58]. In the thin films, as well as the bulk, aging has been observed, posing a problem for stability of the electrical properties. A summary of the literature is given in Table 2.4.

Table 2.4: Summary of nickel manganite thin film processing from the literature

Ref	Composition	Method	Resistivity (Ωcm) RT	E_a (eV)	Conditions
33	$Ni_{0.75}Mn_{2.25}O_4$	RF reactive sputtering from oxide target	15000.00	0.371	Ar atmosphere
	$Ni_{0.75}Mn_{2.25}O_4$	RF reactive sputtering from oxide target	3300.00	0.345	0.09% oxygen
	$Ni_{0.75}Mn_{2.25}O_4$	RF reactive sputtering from oxide target	3000.00	0.345	0.17% oxygen
29	$Mn_{1.56}Co_{0.96}Ni_{0.48}O_4$	Sputtered Ar+PO_2 of 10%, 4mTorr	1000.00	0.352	
65	$Ni_{0.48}Co_{0.24}Cu_{0.6}Mn_{1.68}O_4$	MOD	9.75	0.139	600°C anneal
	$Ni_{0.48}Co_{0.24}Cu_{0.6}Mn_{1.68}O_4$	MOD	1015.00	0.247	800°C anneal
66	$NiMn_2O_4$	Electron beam evaporation	4600.00	0.515	as grown (air)
	$NiMn_2O_4$	Electron beam evaporation	3600.00	0.344	500°C 30min (air)
	$NiMn_2O_4$	Electron beam evaporation	12.00	0.340	600°C 30min (air)
	$NiMn_2O_4$	Electron beam evaporation	8400.00	0.557	as grown (N_2)
	$NiMn_2O_4$	Electron beam evaporation	6200.00	0.521	500°C 30min (N_2)
	$NiMn_2O_4$	Electron beam evaporation	25000.00	0.527	600°C 30min (N_2)
	$NiMn_2O_4$	Electron beam evaporation	3000.00	0.561	as grown (O_2)
	$NiMn_2O_4$	Electron beam evaporation	0.93	0.246	500°C 30min (O_2)
	$NiMn_2O_4$	Electron beam evaporation	2.00	0.288	600°C 30min (O_2)

Thin film processing of the nickel manganite spinel produces material that possesses properties in the range of the bulk. Depending on the partial pressure of oxygen (pO_2) or on the anneal temperature, the properties show some variation. For example, Fau et al. deposited $Ni_{0.75}Mn_{2.25}O_4$ films by RF reactive sputtering from a sintered oxide target. Films synthesized in a pure Ar atmosphere had a high resistivity (around 15,000 Ωcm). Samples deposited in a 0.09% oxygen environment had much smaller resistivities, around 3300 Ωcm [33]. Parlak showed similar results after annealing electron beam evaporated films in oxygen at 500°C and 600°C; the resistivity values decreased multiple orders of magnitude compared to annealing in air or in nitrogen [66]. Films annealed in nitrogen showed the highest resistivities [66].

Nickel manganite spinel thin films have been synthesized using a MOD route with nickel and manganese acetylacetonates, copper nitrate, and cobalt acetate tetrahydrate. This synthesis method is discussed in more detail in the Experimental Procedure chapter. Spinel films were shown to crystallize at temperatures as low as

500°C [58, 65], which is not as low a temperature as was reported for crystallizing powder from oxalate precursors.

In this thesis the films were made using chemical solution deposition (CSD). It is one of the simplest and least expensive thin film fabrication processes because no vacuum system or elaborate deposition chamber is required. Low temperature synthesis of the thin films is possible, as is a large deposition area [67, 68]. No vaporization or ionization of the solutions is required for deposition, and films of high purity and good homogeneity can be made [67]. CSD is a process that can be modified quickly in order to synthesize a new material system that may not have been studied in a thin film form [69]. The following section provides a general introduction to the field.

2.3 Chemical Solution Deposition

Chemical solution deposition (CSD) is a common processing method for the fabrication of thin films [57]. CSD was originally developed in the mid 1980s [69, 70]. CSD consists of three main processing steps [71]: synthesis of the precursor solution, deposition of the solution on the substrate, and heat-treatment to remove the organics and crystallize the desired phase.

In chemical solution deposition, control of the exact composition on a molecular level (local stoichiometry) is (at least in principle) possible [67, 69]. It is also easy to incorporate multiple elements into the solution, which is an advantage when processing complex oxide films [68].

2.3.1 Synthesis of the Precursor Solution

CSD can be separated into three categories, including metal-organic decomposition (MOD), sol-gel, and chelation [69]. According to some scientists, chelation should be categorized as a form of the sol-gel method [71]. Therefore the sol-gel process can be subcategorized into different routes depending on the exact chemistry involved. Modified versions include the chelate process and the Pechini method [71]. Each CSD route can be characterized by the chemical reaction and the type of precursors used to make the solution.

Most CSD solutions are created using metal-organic compounds as the main source of cations. Before discussing the different CSD routes, a quick explanation of the different metal-organic precursors used will be given. The main solution precursors can be divided into three classes [69].

a. Alkoxides – a salt obtained from an alcohol by removing the H from the –OH and replacing it with a metal; $M(OR)_x$, where M = metal, OR = alkyl group

Alkoxides are often used as the cation sources for CSD processes. These compounds are very sensitive to water [69]. In the sol-gel process, alkoxides are used to form oligomers, which are short-chained polymers. In a polymeric form the alkoxide can be stabilized to reduce its sensitivity to water. More polar groups can be present around the alkyl allowing more bonds to form with the metal cation. Among the chemicals often used to bond to the alkyl to form R-O-R bonds are 2MOE = 2-methoxyethanol, amine groups ($-NH_2$), keto groups ($-C=O$), and alcohol groups ($-C-OH$). All of these are polar groups, meaning there is a dipole present. When multiple polar groups bond to the metal, the groups are referred to as a chelating agent. When a chelating agent is used, the alkoxide becomes even more stable and decreases its sensitivity to water, allowing a stable solution for deposition [69].

A heteroalkoxide is able to incorporate two or more metal atoms into its structure. There are some that contain up to five metals. A heteroalkoxide is formed from the mixing of two alkoxides, one of high and one of low electronegativity. They are mainly used as precursors for multicomponent ceramics, such as spinel $MgAl_2O_4$ and $LiNbO_3$ [72].

b. Carboxylates – salts of carboxylic acids; R-COOH, where R=alkyl

Carboxylates, in general, are very stable in water and oxygen and are generally used in the MOD process. Examples of carboxylates are acetates and propionates. Their carboxylic acid counterparts are acetic acid ($R=CH_3$) and propionic acid ($R=C_2H_5$). It is easiest to dissolve these salts in their paired acid. For extra long-chained alkyl groups (C_7H_{15}), xylene can be used as the solvent [69].

c. Beta-diketonates – organic molecules where a methylene group ($-CH_2$) divides two keto groups

Beta-diketonates are molecules in which an exchange of a hydrogen atom occurs in order to transform a keto into an alcohol. These tend to dissolve easily in alcohols, ketones, and ethers. Films made with these precursors require higher pyrolysis temperatures and tend to remain amorphous up to higher temperatures [69].

2.3.1.1 Metal-Organic Decomposition

Metal-organic decomposition uses a solution of metal organics that are insensitive to hydrolysis [71]. This deposition technique was implemented for the synthesis of the solutions used in this work. Common metal organics are carboxylate compounds such as acetates and ethyl hexanoates or beta-dikeytonates such as pentanedionates [71]. These are dissolved in nonpolar solvents [68], for example, xylene [70]. The metal organic compounds do not interact with the solvent and there is no oligomerization behavior as in sol-gel or chelate [70]. The solution is very stable and can be seen as a simple mixture of the starting ingredients [68]. The precursors remain representative of the starting molecules [70]. The precursor compounds are physically condensed onto the substrate through rapid solvent evaporation [73]. The liquid film is then heat-treated to enable thermal decomposition during the pyrolysis or the burnout stage [67]. The organic material is usually removed in the form of CO_2 or water [68]. Extreme exothermic reactions can occur during this stage that can cause biaxial tensile stresses in the film [68]. These stresses can cause cracking of the film [68].

2.3.1.2 Sol-Gel

Sol-gel is a chemical solution process used to make ceramic and glass materials in the form of thin films, fibers (extruded shapes), or powders [67]. In essence, a liquid film is transformed into a solid through hydrolysis and polycondensation reactions [67]. A sol is a colloidal (the dispersed phase is so small that gravitational forces do not exist; only Van der Waals forces and surface charges are present) or molecular suspension of solid particles of ions in a solvent [74]. A gel is a semirigid mass that forms when the solvent from the sol begins to evaporate and the particles or ions left behind begin to join together in a continuous network [74].

The sol typically consists of metal alkoxides (e.g. tetraethylorthosilicate=TEOS, titanium isopropoxide, aluminum butoxide) or metal salts (acetates, nitrates) [19, 68, 71]. The metal alkoxides are usually in the form of covalent liquids [19]. These are dissolved in an alcohol-based solvent to form a stable sol [68]. The alcohol promotes miscibility of the alkoxide and water [19]. Water is a key ingredient to cause the hydrolysis reaction [19]. Sol-gel is similar to MOD, except that the chemistry is designed to produce metal-oxide-metal chains using hydrolysis and polycondensation reactions [68]. The formation of the chains creates a 3D continuous gel network, which is the amorphous oxide layer [68]. Thermal treatments are performed to turn the amorphous layer into the desired crystalline oxide phase.

The series of reactions that occur during the sol-gel process include [68, 70]:

a. Hydrolysis: $M(OR)_x + H_2O \rightarrow M(OR)_{x-1}(OH) + ROH$; where $M(OR)_x$ = alkoxide compound, M = metal, OR = alkyl group

b. Condensation: (-OH elimination): $2M(OR)_{x-1}(OH) \rightarrow M_2O(OR)_{2x-3}(OH) + ROH$

c. Condensation: (H_2O elimination): $2M(OR)_{x-1}(OH) \rightarrow M_2O(OR)_{2x-2}(OH) + H_2O$

2.3.1.2.1 Pechini Method

The Pechini method is a modified sol-gel process that uses an aqueous solution of polymeric precursors dissolved in an alpha-hydroycarboxylic acid (citric acid) and water [75, 76]. The chemical reactions that occur during the synthesis include chelation or the formation of ring compounds around the metal cations [75].

2.3.1.3 Chelate Process

Like sol-gel, the chelate process (chelation) utilizes a liquid solution and similar deposition techniques. This solution, however, is typically made from alkoxide compounds like sol-gels, but consists of modifying ligands such as acetic acid, acetylacetone, or amines to cause the chemical reaction to occur [69, 70]. The solution preparation time is much less than sol-gel; usually it requires less than one hour compared to sol-gel's one-to-two-day preparation time [69, 70]. No distillation or refluxing is required [70]. Like sol-gel, oligomerization occurs during the solution synthesis as shown in Equation 2.12 [69]. The solutions tend to be more stable in air than sol-gel solutions because the chelating agents decrease the hydrolysis sensitivity of the alkoxide [69].

$$M(OR)_n + xCH_3COOH \rightarrow M(OR)_{n-x}(OOCCH_3)_x + xROH \qquad \text{Equation 2.12}$$

2.3.2 The Coating or Deposition Process

Deposition or coating of the chemical solutions onto a substrate can occur via spin coating, dip coating, spraying, roll coating, slot-die coating, and ink-jet printing [71].

Spin coating was used for the deposition of the MOD films in this work. For all the techniques, the thickness of the precursor layer is dependent upon the solution's properties, such as molarity and viscosity [71]. Thickness is also dependent on factors from the deposition technique, including deposition speed and coating time [71]. Properties of the substrate also affect thickness. Surface tension and wetting play large roles in coating ability and thickness.

2.3.3 Heat Treatment

The thermal treatments required to remove organics and crystallize the film are different for different solution routes and end products. The heat treatments are required to transform the as-deposited layer into its desired crystalline phase. There are two main stages [71].

a. Pyrolysis - This stage is required in order to remove the organic matter that remains in the amorphous film. Typical temperatures for pyrolysis range from 300-600°C [71]. During this stage a large volume reduction occurs [71]. Stress and microcracks can easily form. Following pyrolysis, films are often amorphous or nanocrystalline and porous film [71].

b. Annealing - This stage causes the crystallization of the amorphous intermediate film state into its desired phase. The temperatures for this stage usually range between 600-1200°C [71]. During annealing many of the stresses that formed during pyrolysis are removed.

2.4 Spin Spray Ferrite Plating

The spin spray plating technique has also been used to synthesize thin films with the spinel crystal structure. The process is performed at atmospheric pressure, without a vacuum system, and at temperatures under 100°C with no additional heat treatments [77]. A research group at the Tokyo Institute of Technology developed the technique in the 1980s along with the equipment needed to deposit these films [77].

The plating process for film deposition is a modification of a method used for the treatment of wastewater. The heavy metal ions in the water are incorporated into a spinel lattice by a wet oxidation process [77]. The resulting powders could then be separated from the water by magnetic separation [77].

In order to prepare films, a solution containing the cations of interest is sprayed onto the heated, rotating substrate alternately with an oxidant, as shown in Figure 2.13.

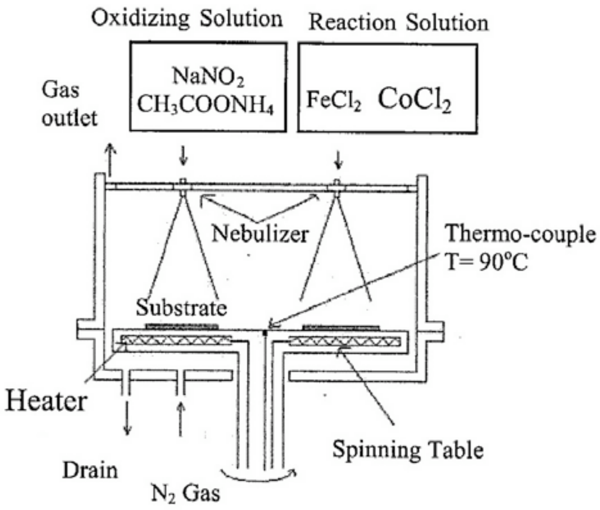

Figure 2.13: Diagram of the experimental setup for the spin spray ferrite plating technique [Source: T. H. Hai, H. T. B. Van, T. C. Phong, A. Mansanori. "Spinel ferrite thin-film synthesis by spin-spray ferrite plating," Physica B. 327 (2003) 194-197.]

In many cases the oxidant utilized consists of ammonium acetate and sodium nitrite (CH_3COONH_4 and $NaNO_2$).

The chemical process describing the spinel formation is shown in Figure 2.14.

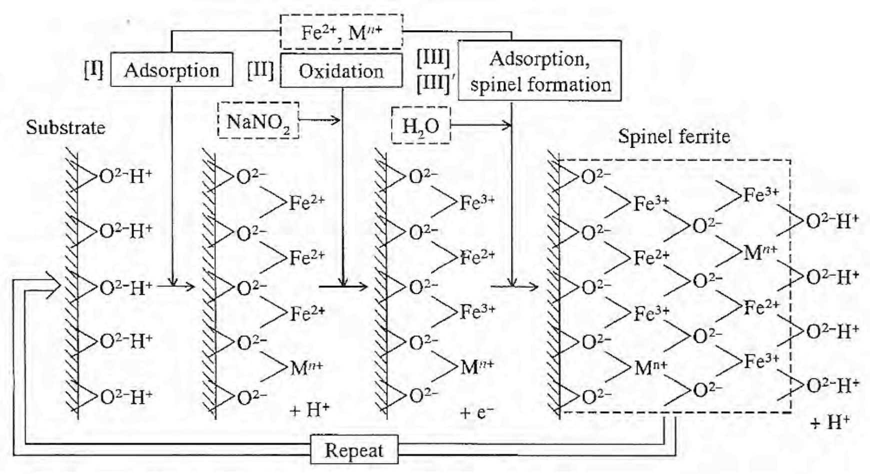

Figure 2.14: The chemical reaction that occurs during the spin spray ferrite plating process [Source: M. Abe. "A soft solution processing technique for preparing ferrite films and their applications," MRS Bulletin. (2000): 221-224.]

The substrate begins with –OH groups on its surface. The reaction solution containing the metal chlorides is sprayed onto the heated substrate. In the case of Fe_3O_4, the Fe^{2+} ions bond to the O^{2-} while the H^+ is removed. The oxidizing solution is sprayed on and causes the Fe^{2+} to oxidize to Fe^{3+}, releasing an electron. These cations then react with water to create another hydroxylated surface. The reaction continues and forms layer by layer a ferrite spinel structure (Fe_3O_4). Table 2.5 gives examples of films that have been deposited using this approach.

Table 2.5: Summary of spin spray films synthesized in the literature

Ref	Cations	pH	mmol/L	Oxidizer	mmol/L	pH adjuster	mmol/L	pH	Substrate	Flow (L/hr)	rpm	T (°C)	growth rate (nm/min)
78	$FeCl_2$		3.8-7.6	$NaNO_2$	2.9-36.2	CH_3COONH_4	65.0	5.0-7.0				90	
	$CoCl_2$		0-7.6										
78	$FeCl_2$		3.78	$NaNO_2$	1.45	CH_3COONH_4	32.5					90	
	$CoCl_2$		0.19-1.7										
	$NiCl_2$		0.19-1.7										
79	$FeCl_2$			$NaNO_2$		CH_3COONH_4							
	$NiCl_2$												
	$ZnCl_2$												
80	$FeCl_2$		16.6	$NaNO_2$	4.35	CH_3COONH_4	65.0		glass	3	150	90	
	$NiCl_2$		5.26										
	$ZnCl_2$		0.18-0.54										
	$CoCl_2$		0-0.84										
81	$FeCl_2$			$NaNO_3$		CH_3COONH_4			glass				
	$NiCl_2$												
	$ZnCl_2$												
	$CoCl_2$												
82	$FeCl_2$			$NaNO_2$		CH_3COOK			glass	4.2			
	$MnCl_2$												
	$ZnCl_2$												
83	$FeCl_2$	5.2	15.1	$NaNO_2$	7.25	CH_3COONH_4	65.0	6.9			300	80	40
	$NiCl_2$		6.31										
	$ZnCl_2$		0.15										
84	$FeCl_2$	6.8		$NaNO_2$		$CH_3COONH_4 + NH_4OH$		6.8-9.2	glass	4.2	150	90	17
	$NiCl_2$												
	$ZnCl_2$												

The table describes the metal chloride precursors used and their concentrations, when provided. The oxidizer and pH adjuster for the oxidizing solution are given as well as their concentrations. Ammonium acetate (CH_3COONH_4) appears to be the most popular pH adjuster, but potassium acetate (CH_3COOK) has also been used. Some papers stated the pH for both the reaction solution and the oxidizing solution. Reference 84 concludes that as the pH of the oxidizing solution is increased, so is the growth rate of the film.

The deposition conditions employed were provided in some of the earlier papers. For the most part, the solutions are carried into the chamber at a flow rate of 3 to 4 L/hr with the substrates rotating at 150 rpm and heated to 90°C. Glass naturally has –OH groups on their surface and therefore was the substrate of choice. It has also been reported that the nozzles should be mounted 9 cm above from the substrates and be separated by 12 cm to ensure sprays do not mix until making contact with the substrate

[84]. It was also reported that adhesion of Ni-Zn ferrite spinel films could be improved by first depositing a thin film of Fe_3O_4 spinel.

The literature has shown that the spin spray process has potential for being able to synthesize spinel-structured materials at very low temperatures. It therefore has the potential to be used to grown different thermistor oxides at conditions that could be incorporated in the CMOS fabrication process for the microbolometer.

Chapter 3

EXPERIMENTAL PROCEDURES

Nickel manganite thermistor thin films with a variety of compositions were synthesized using chemical solution deposition (CSD) and ferrite spinel thermistor films were synthesized using spin spray deposition. The resulting materials were characterized by X-ray diffraction (XRD) for phase analysis, and scanning electron microscopy (SEM) and transmission electron microscopy (TEM) for morphology, phase development, and local compositional homogeneity. In addition, the temperature coefficient of resistance (TCR) was determined as a function of composition and crystallization temperature.

3.1 Solution Preparation

Two types of nickel manganite solutions were used for thin film preparation: an acetate-based solution and an acetylacetonate-based solution. The solutions were batched stoichiometrically in terms of cation content. Several Ni:Mn ratios were investigated in order to both track the composition dependence of the electrical properties, and to interrogate the low temperature portion of the phase diagram shown in Figure 3.1.

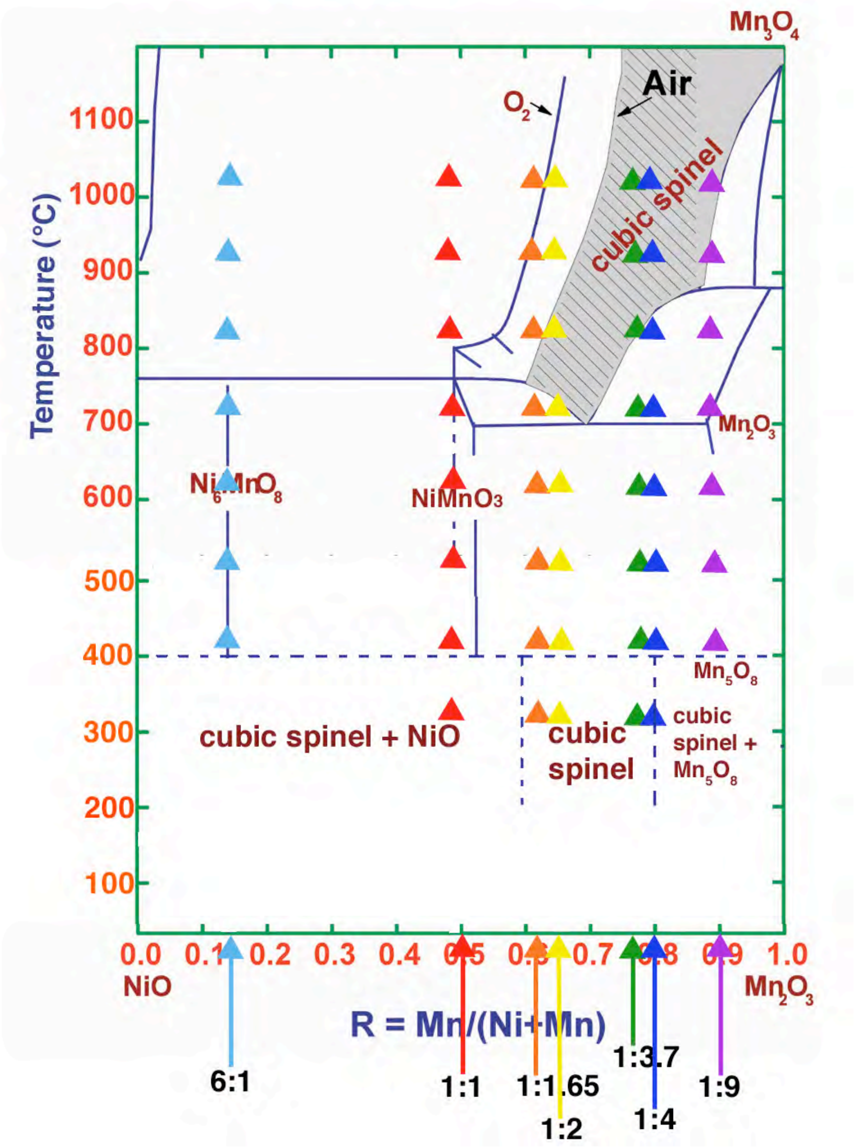

Figure 3.1: NiO – Mn_2O_3 phase diagram highlighting the area where cubic spinel forms; the seven different compositions synthesized in this study are labeled along with the heat-treatment temperatures employed [35, 36]

The phase diagram was mapped out based on powders synthesized using an oxalate route [34, 35, 36]. In this work, the seven compositions made include Ni:Mn ratios of 6:1, 1:1, 1:1.65, 1:2, 1:3.7, 1:4, and 1:9. Table 3.1 shows the percentages and chemical formulas for all of the compositions. It should be noted that the oxidation states are not known in each case.

Table 3.1: Summary of the seven different compositions synthesized

Ni:Mn ratio	**% Ni**	**% Mn**	**Chemical Formula**
6:1	85.7	14.3	Ni_6MnO_x
1:1	50.0	50.0	$Ni_{1.5}Mn_{1.5}O_x$
1:1.65	37.7	62.3	$Ni_{1.13}Mn_{1.87}O_x$
1:2	33.3	66.7	$NiMn_2O_x$
1:3.7	21.3	78.7	$Ni_{0.64}Mn_{2.36}O_x$
1:4	20.0	80.0	$Ni_{0.6}Mn_{2.4}O_x$
1:9	10.0	90.0	$Ni_{0.3}Mn_{2.7}O_x$

Acetic acid – based solutions were prepared by weighing nickel acetate tetrahydrate from Aldrich 99.998% purity ($(C_2H_3O_2)_2Ni_4 \bullet H_2O$) and manganese acetate tetrahydrate from Aldrich 99.99% purity ($(C_2H_3O_2)_2Mn_4 \bullet H_2O$) powders inside a LABCONCO glove box filled with Ar gas. The powders were combined and dissolved in acetic acid and DI (distilled) water in a round bottom flask. A 2:1 ratio of 99.7% acetic acid from Sigma-Aldrich ($C_2H_4O_2$) to DI water was employed. This was the minimum amount of water required to allow the acetate powders to fully dissolve. The smallest amount of water produced a solution with the best wetting ability. Solutions were batched to produce 30 mL of 0.3 molar solution. Batching calculations are given in Appendix A.

Complete dissolution of the powder occurred through mixing and heating the solution. The flask containing the solution was attached to a LABCONCO rotary evaporator and placed in a 70°C bath of silicone oil (See Figure 3.2). An Ar gas ambient was used. Magnetic stir bars were placed both in the silicone oil bath and in the solution flask. The liquid was mixed at 70°C for about 30 minutes or until a clear green solution was produced. Solutions were stored in glass bottles with Parafilm® wrapped around the lids. Acetic acid is very hydrophilic, and will absorb moisture from the air. This led to a solution shelf life of months. After this time, the solution wettability decreased.

Figure 3.2: LABCONCO rotary evaporator and silicone oil bath

Solutions were spun onto fractured pieces of p-type <100> silicon wafers from Nova Electronic Materials, LTD with 10,000 Å ±5% of thermally grown SiO_2 on the surface. The electrical resistivity of the wafers was between 5 and 25 Ωcm and the measured wafer thicknesses were between 475 and 575 μm. Prior to deposition, the wafers were blown off with N_2 gas to remove any particles. Water or organic surface layers were removed in a rapid thermal annealer (RTP-600S Tsunami^{TM} Series) by heating to 550°C for 1 minute. The solution was dispensed through a syringe with a 0.1 μm filter to cover the entire surface of the wafer as illustrated in Figure 3.3.

Figure 3.3: Illustration of spin coating

The wafer was then spun at 3000 rpm for 30 seconds using a Headway Research spin coater (Model PWM32). After each layer was spun, it was heat-treated on a 100°C hotplate for 1 minute, and then moved to a hotplate set at 270 - 300°C for 3 minutes. It was subsequently found that 300°C produced superior films. The process was then repeated. Between each layer the N_2 gun was used to blow off any dust particles that may have settled during the pyrolysis. In most cases, for every two layers that were deposited, the sample was annealed for one minute at temperatures between 430 and 1030°C in the RTA. A typical sample consisted of a total of eight spin-coated layers, yielding a thickness between 150-250 nm depending on temperature.

The acetylacetonate solution was prepared by MOD as described in the work of Kukuruznyak, Moyer, and Ohuchi [28]. Compositions with a Ni:Mn ratios of 1:2, 1:3.7, and 1:4 were batched using 95% nickel acetylacetonate from Aldrich ($Ni(C_5H_7O_2)_2$) and technical grade manganese acetylacetonate from Aldrich ($Mn(C_5H_7O_2)_3$). The powders were weighed and measured inside the glove box into two separate round bottom flasks. Methanol from Riedel-deHaen (CH_3OH) and >99% ethylene glycol from Sigma-Aldrich

($C_2H_2(OH)_2$) were added to the manganese in a volumetric ratio of 6:1 and the powder was dissolved while stirring on a hot plate at 60°C. 99.99% glacial acetic acid from Sigma-Aldrich ($C_2H_4O_2$) was added to the nickel source and the two were mixed at room temperature for a few minutes. The precursors and solvents were batched to produce 30 mL of 0.3 molar solution. After each cation was dissolved, the liquids were combined and the pH was adjusted to pH=1 using 69.5% purity nitric acid from Fluka. The solution was then mixed on a hot plate at 60°C for 30 minutes.

The Kukuruznyak paper suggested that addition of a borosilicate could potentially reduce the crystallization temperature of spinel to 500°C, although the crystallinity was not as good as films prepared without the borosilicate at higher temperatures. The acetylacetonate solution with the incorporation of the flux was prepared using a "hybrid sol-gel-MOD process" [54]. In this study, solutions were made with and without the borosilicate doping in order to compare the results. For solutions doped with borosilicate, a combination of 2 wt% of 99.999% TEOS (tetraethylorthosilicate) from Sigma-Aldrich ($C_8H_2OO_4Si$) and 2 wt% of 99% triethyl borate from Sigma-Aldrich ($C_6H_{15}BO_3$) were added. The solution was mixed for another 30 minutes at room temperature. The acetylacetonate solutions also exhibit a finite shelf life, after which precipitation is evident due to shifting of pH away from 1.

Thin films were prepared by dispensing the acetylacetonate solution over the entire surface of a cleaned silicon wafer and spinning at 3000 rpm for 30 seconds. After each layer, the film was pyrolyzed on a hot plate set to 500°C for 40 seconds. This caused an instantaneous color change of the film due to the removal of organics and the film densifying (decreasing the thickness). Every two layers, the sample was heat-treated in the RTA at temperatures ranging from 430 to 1030°C for 1 minute.

Films were also annealed using a tube furnace in order to vary the annealed time and the atmospheric conditions. The only heat-treatment the films saw before going into the tube furnace was the pyrolysis. Eight layers were spun onto the wafer, after each the pyrolysis procedure for the specific solution was performed. Films were placed directly into the tube furnace after it had already reached the desired temperature. Anneal times varied between one and 18 hours. Atmospheres used to heat-treat the films included ambient air, flowing oxygen, and flowing argon. Temperatures ranged between 300°C and 500°C, focusing on low-temperature crystallization.

3.2 Powder Preparation

The powder preparation process was used for high temperature XRD, and thermal analysis, as well as to follow reactions during the spin-spray process. High temperature XRD was used to follow the phase evolution of the 1:4 Ni:Mn from acetate precursors. Thermal analysis of the acetate and acetylacetonate powders allowed the identification of the organic removal temperature of the solution systems. In the case of the spin spray solutions, XRD of the resulting powder helped gauge reactions involving the Fe cations with the addition of the oxidizing solution.

The solution of interest was dried to a powder by holding it on a hot plate at 120°C for about a day in a fume hood. A lid partially covered the top of the container to limit contamination and to allow moisture to escape. Once the liquid was completely dried, a brown powder remained. The powder was ground in a mortar and pestle prior to thermal analysis and diffraction measurements.

3.3 XRD Analysis

XRD patterns were obtained on both films and powders in order to identify the phase content after heat-treatment. Zero background holders were used to analyze samples in both forms. For thin films, the sample was adhered to the holder using double-sided tape. For powder samples, grinding with a mortar and pestle were used to ensure powder homogeneity; a microscope slide helped pack the powder into the holder. Continuous scans were run on an X-ray diffractometer (Scintag - Model XPH-105) with a 2θ range from 15° to 70 or 85° and at a scan rate of 2.5° per minute.

High-temperature XRD was also used to follow the phase evolution in powders prepared from a 1:4 Ni:Mn solution. The dried powder was dispersed on a platinum strip heater. Step Bragg-Brentano theta-theta scans were run from 5° - 70° 2θ with a scan time of 2 seconds for every step of 0.02°. The scans were performed at room temperature (25°C), 350°C, 550°C, 650°C, 750°C, 850°C, and 950°C. A ramp rate of 10° per minute was used along with a 60 second delay before scanning.

Grazing angle X-ray diffraction was performed to analyze films while minimizing contributions from strong substrate peaks. Diffraction patterns were collected between 15 and 64° 2θ. A step theta-2 theta scan with a 0.02° step size was taken with holds of 0.5 seconds per step. Both high-temperature XRD and grazing angle XRD were performed on a Scintag diffractometer (Model: XGEN-4000).

Lattice constants were obtained from the highly crystalline films. A silicon powder standard was run prior to the films to calibrate the alignment of the detector. A theta-2 theta step scan was run with a 0.02° step size with a hold time of 3 seconds per step using an X-ray diffractometer (Scintag - Model XPH-105). Three of the most intense peaks (the 311, 400, and the 511) were scanned for each of the spinel films.

3.4 Aging and Thermal Treatments

A variety of heat treatments and aging experiments were employed to better understand the evolution of the properties and structure of nickel manganite films as a function of the thermal profile. Anneals at the film crystallization temperatures, (600 or 700°C for the samples used), were performed in two different environments, air and flowing nitrogen (N_2) gas. The films were placed directly into a small tube furnace equipped with an OMEGA CN-2010 series programmable controller. For the ambient air atmosphere, covers were placed on both ends of the furnace during the heat treatments. For the flowing N_2 ambient, <2 ppm moisture compressed N_2 gas was fed into the back of the furnace and flowed out the front cover through a bubbler filled with water at a rate of 3 mL/minute. The ramp rate used for heating was 10°C/minute while cooling ramps were set to 20°C/minute.

Similar tests were performed at the crystallization temperature, 600°C, on a series of films to examine any change caused by long anneals. Films were annealed for 24, 96, and 192 hours. A temperature profile with a heating rate of about 10°/minute to 600°C and a cooling rate of 20°/minute was used.

Aging tests were run to test the films in potential back-of-the-line conditions. Samples annealed at 400°C were characterized after prolonged exposure to 400°C in air to test the stability of amorphous films. Again, the films were placed directly into the tube furnace with covers on the front and back. The temperature profile used was a ramp rate of about 10°/minute to 400°C, followed by 1, 5, or 15 hours soaks, and then a ramp rate of 20°/minute back to room temperature.

A second aging test to measure the drift in resistance over time was performed. Films were held at 150°C in ambient air for 500 hours. Periodically, the films were removed from the oven, the resistance was measured at room temperature and they were placed back in the oven. The time intervals at which resistance was measured were approximately on a logarithmic scale due to the fact that the resistance tends to increase most during the first 100 hours.

3.5 Thermal Analysis

Simultaneous differential scanning calorimetry (DSC) and thermal gravimetric analysis (TGA) were run on the 1:3.7 and 1:2 nickel manganite powders to better understand the point at which the solvents and organics are removed, as well as the crystallization temperature. The SDT 2960 Simultaneous DSC-TGA instrument was used. TGA measures the weight loss or weight gain of a material as a function of temperature. It is able to indicate the mass of organics removed, the rate at which they burned off, and the temperature at which the organics were completely removed. DSC indicates the temperatures at which exothermic and endothermic reactions occur.

A powder dried from a solution was used for the thermal analysis. The powder was placed in a platinum crucible and the analysis was run in air because the films are pyrolyzed and annealed in air. The thermal analysis furnace program, shown in Figure 3.4, had a ramp rate of 10°/minute up to 950°C where it was held for 10 minutes before cooling at 20°C/minute to room temperature.

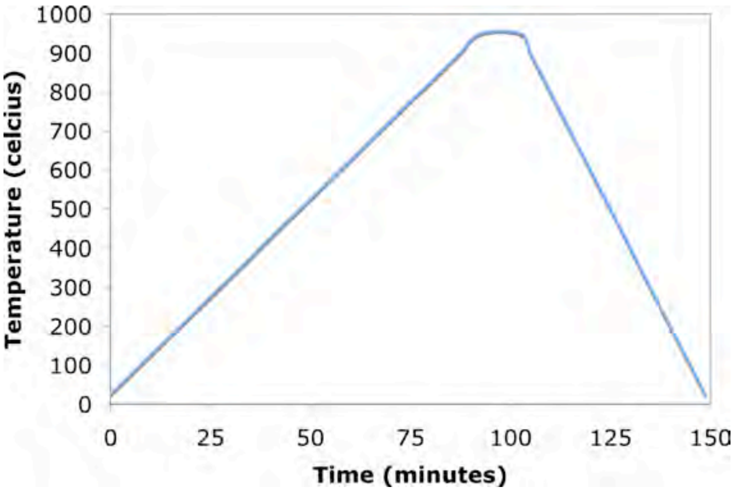

Figure 3.4: Thermal analysis furnace program with a 10°C/minute ramp up rate

3.6 SEM

A Hitachi S-3000H SEM (scanning electron microscope) was used to image both cross sections and the surface of the nickel manganite films. For cross sections, samples were mounted on cross-section sample holders using silver paste and carbon tape to minimize charging. Conducting tape was used to border the edges of the film, ensuring electron pathways to the sample holder. Once mounted, the cross section was sputter coated with a thin layer of gold. An accelerating voltage of 5 kV was used in combination with a working distance of 5 mm in order to observe the film grain size. For viewing the surface of the films a small fractured piece was adhered using carbon tape to a sample holder. A small piece of the conductive tape was placed on the surface of the sample to connect it to the holder in order to minimize charging. The films were again sputtered with a thin layer of gold before placing them in the vacuum chamber.

3.7 FESEM

The FESEM (field emission scanning electron microscope) was also used to image the film cross sections. A field emission microscope can operate at much lower accelerating voltages than a conventional SEM. It is typically used between 1 and 5 kV, but has a range of a few hundred volts to 30 kV. Higher resolution can be attained with an electron beam that is typically brighter and better-focused than conventional SEMs. FESEMs can be used to view less conductive materials, such as organics and polymers [85].

The nickel manganite films were cleaved and clamped into a cross sectional sample holder. Silver paste was used to make an electrical contact between the film and the sample holder. About 15-20 Å of iridium was sputtered onto the exposed cross-section of the film to minimize charging. For FESEM work, iridium is chosen over gold because it can better protect the film from beam damage at higher magnifications (<200,000X) [86]. Gold is used at lower magnification (<2000X) [86]. An accelerating voltage of 1 kV and a current of 20 μA was used in combination with a working distance of 2.5 mm.

3.8 TCR Measurements

The nickel manganite films were electroded by sputtering 300 nm of gold through a shadow mask onto the surface. The shadow mask utilized a series of strip electrodes 200 μm wide and 5 mm long. Four strips were placed 200 μm apart from each other while one set of strips has a 400 μm spacing as shown in Figure 3.5.

Figure 3.5: Schematic of the strip electrodes deposited onto the films

Current versus voltage (I-V) measurements were first obtained to ascertain whether the electrical contacts were ohmic. I-V curves were taken as a function of temperature using a two-probe setup and a heated stage, as shown in Figure 3.6.

Figure 3.6: A two-probe setup used for TCR measurements

A Hewlett Packard 4140B pA Meter/DC Voltage Source was used with a LabView program to collect the data. Voltages between -7.0 V and 7.0 V were applied in steps of 1.0 V; at each voltage a hold time of 10 seconds was used before the current was collected. I-V data were obtained at different temperatures. The resistance was obtained from the inverse of the I-V slope. Resistance is related to resistivity by a geometrical factor as shown in Equation 3.1, where l is the distance between electrodes and A is the area of the thin film underneath the electrode (film thickness times the length of the electrode).

$$R = \rho*(l/A) \qquad \text{Equation 3.1}$$

Resistivity is the inverse of conductivity and therefore has a similar temperature dependence as the resistance (Equation 3.2). TCR is identical to the temperature coefficient of resistivity.

$$\rho = \rho_o \exp(E_a/kT) \qquad \text{Equation 3.2}$$

TCR values reported in this thesis were determined from the slope of the natural log of resistance versus temperature data. They can also be calculated at room temperature, 298 K, using Equation 3.3.

$$\%TCR = - E_a/kT^2 * 100 \qquad \text{Equation 3.3}$$

Equation 2.3 gives the TCR value as a percentage, which is how it is most commonly found in the literature. The units for TCR are given in %/°C or %/K. For the nickel manganite films, the values are negative.

3.9 Transmission Electron Microscopy (TEM)

TEM analysis was used to help better understand the microstructure and structure of the nickel manganite thin films. As mentioned in the literature review, in bulk thermistor materials, phase decomposition into a rocksalt, NiO phase has been observed [25]. It has been reported that multiple anneals are required in order to synthesize a powder that is mainly spinel [41]. The results of such a decomposition is shown in Figure 3.7 for a medical grade bulk thermistor tape cast nickel manganite sample from Sensor Scientific, Inc.

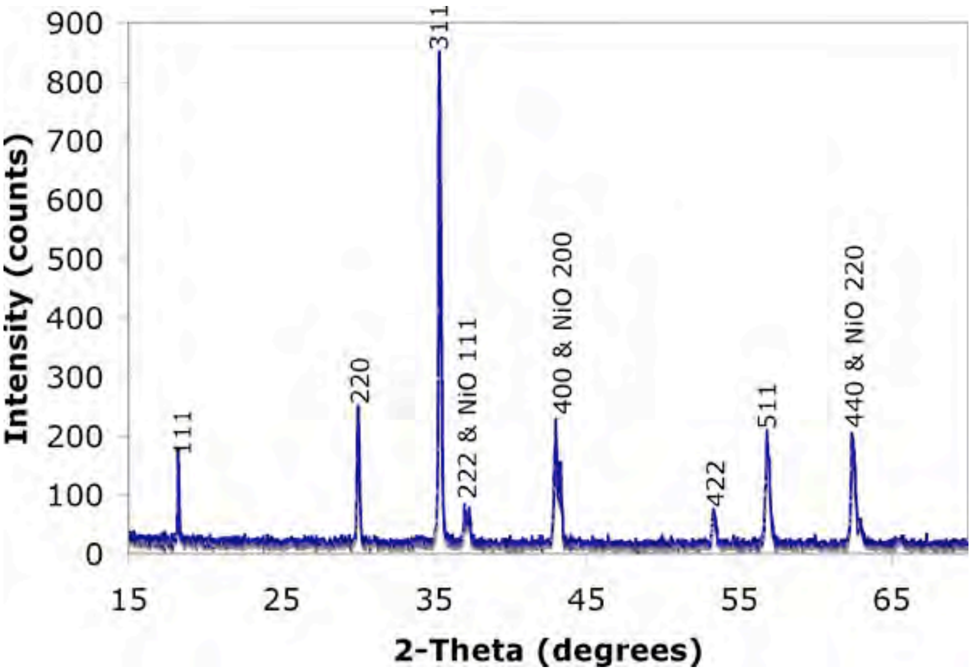

Figure 3.7: XRD pattern of a medical grade bulk thermistor nickel manganite spinel sample from Sensor Scientific, Inc. The indexing corresponds to the spinel phase unless otherwise noted.

The d-spacings of the spinel phase and the NiO rocksalt phase are very similar at low 2θ values. In this pattern there are three peaks from NiO: 111, 200, and 220, that are present next to the 222, 400, and 440 spinel peaks. Figure 3.8 provides a zoomed in plot of the 111 peak in the NiO structure to illustrate the presence of the two phases.

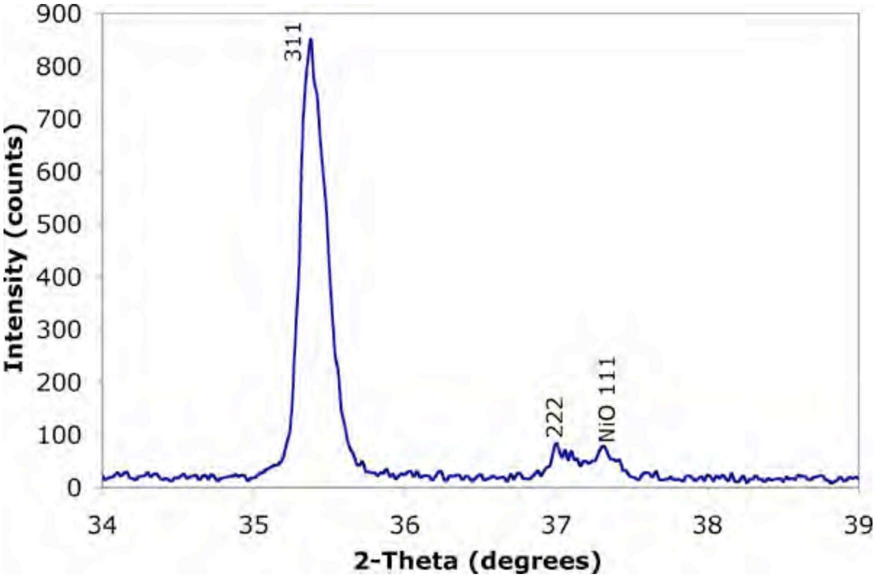

Figure 3.8: XRD pattern showing the NiO decomposition of the bulk spinel thermistor sample from Sensor Scientific, Inc.; the indexing corresponds to the spinel phase unless otherwise noted.

However, it was found that it was difficult to detect formation of rocksalt second phases via X-ray diffraction on thin films. Thus, TEM was employed. Three samples were examined, a film with a Ni:Mn ratio of 1:4 heat treated at 900°C, a film with a Ni:Mn ratio of 1:2 crystallized at 800°C, and one with a Ni:Mn ratio of 1:1 heat-treated at 900°C. The first two were synthesized within the spinel region of the bulk phase diagram and XRD showed them to be phase pure spinel. The third was synthesized within a region of mixed phases, spinel and NiO. Cross sections of the nickel manganite thin films were prepared by mechanical polishing to 20-30 μm followed by ion milling to perforation.

A JEOL 2010F (200 kV) microscope, along with a field emission gun (FEG), a LaB_6 electron gun, and a Gatan Image Filter (GIF) were used for the TEM characterization. The crystallographic phases present were determined using high-resolution (HR) TEM. Compositional information was found using an energy dispersive X-ray spectrometer (EDS). Elemental maps were created using energy-filtered transmission electron microscopy (EFTEM) in order to identify the spinel-rocksalt phase decomposition. Dr. Jing Li completed the TEM work.

3.10 Spin Spray Deposition

Spin-spray deposition was explored as a potential low processing temperature alternative to sol-gel processing, as described in the literature review. Two aqueous solutions were batched and deposited separately. They combine and react at the substrate. The oxidizing solution was batched to 2000 mL with a 0.95 M concentration of 98% ammonium acetate from Sigma-Aldrich ($C_2H_7NO_2$), a 0.012 M concentration of 99.999% sodium nitrite from Aldrich ($NaNO_2$), and DI water. The reaction solution was batched to 2000 mL with a 0.2 M concentration of >98% iron chloride tetrahydrate ($FeCl_2*4H_2O$) from Fluka and DI water. Solutions were mixed at room temperature on a stir plate for about 20 minutes or until the precursors were completely dissolved.

Substrates were blown off with a N_2 gun and either taped using Kapton tape or screwed down onto the heated table (Figure 3.9) in the deposition chamber (Figure 3.10).


Figure 3.9: Heated substrate holder in spin spray system


Figure 3.10: Spin spray equipment

The substrates used were either VWR glass microscope slides or NOVA Si wafers with 10,000 Å of thermal oxide. Both have OH^- groups on the surface. The nozzle height was set to be about 10 cm from the substrates. The substrate heater was turned on and stabilized at 90°C before DI was pumped though at 0.6 L/hour using diaphragm pumps pressurized with N_2 gas flowing at 7.5 mL/minute. Two separate Tygon tubing lines carry the solutions to two different nozzles, one for each solution. The end of the Tygon tubing that is placed in the beaker with solution was weighted to hold the tubing in the liquid (See Figure 3.11).

Figure 3.11: Fixture to hold tubing in the solution during the deposition

When the DI water sprayed into the chamber, the substrate temperature immediately dropped about 30°C. To allow the heater to compensate for this, the water flow was maintained for about 20-30 minutes. It has been observed that with the equipment used in this thesis the temperature never returns to 90°C, but will equilibrate around 70°C. During this stabilization, the solutions were mixed continuously. When the chamber equilibrated, one tube was placed in the oxidizing and the other in the reaction solution, in order to carry the reactants to the substrate. 50 minutes were required to achieve a film thickness of about 300-500 nm. Following deposition, the heat was turned off and the hoses were placed back into the beakers containing DI water. The chamber was allowed to come back to room temperature before stopping the water flow and the N_2 gas flow.

Chapter 4

RESULTS AND DISCUSSION

4.1 Introduction

Seven different compositions in the nickel manganite system were synthesized using the two types of solutions described in the Experimental Procedure chapter. Structure-processing relationships were studied using X-Ray Diffraction (XRD); electrical properties of the films were measured using current-voltage tests; thermal analysis was performed on the two types of solutions; and the microstructure and chemistry of the films were observed using SEM and TEM characterization. Critical to this study was a determination of the stability of the film properties through aging experiments, understanding phase decomposition, and finding low temperature processing routes for synthesizing high TCR and low resistivity films.

Two synthesis routes were explored for the processing of thermistor materials chemical solution deposition (CSD) and the spin spray technique. CSD was chosen due to its simplicity and flexibility in synthesizing a wide range of stoichiometries. It is important to note that the materials science that was learned can be translated to other processing routes, such as sputtering, that may be more compatible with silicon micromachining. As an alternative method for low temperature deposition, spin spray methods were also investigated.

Throughout this chapter, samples prepared by chemical solution deposition are designated according to composition and the solvent system used for the precursor solutions. The seven compositions made include the following Ni:Mn ratios: 6:1, 1:1, 1:1.65, 1:2, 1:3.7, 1:4, and 1:9 (See Table 4.1).

Table 4.1: Summary of the seven different compositions synthesized for CSD films

Ni:Mn Ratio	**% Ni**	**% Mn**	**Chemical Formula**
6:1	85.7	14.3	Ni_6MnO_x
1:1	50.0	50.0	$Ni_{1.5}Mn_{1.5}O_x$
1:1.65	37.7	62.3	$Ni_{1.13}Mn_{1.87}O_x$
1:2	33.3	66.7	$NiMn_2O_x$
1:3.7	21.3	78.7	$Ni_{0.64}Mn_{2.36}O_x$
1:4	20.0	80.0	$Ni_{0.6}Mn_{2.4}O_x$
1:9	10.0	90.0	$Ni_{0.3}Mn_{2.7}O_x$

As described in chapter 3, acetate-based aqueous solutions and acetylacetonate nonaqueous solutions were both used.

4.2 Processing Studies of Nickel Manganite

Initial processing studies were undertaken to assess the window in temperature and composition in which films with the spinel crystal structure could be synthesized. In bulk thermistors, the high-temperature stable spinel region of the phase diagram is chosen for processing. High TCR and excellent property stability has been shown to exist in materials with this structure. Phase development was determined by using XRD and TEM. Comparisons were made between films prepared with various annealing temperatures, thicknesses, compositions, and solution chemistries. All films were compared to the phase diagram to locate discrepancies and similarities.

4.2.1 Crystallinity as a Function of Annealing Temperature

To assess the temperature required for phase development, films of a variety of Ni:Mn ratios were annealed for one minute in air in a rapid thermal annealer (RTA). Typical film thicknesses were 150 nm. Temperatures between 300°C and 1030°C were chosen to heat-treat the different compositions in order to assess the phase formation. The accuracy of the hold temperature should be within ± 10°C, excluding the initial overshoot. Due to lack of crystallization in the 430°C films (shown below), some pyrolyzed films were heat treated at temperatures from 300 to 500°C for longer times in a tube furnace in low pO_2 atmospheres instead of the RTA. The tube furnace was measured to be within ± 10°C of the set temperature at the location of thermocouple placed in the center of the silica tube. There was about a two-inch hot zone in the middle of the silica tube where the samples were placed. The two different processing routes, RTA annealing versus low pO_2 annealing, are discussed separately.

Of particular interest were the temperature ranges over which the cubic spinel phase was reported to form. For the engineering aspects of this project, the lower temperature spinel regions were of greater interest, but the overall understanding of why and how the different phases form is of scientific interest. Therefore different processing routes and conditions were examined. According to the combined phase diagram incorporating Wickham's and Tang's results (See Figure 4.1), the spinel structure should not be formed between 400°C and 705°C.

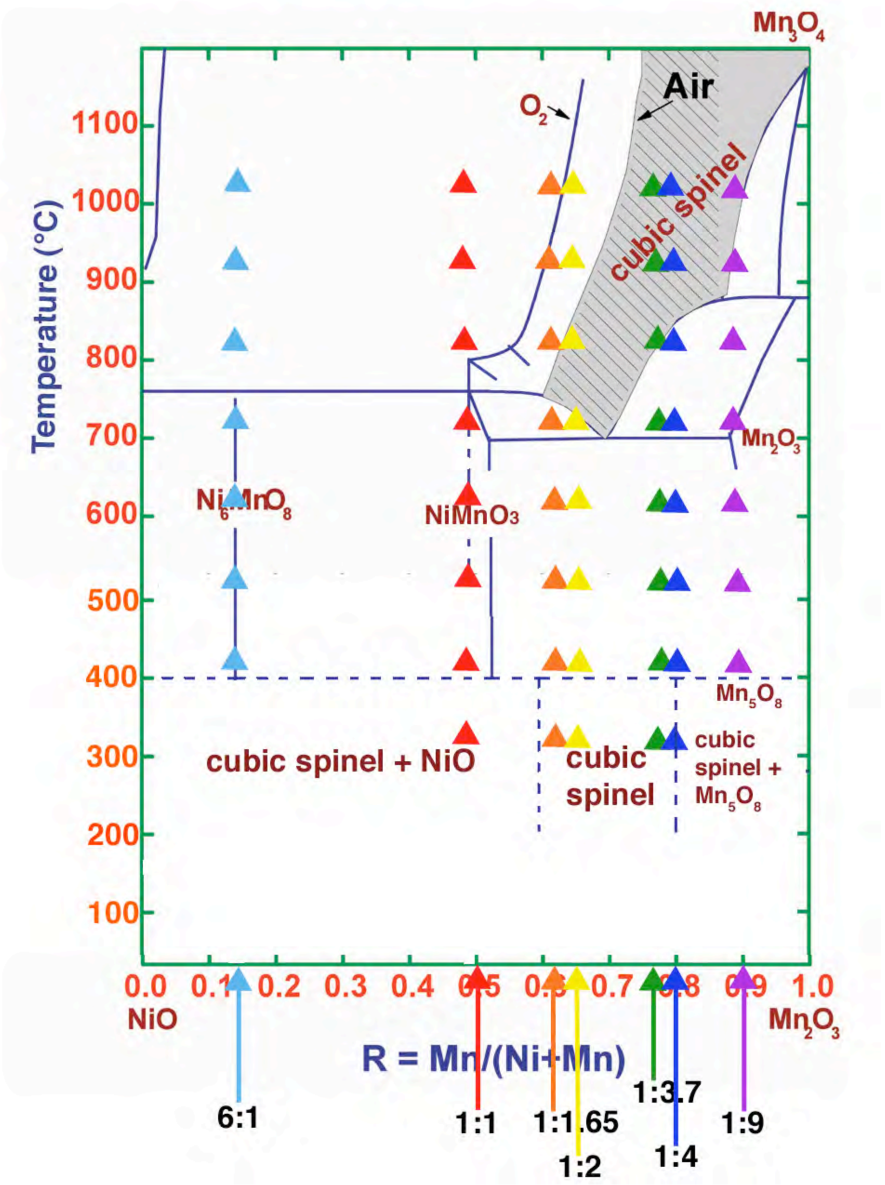

Figure 4.1: NiO-Mn_2O_3 phase diagram with synthesized films marked with triangles [35, 36]

The eutectoid temperature was reported by Wickham to be 705°C. Below 705°C $NiMnO_3$ and Mn_2O_3 should be present [35]. However, it has been pointed out by several groups that a cation deficient spinel can be prepared at lower temperatures (e.g. below 400°C) particularly in somewhat reducing conditions [36]. This is believed to be because the decomposition from spinel into the ilmenite and bixbyite phases requires oxygen and may not occur in an inert atmosphere [36]. Thus, the first goal of this research was to determine whether or not the chemical solution deposition routes explored here would follow similar patterns for phase development in films as in powders and ceramics.

4.2.1.1 Rapid Thermal Annealing

One set of films was synthesized using a pyrolysis step followed by annealing in a RTA. RTA is known for its quick ramp rates (hundreds of degrees a minute) and short anneal times. The following results are organized by composition (as shown in Figure 4.1).

4.2.1.1.1 1:1 Ni:Mn Films from Acetate Precursors

The phase diagram shows a line compound for Ni:Mn ratios of 1:1 for temperatures below 760°C. Between 400°C and 760°C the films should show two phases, the ilmenite and Ni_6MnO_8. However, for the thin films from acetate precursors, X-ray diffraction (XRD) shows growth of spinel peaks as low as 630°C. During thin film processing it is possible that the organics present can cause low *local* oxygen partial pressures, yielding an environment with insufficient oxygen to enable the formation of ilmenite and Ni_6MnO_8, even though an air ambient was used. These phases both have high oxidation states for manganese, 3+ and 4+. Above 760°C, the 1:1 composition should show a two-phase region of spinel and rocksalt NiO phases. However, it was found that between 630°C and 1030°C, only the spinel phase appears according to the XRD diffraction patterns in Figure 4.2.

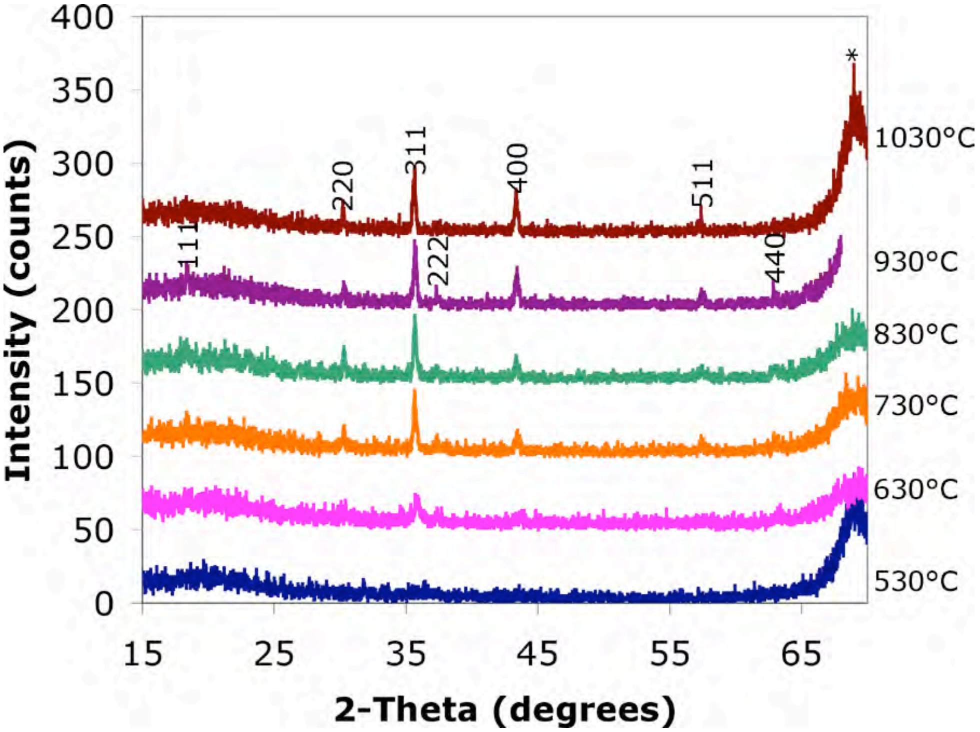

Figure 4.2: XRD patterns of films made from the Ni:Mn 1:1 acetate solution and crystallized at temperatures ranging from 530°C to 1030°C for one minute in the RTA. The indexed diffraction peaks correspond to a cubic spinel with a lattice parameter of 8.345 Å ± 0.003 Å and thicknesses range from 150 nm for denser films annealed at higher temperatures to 230 nm for the low temperature annealed films. The "*" peak is due to the substrate. Here and in all subsequent XRD data, the patterns for different samples are offset for clarity.

In particular, there was no sign of the thermodynamically stable $NiMnO_3$ or NiO phases crystallizing in these films above 730°C after a one minute anneal using a RTA. Instead, a cubic spinel was identified.

In previous research on nickel manganite powder processing, a cation deficient spinel and rocksalt, NiO, phases were shown to crystallize below 400°C and stoichiometric phases above 760°C [35, 36]. In particular, powders with a nickel to manganese ratio of 1:1 from oxalate precursors did not readily produce the ilmenite phase [87]. Instead, thermal analysis of the organic precursor illustrates the formation of the cubic spinel phase dominating, unless between 600°C and 700°C the material is quenched to form the ilmenite phase [87]. In this work, no clear ilmenite peaks were detected in the XRD patterns. TEM analysis could help to determine if two phases in fact exist. Samples heat-treated at 300°C and 400°C (not shown) appear amorphous with XRD patterns similar to the 530°C film.

It was anticipated that the films prepared with a Ni:Mn ratio of 1:1 would show a spinel phase and a rocksalt-structured phase when annealed above 760°C. However, as shown in Figure 4.3, slow scan XRD patterns of the 1:1 films annealed at temperatures between 830 and 1030°C do not show any NiO peaks even though these samples fall within the two-phase region on the phase diagram.

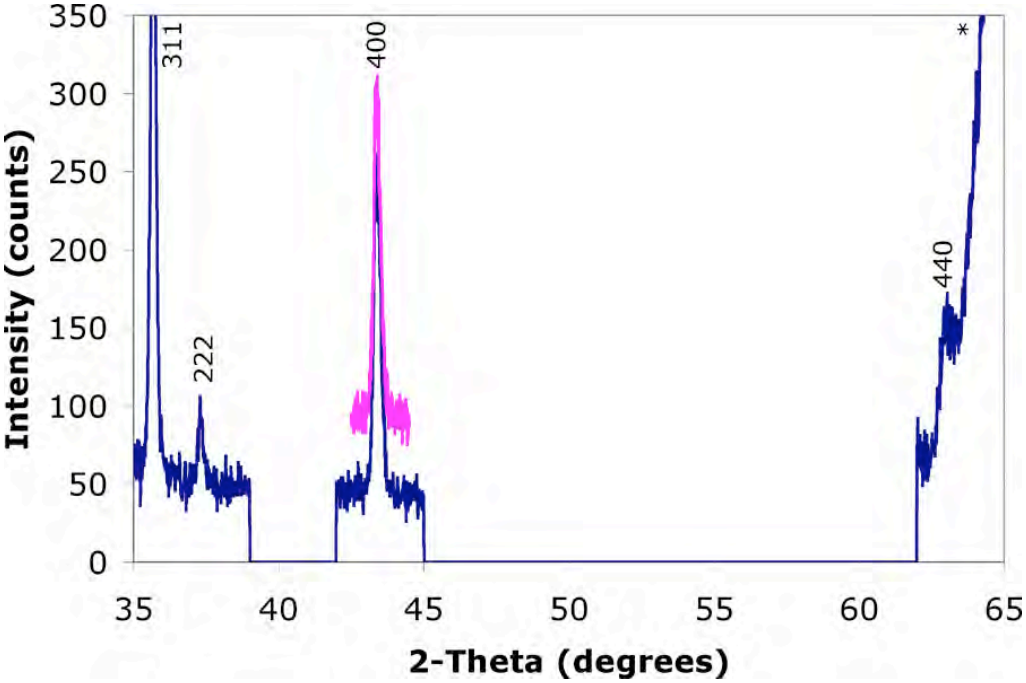

Figure 4.3: Slow count time XRD pattern of Ni:Mn 1:1 acetate film annealed at 830°C showing spinel peaks. No peak splitting characteristic of the NiO phase was detected. The “*” peak is due to the substrate.

Thus, it became interesting to determine whether the samples were, indeed, single-phase (presumably stabilized by some sort of kinetic limitation), or whether the second phase simply could not be detected by X-ray diffraction.

As a second interrogation method, TEM analysis was employed. A cross-sectional sample of the 1:1 films annealed at 930°C was prepared for TEM analysis in order to determine if the NiO phase was present. EELS elemental mapping with the Mn and Ni L2 and L3 edges was used to examine the distribution of Ni and the Mn across the film. Figure 4.4 displays sets of lower magnification, a, b, and c, and higher magnification, e, f, and g, cross sectional TEM images and corresponding EELS maps for nickel and manganese distributions through the Ni:Mn 1:1 film prepared from an acetate solution and annealed at 930°C. The TEM work was performed by Dr. Jing Li.

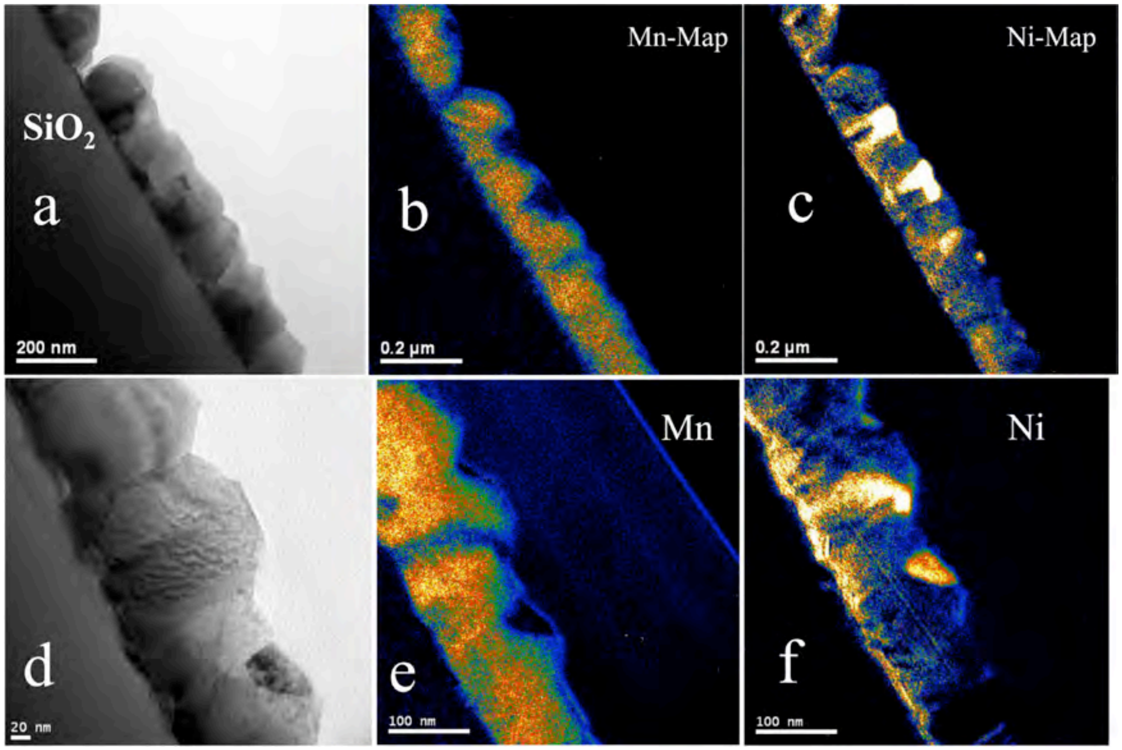

Figure 4.4: TEM images and EEL elemental mapping of nickel and manganese within an acetate film with a Ni:Mn ratio of 1:1 annealed at 930°C

The grain size is between 100 nm and 150 nm and in many regions the film appears to have a single grain across the thickness. The nickel and manganese mapping show significant inhomogeneity within the film. The areas rich in nickel correspond to regions with little manganese. It was hypothesized that locally high concentrations of Mn are the results of spinel rich regions while where there are high concentrations of Ni, the rocksalt phase is present. To help prove this statement, the decomposition was also observed using HRTEM and EDS. HRTEM was used to identify the periodicity of the lattice. The spinel phase shows a (hkl) d-spacing of two times that of the rocksalt phase. Figure 4.5 shows the HRTEM image of the 1:1 930°C acetate film projected along the <011> direction.

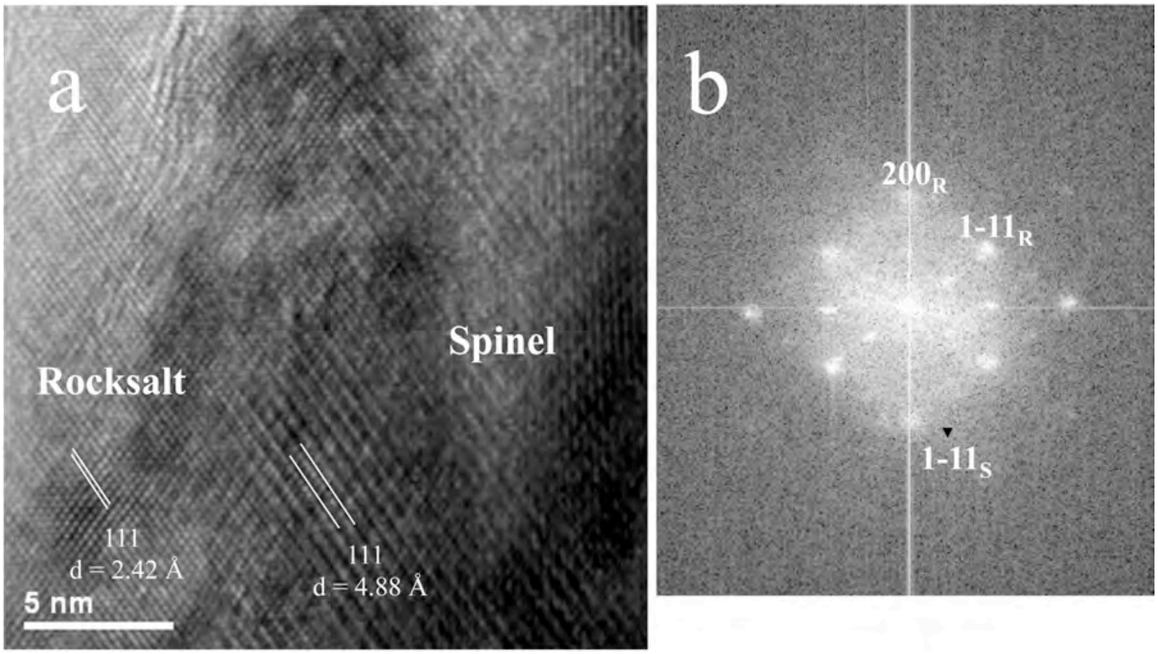

Figure 4.5: (a) HRTEM image of the Ni:Mn 1:1 acetate film annealed at 930°C and (b) the Fourier transform of the image. The subscript S is used to denote the spinel and the subscript R is used for rocksalt.

Figure 4.5a is an image taken within a single grain of the 1:1 film along the [011] orientation. Regions with both the spinel structure (d = 4.88 Å) and the rocksalt structure (d = 2.42 Å) have been identified within this grain. The error on the d-spacings is greater than ±0.01 Å. The large error is due to the fact it is difficult to find the exact zone axis orientation for a grain because the film is both fine grained and polycrystalline. As expected, the d-spacing of spinel is approximately twice that of the rocksalt phase. Figure 4.5b represents the Fourier transform of the HRTEM image from a. The Fourier transform is used to confirm the orientation is in fact along the <011> direction.

The EDS spectrum obtained at different regions within a single grain of the 1:1 film show inhomogeneity in the amount of nickel and manganese present. Figure 4.6 shows the intensities of Ni and Mn at two different regions within a grain (two separate spectra).

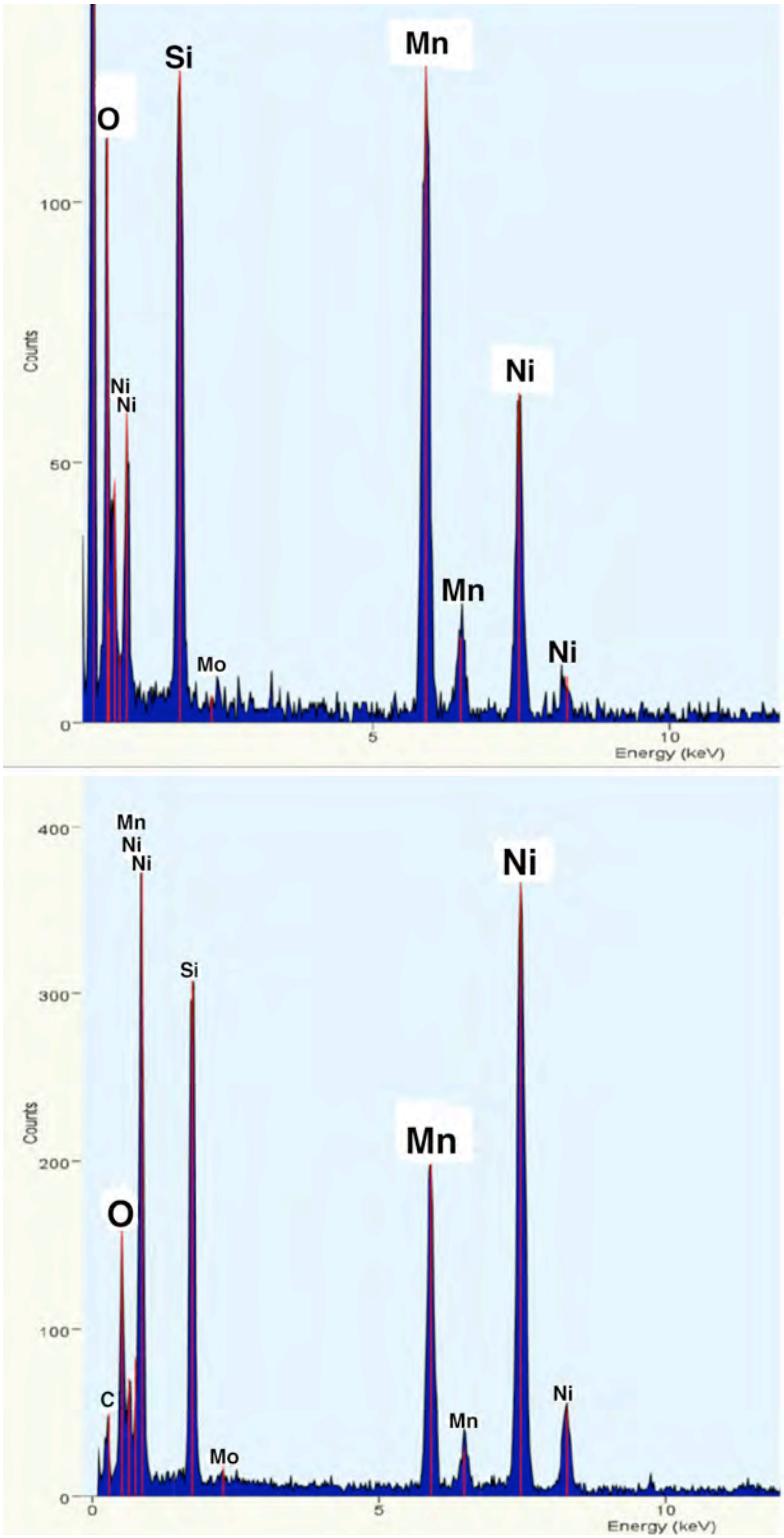

Figure 4.6: EDS spectra within a single grain of spinel in the Ni:Mn 1:1 acetate film annealed at 930°C

The spectrum on the top shows elemental intensities that would correspond with the spinel phase region while the spectrum on the right has a much larger nickel intensity that would be consistent with the rocksalt, NiO structure. The grains with the spinel phase are on the order of 100 to 150 nm in size. Thus, the TEM analysis shows that the samples do, in fact, decompose into two phases. It is believed that there are two principle reasons why this decomposition was not detected in the X-ray diffraction measurements. First, the size of the NiO crystallites is quite small, on the order of only 10's of nanometers, if it is occurring within a grain of spinel. In addition, the NiO may be coherently strained to the spinel. This would lead to the NiO having exactly half of the lattice parameter as the spinel, and therefore separate peaks would not be observed in the XRD patterns. Due to the comparatively large error in the lattice parameters determined by TEM, it was not possible to conclude whether or not the rocksalt is coherently strained to the spinel phase.

4.2.1.1.2 1:3.7 Ni:Mn Films from Acetylacetonate Precursors

Films with 1:3.7 Ni:Mn ratios from acetylacetonate -based solutions display the spinel structure after heat-treatments at 630°C to 1030°C. For one minute RTA anneals below 530°C, the films appear X-ray amorphous. Figure 4.7 illustrates the crystallization as a function of temperature.

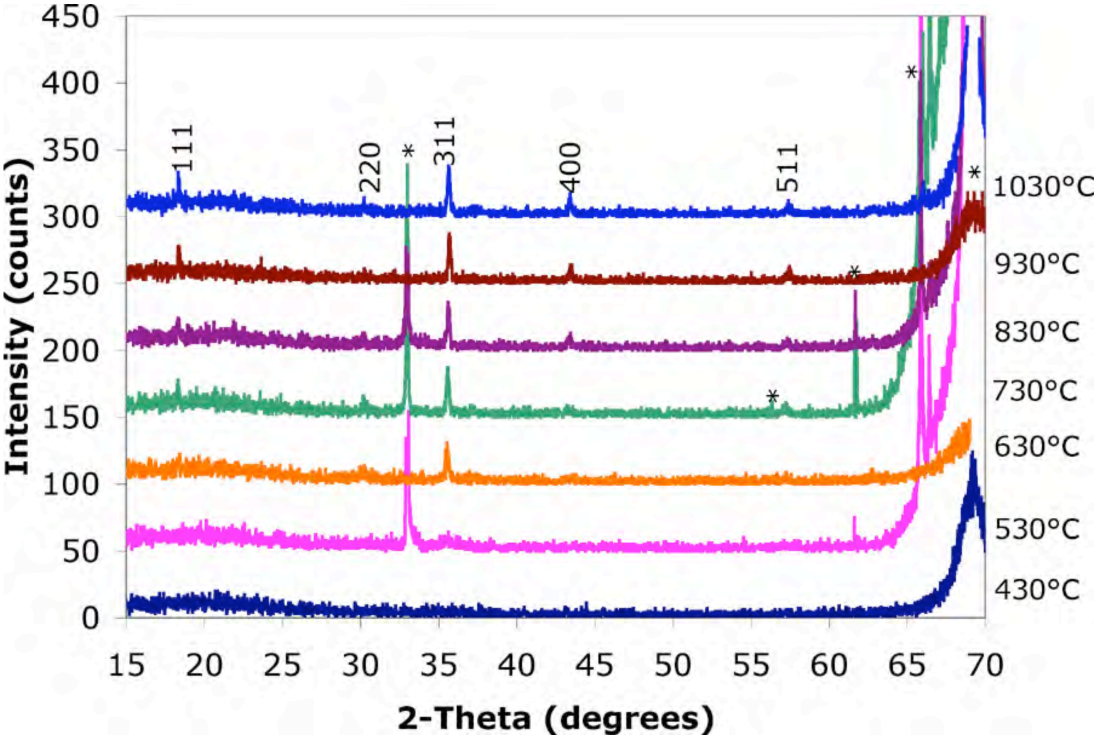

Figure 4.7: XRD patterns of films made from the Ni:Mn 1:3.7 acetylacetonate solution and heat-treated at temperatures ranging from 430°C to 1030°C for one minute in the RTA. Indexed peaks correspond to the cubic spinel phase and the "*" peaks are due to the substrate. Most of the indexed diffraction peaks correspond to a cubic spinel with a lattice parameter of 8.348 Å ± 0.004 Å. Film thicknesses range from 150 nm for denser films annealed at higher temperatures to 230 nm for the low temperature annealed films.

The phase diagram shows a single-phase spinel region above 850°C for this composition. Between 850°C and 705°C, a two-phase region of Mn_2O_3 and spinel should exist. No signs of Mn_2O_3 were detected after the one-minute anneals were performed. This might be associated with low local pO_2 from organics remaining in the film. In particular, removal of residual carbon in the film will produce an atmosphere richer in CO and CO_2, and depleted in oxygen. Below 705°C should be another two-phase region of Mn_2O_3 and $NiMnO_3$, neither of which were identified by XRD after the initial anneal. If a low local pO_2 exists, there is not enough oxygen present to oxidize the manganese to its higher oxidation state as would be required in these two structures. The spinel phase is favored and observed experimentally.

The 1:3.7 acetylacetonate-based composition was also synthesized with a borosilicate (a ratio of 1:1 B:Si) flux to assess the impact on crystallization temperature. A 2% by weight doping was added to the solution as explained in Chapter 3. Figure 4.8 demonstrates the poor crystallization that resulted in the films.

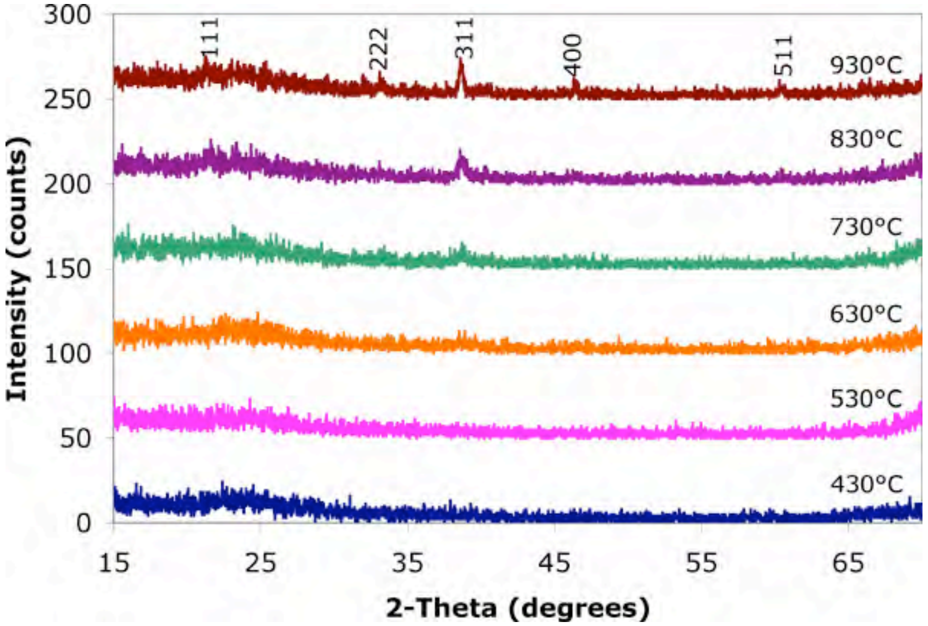

Figure 4.8: XRD patterns of films made from the Ni:Mn 1:3.7 acetylacetonate solution doped with borosilicate and crystallized at temperatures ranging from 430°C to 930°C for one minute in the RTA. The indexed diffraction peaks correspond to a cubic spinel. The films thicknesses range from 150 nm for denser films annealed at higher temperatures to 230 nm for the low temperature annealed films.

Compared to the films in Figures 4.7 and 4.9, these are clearly not as crystalline. The decrease in crystallinity is consistent with previous reports [58]. With one minute RTA anneals, the diffraction peaks do not begin to narrow until 930°C. The thicknesses are similar to those of undoped films from Figure 4.7, suggesting the borosilicate dopant was the main reason for the decrease in X-ray peak heights. Consequently, work on borosilicate - containing films was not pursued further.

4.2.1.1.3 1:3.7 Ni:Mn Films from Acetate Precursors

Films with Ni:Mn ratios of 1:3.7 were also made from an acetate-based solution. The results are different from those shown in the acetylacetonate films (Figure 4.7). The acetate films appear to be more consistent with the phase diagram, as shown in Figure 4.9. This is correlated with the observation that higher temperatures were required for full removal of the organics from the acetylacetonate solutions (See section 4.2.1.1.2).

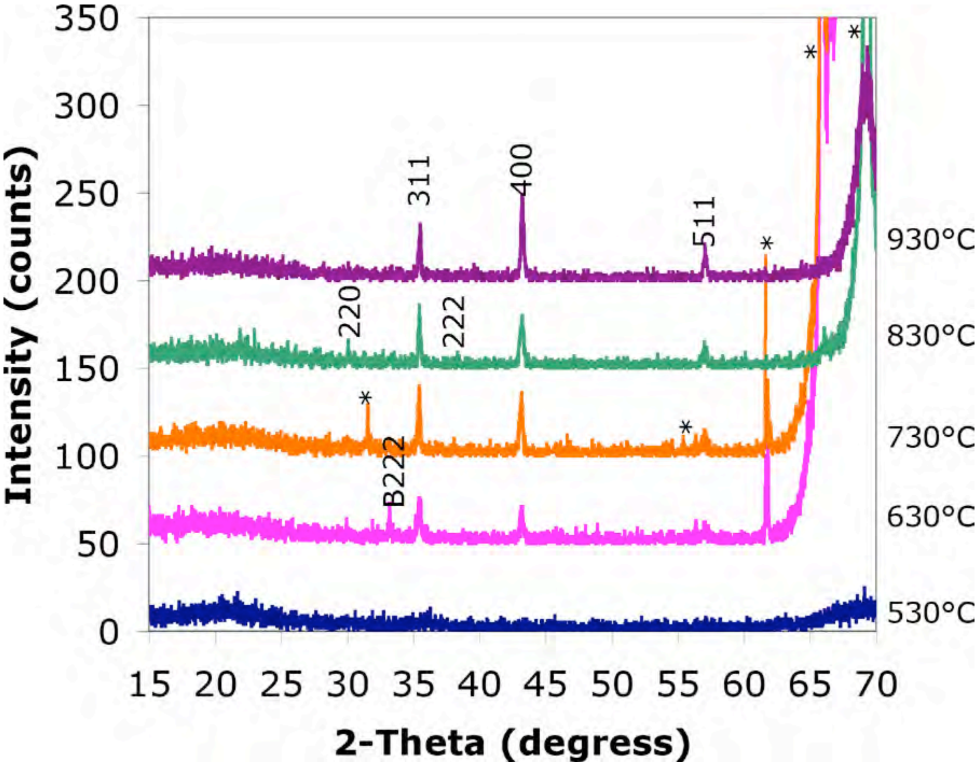

Figure 4.9: XRD patterns of films made from a Ni:Mn 1:3.7 acetate solution and heat-treated at temperatures ranging from 530°C to 930°C for one minute in the RTA. Indices correspond to those of a nickel manganite spinel with a lattice parameter of 8.34 Å ± 0.02 Å unless otherwise marked. Peaks with a "B" are from the bixbyite phase; those with an "*" are from the substrate. The film thicknesses range from 150 nm for denser films annealed at higher temperatures to 230 nm for the low temperature annealed films.

A second phase of bixbyite, Mn_2O_3, can be identified as "B" in the film annealed at 630°C. At this temperature two phases are suppose to coexist, ilmenite and bixbyite. The spinel phase is still present. At temperatures above 730°C, only spinel should be present according to the phase diagram and the results show just this.

It was hypothesized that the pyrolysis procedure might be responsible for the observed differences between films from the two different solutions. The acetate films were heated to 100°C for 1 minute and then held at 300°C for 3 minute to remove the organics. These temperatures were determined after thermal analysis, (see section 4.2.1.1.3.1). In contrast, the acetylacetonate films were pyrolyzed at 500°C for 40 seconds. If some organics remain after pyrolysis, local low oxygen pressures could develop during annealing, which could influence the phase assemblage [38].

4.2.1.1.3.1 Thermal Analysis of the Two Solutions

A low pO_2 anneal environment has been reported to stabilize the spinel phase at low temperatures. To determine whether residual organics could influence the phase development in the nickel manganite films, thermal analysis was performed to better understand when organics are removed from the CSD films. To facilitate the formation of the low temperature metastable spinel phase the pyrolysis procedures can be optimized to leave a small amount of organics to create local low pO_2 around the film.

DTA/TGA curves for acetate and acetyacetonate solutions on heating at 10°C/minute (Figure 3.4) were compared. The thermal analysis shows above 250°C, the powder from the acetate solution underwent a 50% weight loss. The exothermic reaction associated with this weight loss does not finish until about 320°C (Figure 4.10).

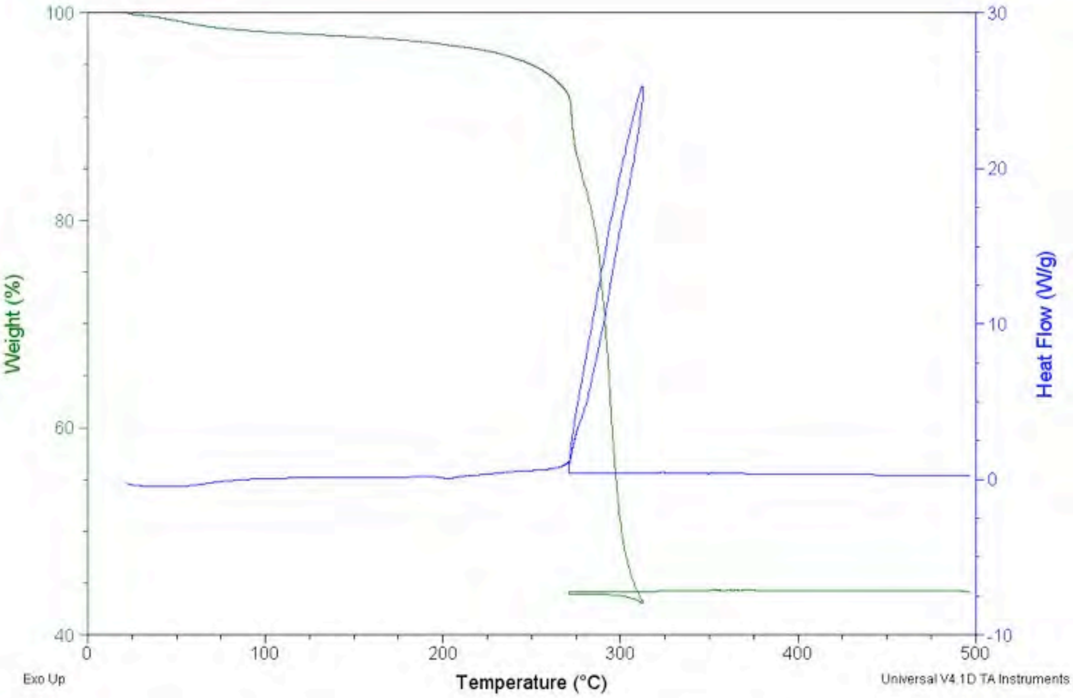

Figure 4.10: TGA and DSC curves for Ni:Mn 1:2 nickel manganite powder from an acetate solution

This suggests that there may be some retained organics in the films following a pyrolysis at 300 °C that could, indeed, lead to low local oxygen partial pressures. In contrast, the powder dried from a 1:3.7 acetylacetonate solution doped with borosilicate shows that the organics are removed around 425°C. A 7% weight loss was observed (Figure 4.11).

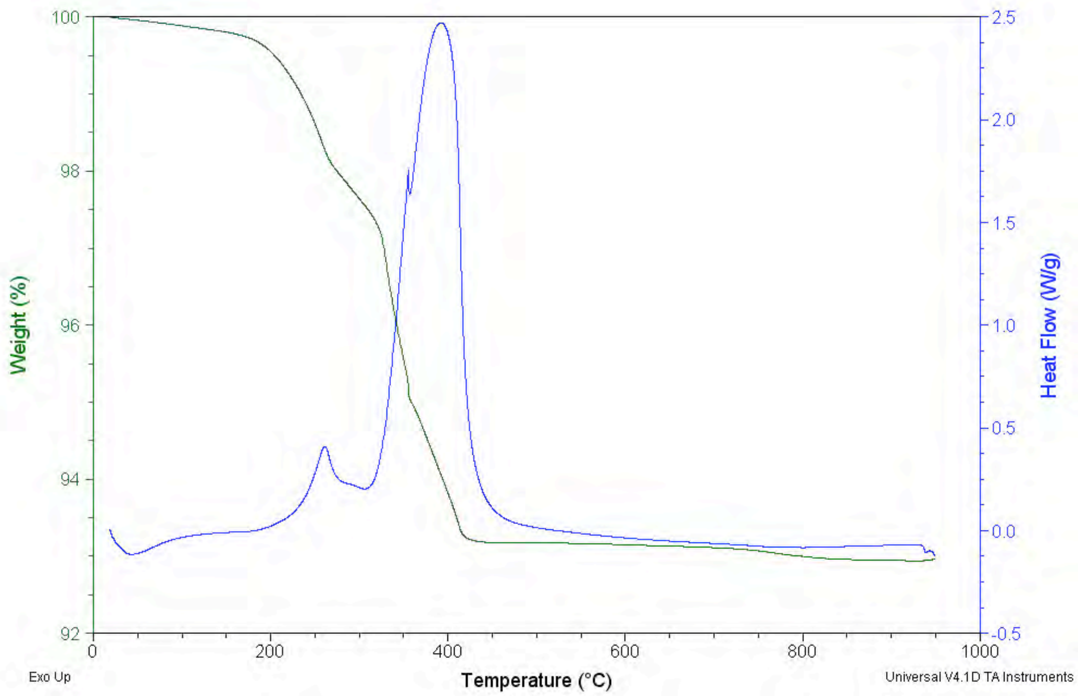

Figure 4.11: TGA and DSC curves for Ni:Mn 1:3.7 nickel manganite powder doped with borosilicate from acetylacetonate precursors

4.2.1.1.3.2 Acetate versus Acetylacetonate Solutions and Pyrolysis Procedures

To assess this importance of residual organics on phase development, the pyrolysis procedures were reversed; the 500°C 40 s pyrolysis was performed on the acetate films and the 100°C 1 minute and 300°C 3 minutes pyrolysis was performed on the acetylacetonate films. Figure 4.12 shows the XRD patterns for 1:4 films from an acetate precursor (after an anneal at 730°C) prepared using different pyrolysis procedures.

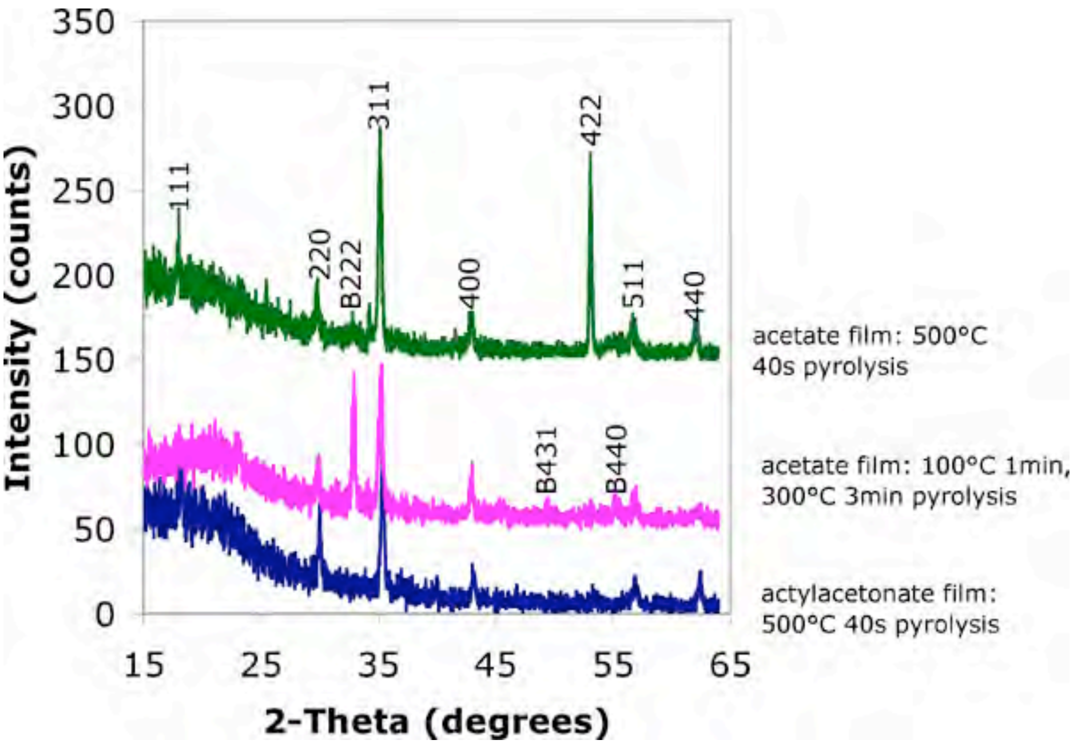

Figure 4.12: Grazing incident XRD patterns of Ni:Mn 1:4 acetylacetonate film annealed at 730°C and made with the 500°C 40s pyrolysis, 1:4 acetate film annealed at 730°C and made with 100°C 1 minute and 300°C 3 minutes pyrolysis, and the 1:4 acetate film annealed at 730°C made with the 500°C 40 second pyrolysis. Peaks with a "B" are from the bixbyite phase; the other indexed diffraction peaks correspond to a cubic spinel. Films are about 150 nm thick.

It can be seen in the figure that the film made using the acetate solution with the two-step, slower pyrolysis shows two distinct phases, the cubic spinel and the bixbyite phase (designated by "B" in the figure). When an acetate film was made using the 500°C 40 second pyrolysis, the bixbyite phase is reduced greatly, while the spinel phase remains. The fact that the amount of bixbyite is greatly reduced with the faster pyrolysis suggests that retained organics are, in fact responsible for the stabilization of the spinel phase.

The pyrolysis was also reversed with the acetylacetonate film. A 1:3.7 acetylacetonate film was crystallized at 700°C using the slower two-step pyrolysis, 100°C for 1 minute and 300°C for 3 minutes. As was described in section 4.2.1.1.3.1, it was found that the acetylacetonate organics are not fully removed until about 450°C. This means the two-step pyrolysis may not complete organic removal. Thus, on another sample, a 3 minute soak on a hot plate at 450°C was added after a 2 step pyrolysis. Figure 4.13 shows the resulting diffraction patterns of these films after a 730°C crystallization anneal.

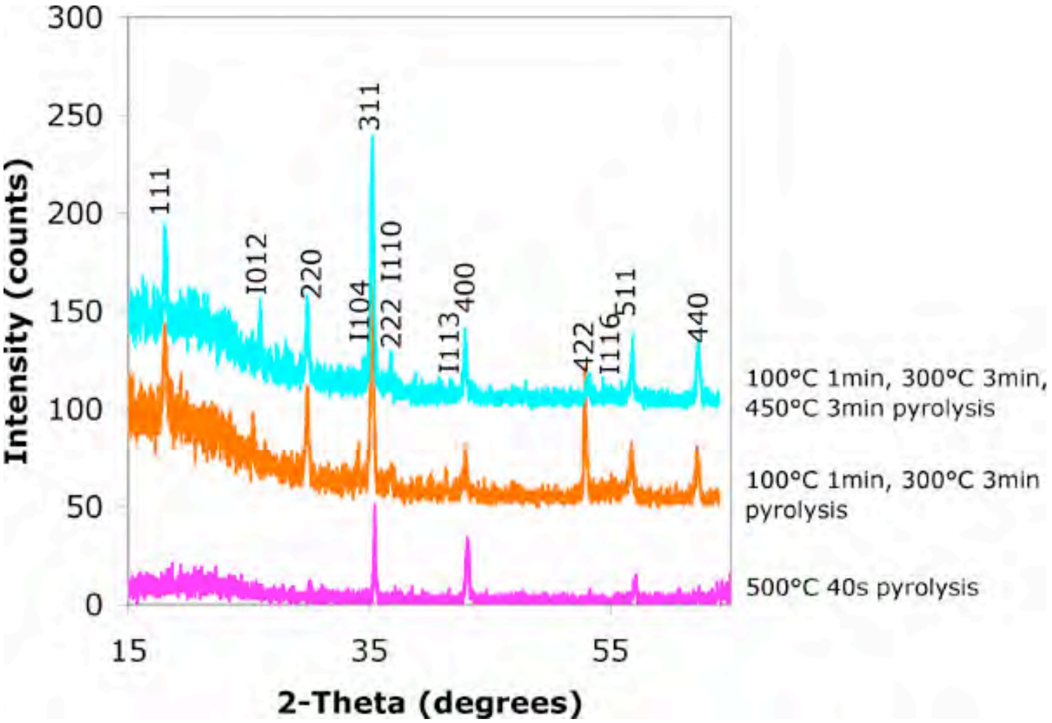

Figure 4.13: Grazing incident XRD patterns of Ni:Mn 1:3.7 films annealed at 730°C from acetylacetonate solutions using different pyrolysis steps. From the bottom to the top: film made using the 500°C 40s pyrolysis, film made using a 100°C 1 minute, 300°C 3 minutes pyrolysis, film made using a 100°C 1 minute, 300°C 3 minutes, 450°C 3 minutes pyrolysis. Peaks with a “I” are from the ilmenite phase; the other indexed diffraction peaks correspond to a cubic spinel. Films have thicknesses of about 150 nm.

It is clear that 1:3.7 films from acetylacetonate 730°C solutions show just diffraction peaks from the cubic spinel when a 500°C 40 s pyrolysis step is used. No signs of a second phase are apparent. The other two patterns are of films prepared using slower, multistep pyrolysis procedures. Both show second phase formation of ilmenite $NiMnO_3$.

It can be concluded that a slower pyrolysis, which should be more effective at removing the organics, yields second phase formation consistent with the phase diagram for samples prepared in air.

4.2.1.1.4 1:4 Ni:Mn Films from Acetate Precursors

The crystallinity of 1:4 Ni:Mn films from acetate precursors as a function of heat-treatment conditions is shown in Figure 4.14.

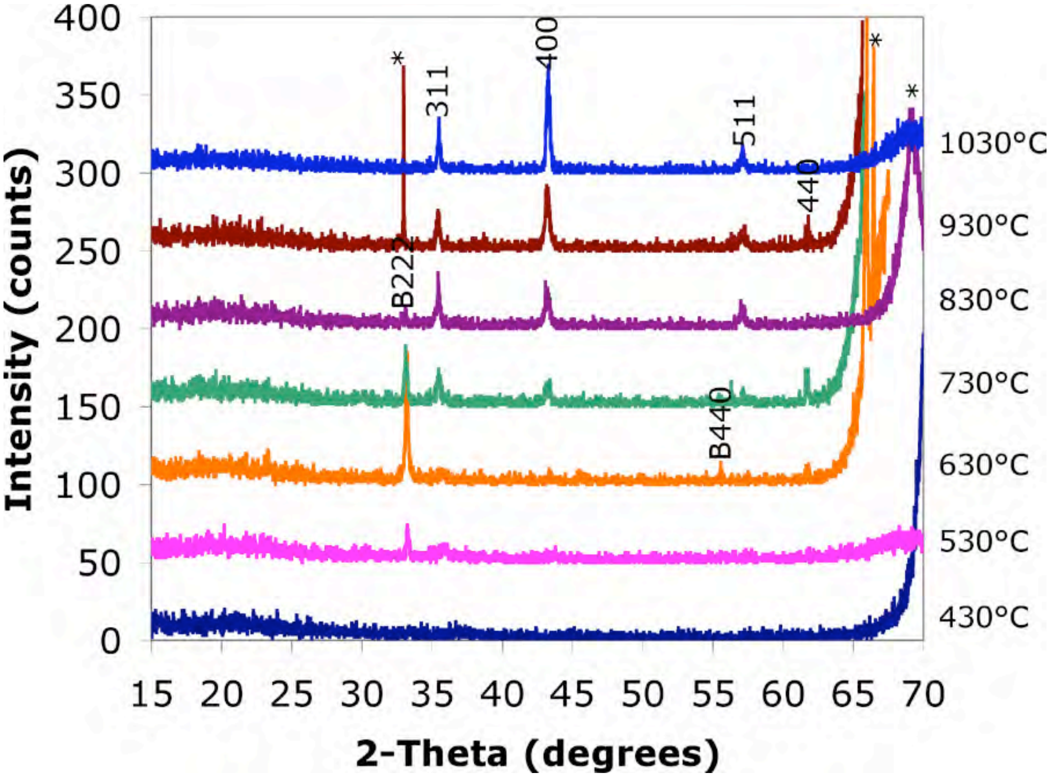

Figure 4.14: XRD patterns of films made from the Ni:Mn 1:4 acetate solution and crystallized at temperatures ranging from 430°C to 1030°C for one minute in the RTA. Indexed peaks correspond to the cubic spinel phase and those with an "*" are from the substrate. The indexed diffraction peaks correspond to a cubic spinel with a lattice parameter of 8.39 Å ± 0.03 Å. The thicknesses range from 150 nm for denser films annealed at higher temperatures to 230 nm for the low temperature annealed films.

Films heat-treated at 300°C are X-ray amorphous (not shown). The phase diagrams show a region of metastable cation deficient spinel phase below 400°C; between 400°C and 850°C bixbyite and ilmenite should coexist, and above 850°C single-phase spinel should form. It was found that films heat-treated between 530°C and 830°C showed the presence of a bixbyite as well as the spinel. The ilmenite phase was not identified in these films. By 930°C, the second phase disappears completely consistent with the equilibrium phase diagram.

4.2.1.1.4.1 High Temperature XRD

Since it is believed that the spinel phase crystallized due to local low partial pressures of oxygen within the film during the brief RTA step, to assess the phase formation under conditions closer to thermodynamic equilibrium in air, the 1:4 acetate solution was dried and ground into powder for high temperature XRD analysis. In-situ XRD was performed on the powder in ambient air using ramp rates of 10 °C per minute along with a 60 second hold before scanning. Step scans took approximately 2 hours to complete before the next temperature was approached. Figure 4.15 shows the XRD results obtained at each temperature.

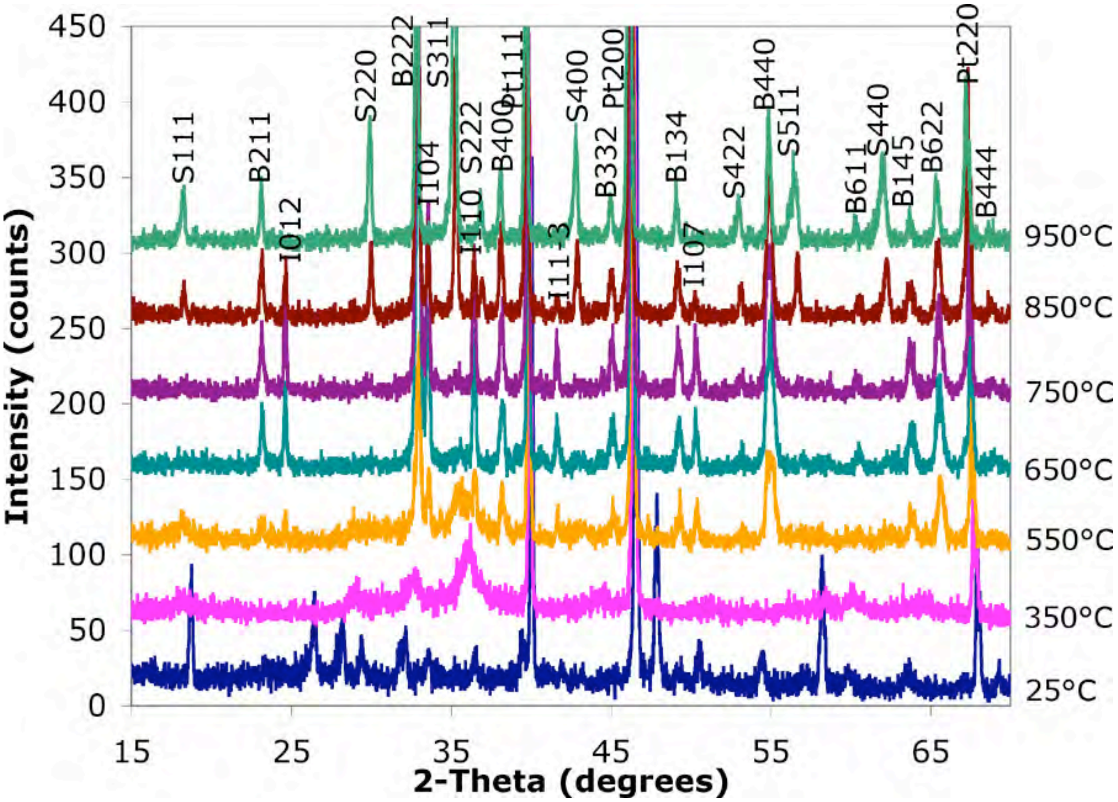

Figure 4.15: High temperature XRD runs for Ni:Mn 1:4 acetate solution between room temperature and 950°C. Indexed peaks refer to the spinel (S), bixbyite (B), and ilmenite (I) phases. The powder was placed on a platinum (Pt) holder.

At least two phases besides cubic spinel form over the course of the heat treatments, $NiMnO_3$ and Mn_2O_3. The organics observed at 25°C are removed by 350°C. A metastable cubic spinel exists along with bixbyite. At temperatures between 550°C and 650°C both bixbyite and ilmenite are present without noticeable traces of spinel, (i.e. the spinel decomposes into bixbyite and ilmenite). By 750°C the powder has begun to transform to the high temperature cubic spinel phase. The crystallization of spinel increases up to 950°C. Between 850°C and 950°C, ilmenite is converted, but some bixbyite remains. The final spinel phase observed at 950°C shows the cubic spinel phase.

4.2.1.1.4.2 Film Microstructure

The FESEM was used to study the microstructure of the films. Figures 4.16 and Figure 4.17 show the microstructure of a 1:4 acetate 8-layer film heat-treated at 930°C.

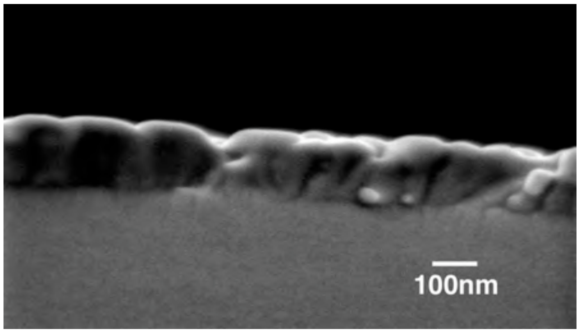

Figure 4.16: FESEM images of a Ni:Mn 1:4 acetate film heat-treated at 930°C

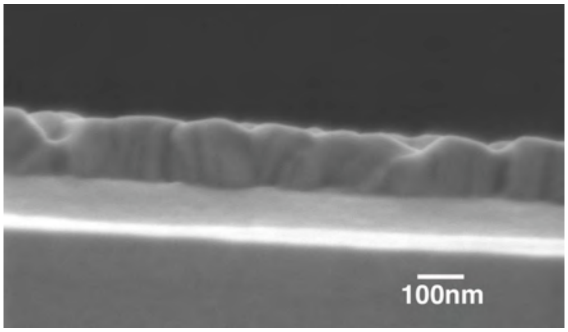

Figure 4.17: FESEM images of a Ni:Mn 1:4 acetate film heat-treated at 930°C

The morphology appears to be columnar in that the film is one grain thick. The average grain height is about 150 nm and the grain widths range from about 50 to 150 nm.

TEM was also used as a means of viewing the cross sections of the nickel manganite films. A 1:4 acetate film heat-treated at 930°C deposited on a silicon substrate is shown in Figure 4.18 a and b. The film thickness was about 150 nm. The film shows well-defined grain boundaries with no indication of a significant reaction with the underlying SiO_2.

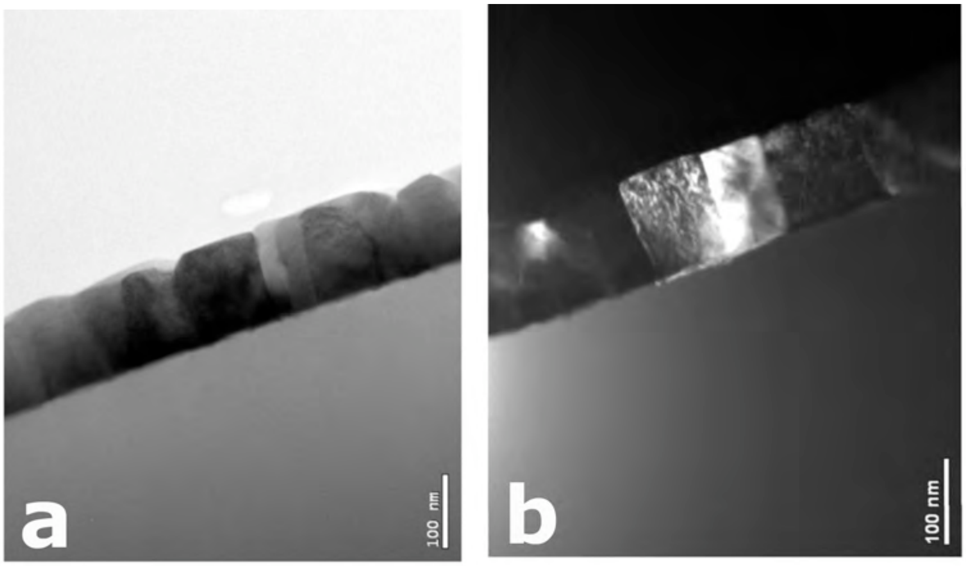

Figure 4.18: TEM images of a Ni:Mn 1:4 acetate film annealed at 930°C and is 8-layers thick (~150 nm) where a is a bright field micrograph and b is a dark field micrograph

4.2.1.1.4.3 Phase Homogeneity

TEM analysis was also performed on a Ni:Mn 1:4 film prepared from an acetate-based solution and annealed at 930°C. A TEM image of the cross section is shown in Figure 4.19a along with the EELS results in Figure 4.19b and c that were obtained using the Mn and Ni L2 and L3 edges.

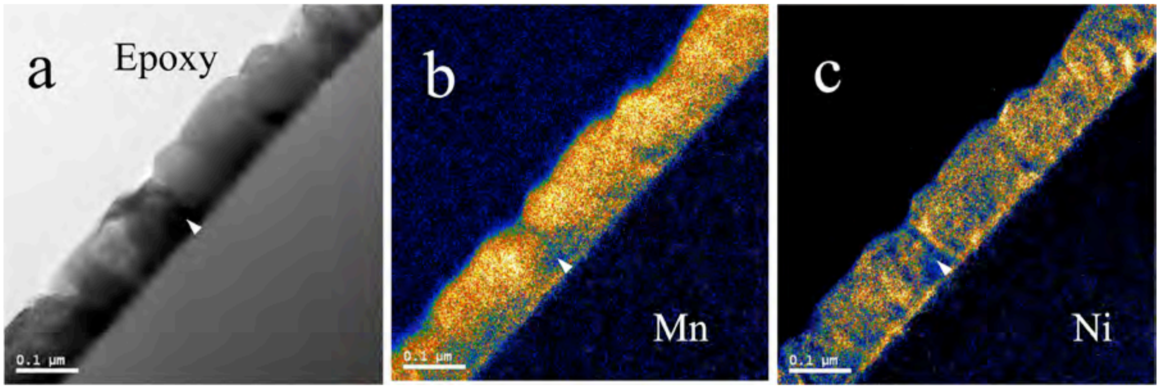

Figure 4.19: TEM image (a) and EELS elemental mapping of manganese (b) and nickel (c) in a Ni:Mn 1:4 film prepared from an acetate-based solution and annealed at 930°C. Arrows represent a region that is poor in both manganese and nickel due to the small thickness of the TEM sample in this region.

Again, the films were one grain in thickness after this heat-treatment. The grain size is approximately 150 nm. It was found that both the structure and the composition were uniform within the grains and throughout the film. The region marked by the arrow shows low concentrations of both elements, and is presumably caused either by a pore or by an area that was thinned excessively during the TEM sample preparation.

4.2.1.1.5 1:4 Ni:Mn Films from Acetylacetonate Precursors

The Ni:Mn 1:4 films were made using an acetylacetonate solution in order to better understand when and how the low temperature phases appear. Figure 4.20 shows films annealed between 530°C and 930°C.

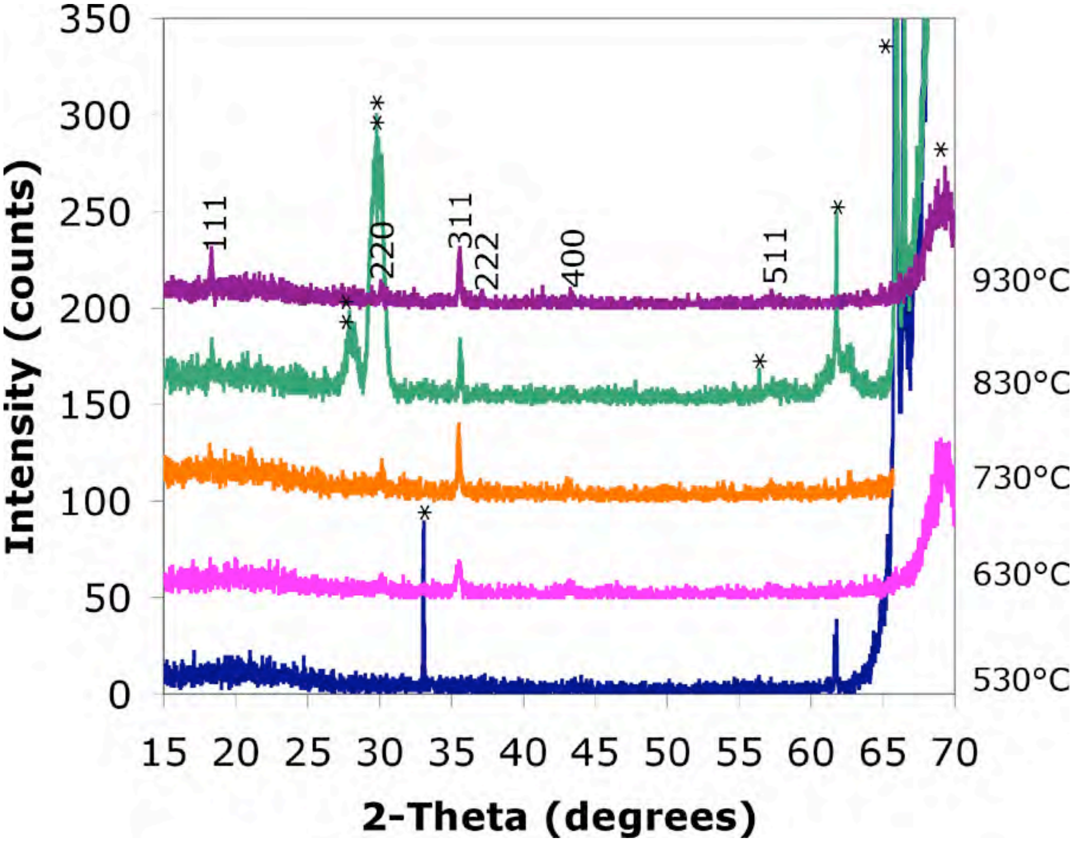

Figure 4.20: XRD patterns of films made from the Ni:Mn 1:4 acetylacetonate solution and crystallized at temperatures ranging from 530°C to 930°C for one minute in the RTA. Peaks marked with an "*" are from the substrate. The peaks marked with "**" are unknown. The indexed diffraction peaks correspond to a cubic spinel. Film thicknesses range from 150 nm for denser films annealed at higher temperatures to 230 nm for the low temperature annealed films.

Compared to the acetate-based films, these XRD patterns do not show any signs of second phases, ilmenite or bixbyite, at the lower temperatures. This is consistent with a larger content of retained organics producing a lower pO_2. This prevents the oxidation of manganese and inhibits the generation of a second phase. The more thorough pyrolysis used for the majority of the films from acetate precursors allows more time for organic removal. The higher local pO_2 during the crystallization step then yields the phases on the Wickham phase diagram.

4.2.1.1.6 1:1.65 Ni:Mn Films from Acetate Precursors

The 1:1.65 acetate-based films also show crystallization of the spinel phase at temperatures as low as 630°C for one minute RTA anneals. The spinel phase is observed for annealing temperatures up to 1030°C, as shown in Figure 4.21, similar to the 1:1 films.

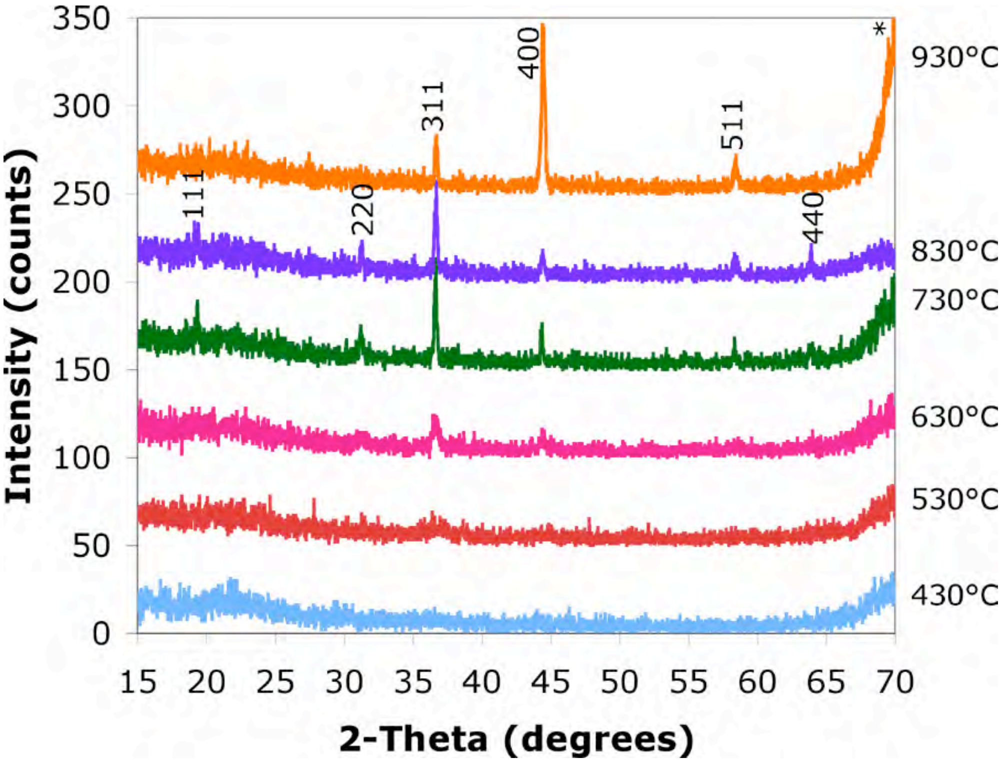

Figure 4.21: XRD patterns of films made from the Ni:Mn 1:1.65 acetate solution and heat-treated at temperatures ranging from 430°C to 930°C for one minute in the RTA. The indexed diffraction peaks correspond to a cubic spinel with a lattice parameter of 8.331 Å ± 0.003 Å. Film thicknesses range from 150 nm for denser films annealed at higher temperatures to 230 nm for the low temperature annealed films. Peaks with an "*" are from the substrate.

According to the phase diagram, at the 1:1.65 composition there should be mixed phases of ilmenite $NiMnO_3$ and bixbyite (Mn_2O_3) between 400°C and 705°C. At higher temperatures, a mixture of spinel and rocksalt (NiO) phases should be present, similar to the 1:1 films. For example, according to the lever rule, there should be 7.5% NiO and 93.5% spinel for the films heat-treated at 930°C. Only the spinel phase was observed using X-ray diffraction. It would be interesting to perform TEM analysis on a 1:1.65 film to see if the same small-scale heterogeneity develops within the spinel grains.

4.2.1.1.7 1:2 Ni:Mn Films from Acetate Precursors

Films with Ni:Mn ratios of 1:2 prepared from acetate-based solutions show a similar phase development sequence (between 430°C and 1030°C) to the 1:1 and 1:1.65 films. Figure 4.22 demonstrates the crystallization of the spinel phase without the detected presence of a second phase at temperatures below 705°C, most likely due to low local pO_2 as discussed previously. According to the phase diagram, a single-phase region of spinel occurs between about 730°C and 900°C for this composition.

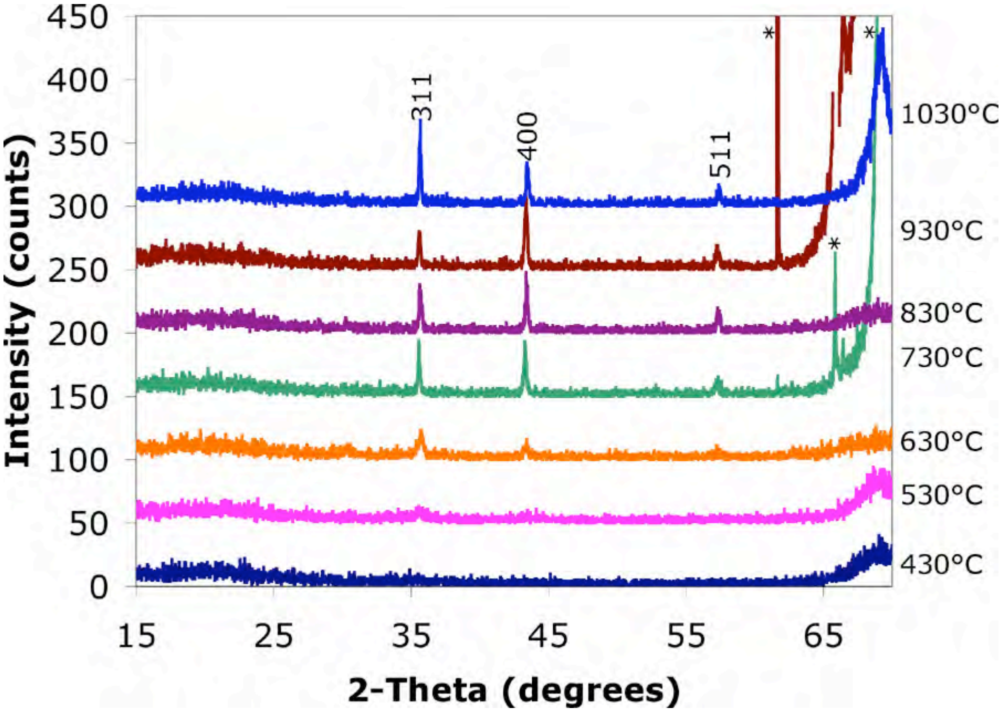

Figure 4.22: XRD patterns of films made from Ni:Mn 1:2 acetate solutions and heat-treated at temperatures ranging from 430°C to 1030°C for one minute in the RTA. Films are about ~150 nm thick. The indexed diffraction peaks correspond to a cubic spinel with a lattice parameter of 8.332 Å ± 0.005 Å. Peaks with an "*" are from the substrate.

4.2.1.1.7.1 Phase Homogeneity

The 1:2 acetate film annealed at 830°C was imaged using TEM for a more thorough analysis of composition homogeneity. EELS mapping of manganese and nickel was taken across a cross section of the film using the Mn and Ni L2 and L3 edges. Figure 4.23 shows a series of lower magnification images, a, b, and c, while d, e, and f are higher magnification images.

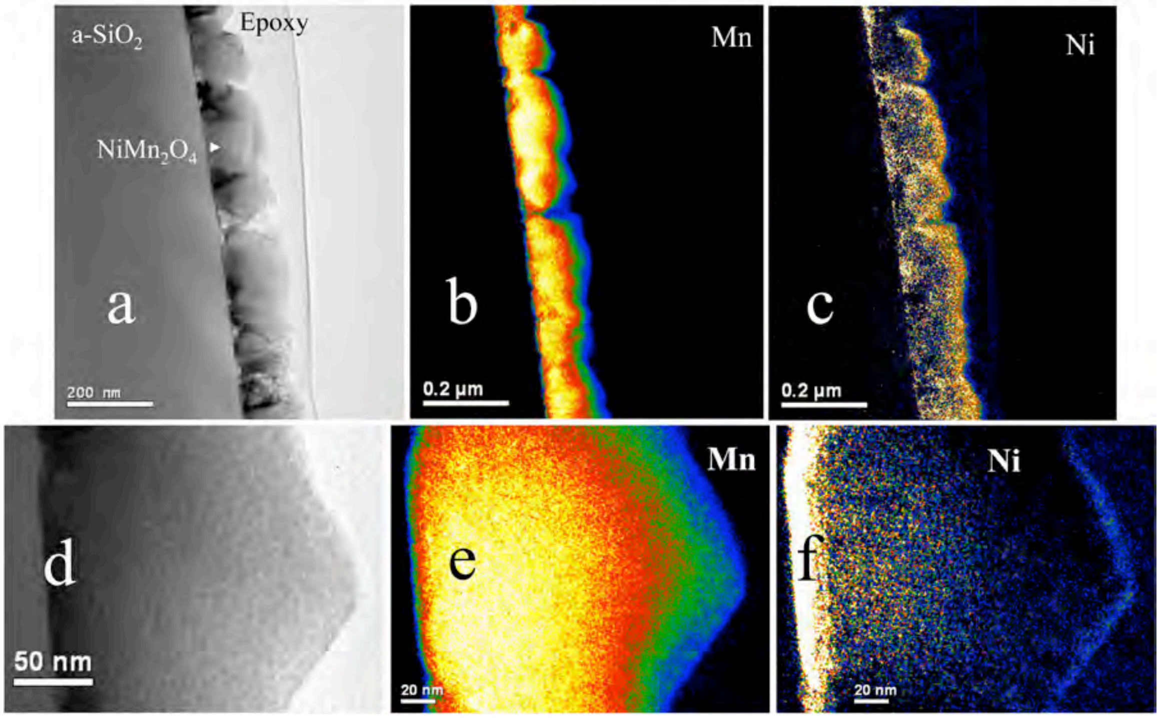

Figure 4.23: EELS elemental mapping of manganese and nickel within a Ni:Mn 1:2 acetate film heat-treated at 830°C

The maps portray a film that is essentially homogeneous in manganese and nickel content laterally, between grains. No decomposition is present in this film, as was seen in the 1:1 acetate film annealed at 930°C. EDS measurements across the thickness of the film confirmed the EELS results, as shown in Figure 4.24.

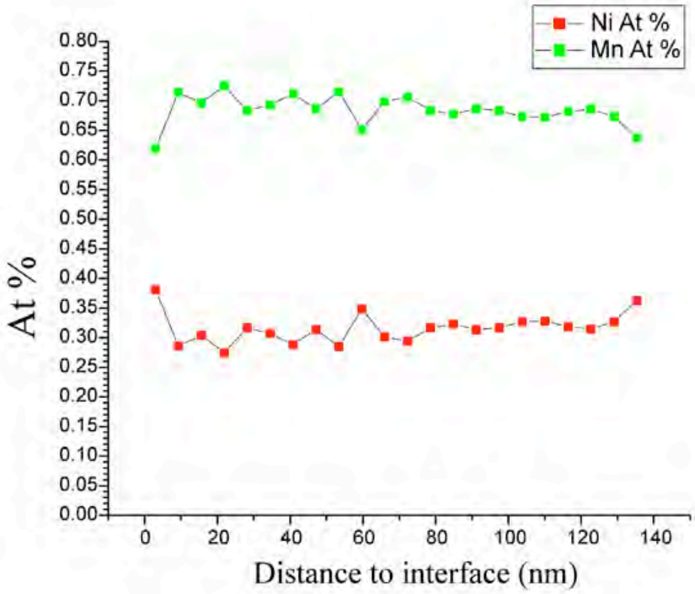

Figure 4.24: EDS analysis of the atomic percent of nickel and manganese across the thickness of a Ni:Mn 1:2 acetate film annealed at 830°C

There may be a very thin region near the films/substrate interface where the concentration of nickel (36 – 37.5 At%), is greater compared to the average (27.5 – 34.5 At%), while the manganese concentration at the interface (62-63.7 At%) is lower than the average (65.5 – 72.5 At%). Additional mapping on other samples should be undertaken to confirm this.

4.2.1.1.7.2 Film Microstructure

The microstructure was also characterized for a 1:2 acetate film annealed at 830°C. TEM images of the cross section are shown in Figure 4.25, where a is a bright field TEM micrograph and b is a dark field TEM micrograph. Many of the grains extend across the thickness of the film (~ 150 nm).

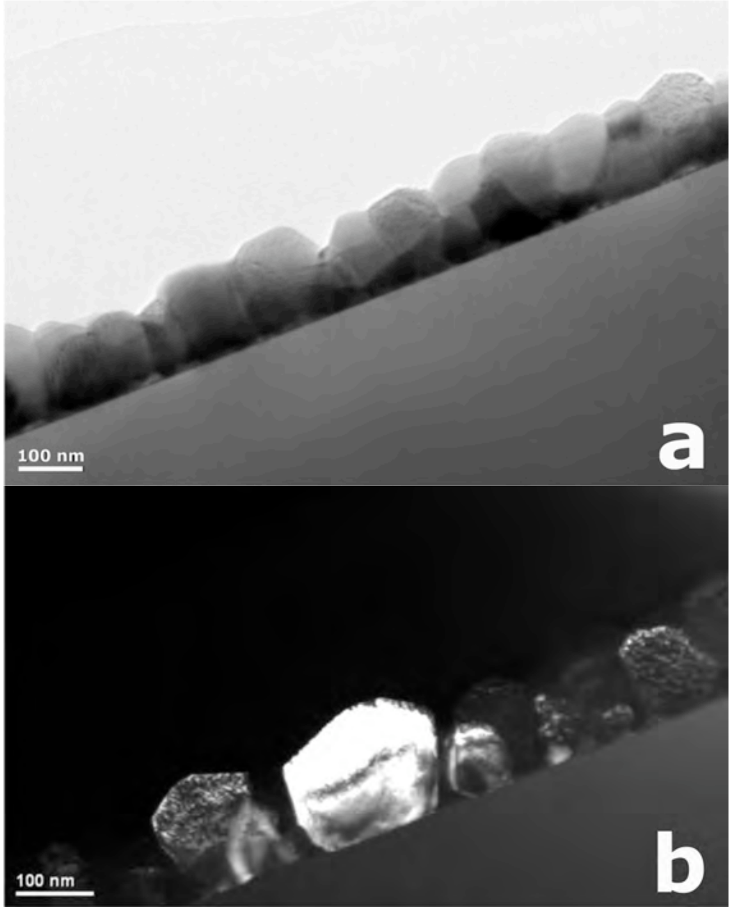

Figure 4.25: TEM images of a Ni:Mn 1:2 acetate films annealed at 830°C and is 8-layers thick where a is a bright field micrograph and b is a dark field micrograph

4.2.1.1.8 1:9 Ni:Mn Films from Acetate Precursors

The films made from the Ni:Mn 1:9 acetate solution are dominated by the bixbyite phase, Mn_2O_3, at all temperatures, consistent with the phase diagram. A peak that corresponds to the 33° 2θ angle of bixbyite has been observed as low as 530°C. Some spinel does form in films heat-treated at 930°C and 1030°C as seen in Figure 4.26 and in accordance with previous work [35].

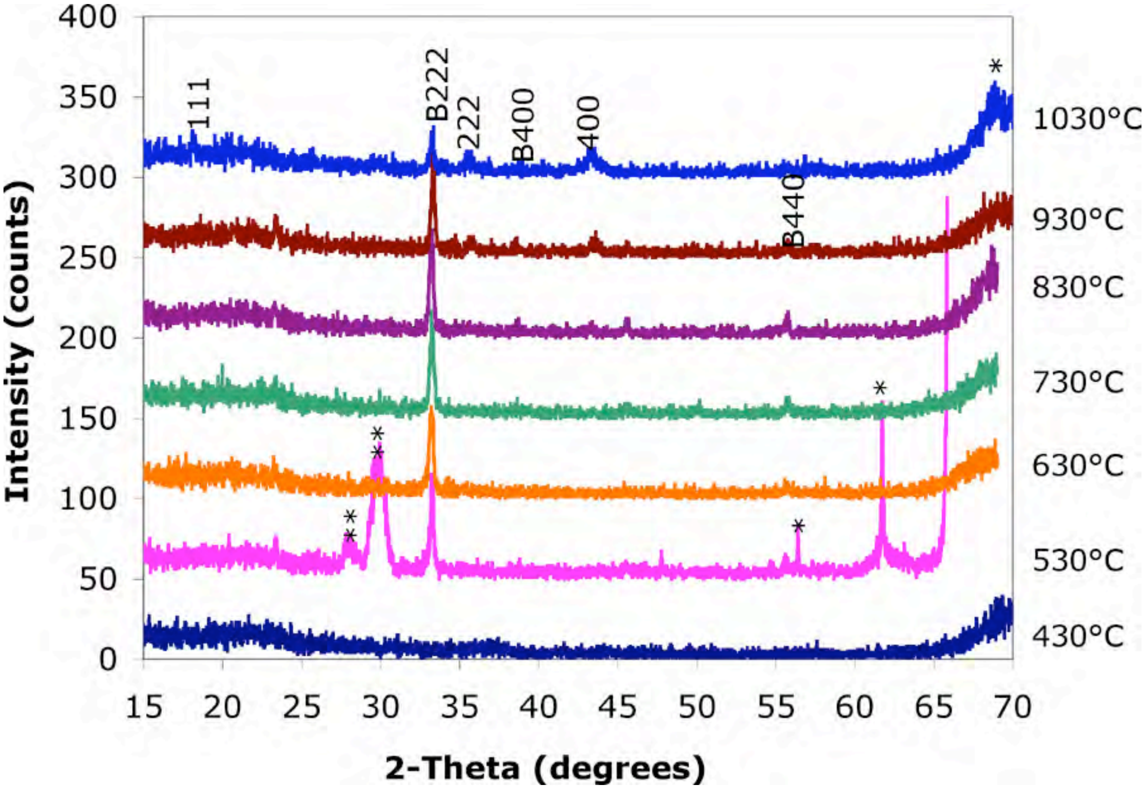

Figure 4.26: XRD patterns of films made from the Ni:Mn 1:9 acetate solution and crystallized at temperatures ranging from 430°C to 1030°C for one minute in the RTA. Indices with a "B" are from the bixbyite phase with a lattice parameter of 9.397 Å ± 0.004 Å, while peaks with an "*" are from the substrate and peaks with "**" are unknown. The other indexed diffraction peaks correspond to a cubic spinel with a lattice parameter of 8.42 Å ± 0.04 Å.

4.2.1.1.9 6:1 Ni:Mn Films from Acetate Precursors

On the Wickham phase diagram, Ni_6MnO_8 is a line compound between 400°C and 760°C. Above 760°C Ni_6MnO_8 should decompose into a rocksalt phase and a spinel phase. Below 400°C a metastable cation deficient cubic and a rocksalt phase can be present. Figure 4.27 shows the experimental results on phase formation in 6:1 films as a function of the heat-treatment temperature over the range from 430°C to 1030°C.

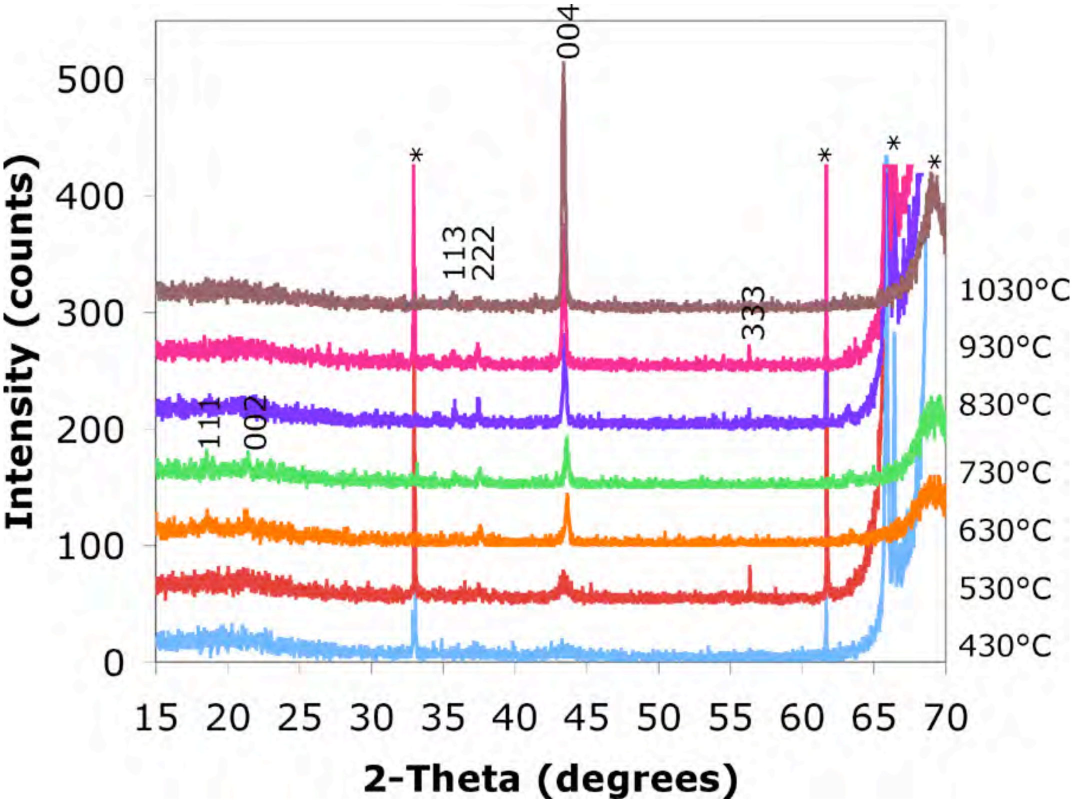

Figure 4.27: XRD patterns of films made from the Ni:Mn 6:1 acetate solution and crystallized at temperatures ranging from 430°C to 1030°C for one minute in the RTA. Peaks with a "*" are from the substrate. The other indexed diffraction peaks correspond to a cubic Ni_6MnO_8 with a lattice parameter of 8.33 Å ± 0.02 Å.

Crystallinity was shown to increase as a function of annealing temperature. For 6:1 films, above 830°C, NiO and spinel phases are supposed to form according to the phase diagram, but XRD only shows the presence of Ni_6MnO_8. It is possible that NiO and/or spinel are present in these films, but have crystallites that are too small to be detected by XRD. TEM of the 1:1 film showed the presence of the NiO phase when XRD did not and therefore it would be interesting to study the high temperature annealed 6:1 films using TEM.

In conclusion, it has been found that spinel is readily crystallized during rapid annealing of chemical solutions for compositions between 50% and 80% Mn/(Ni+Mn).

It is believed that the enhanced stability of spinel at lower temperatures is associated with low oxygen partial pressures.

4.2.1.2 Low pO_2 Annealing

Because microbolometer arrays are often made directly on top of underlying CMOS circuitry, it is important for the processing temperatures to be as low as possible. In the back-end-of-the-line fabrication of the microbolometer, the highest temperature the wafer should be exposed to is about 450°C. Thus, if a new material system is used to fabricate microbolometers, it would be most interesting if the NTC film could be prepared at temperatures below this. To increase the likelihood of forming the spinel phase at these low temperatures [36], films were also processed in a tube furnace for annealing in more reducing atmospheres. For these studies, the films were heat-treated in the tube furnace after a pyrolysis step. As a starting point, the annealing time was set at five hours and various atmospheres were tested, including ambient air, flowing oxygen, and flowing argon. The following results are organized by composition (as shown in Figure 4.1).

4.2.1.2.1 Films Annealed in Argon at 400°C

A set of pyrolyzed films was annealed in a tube furnace in flowing argon gas with 2-6 ppm of oxygen. A Ni:Mn 1:1 acetate film, a 1:1.65 acetate film, a 1:3.7 acetylacetonate film, a 1:3.7 acetate film, and a 1:4 acetate film were all annealed for 5 hours in argon. The majority of the films showed little crystallinity, but the onset of spinel crystallization is apparent in the 1:4 film, as seen in Figure 4.28.

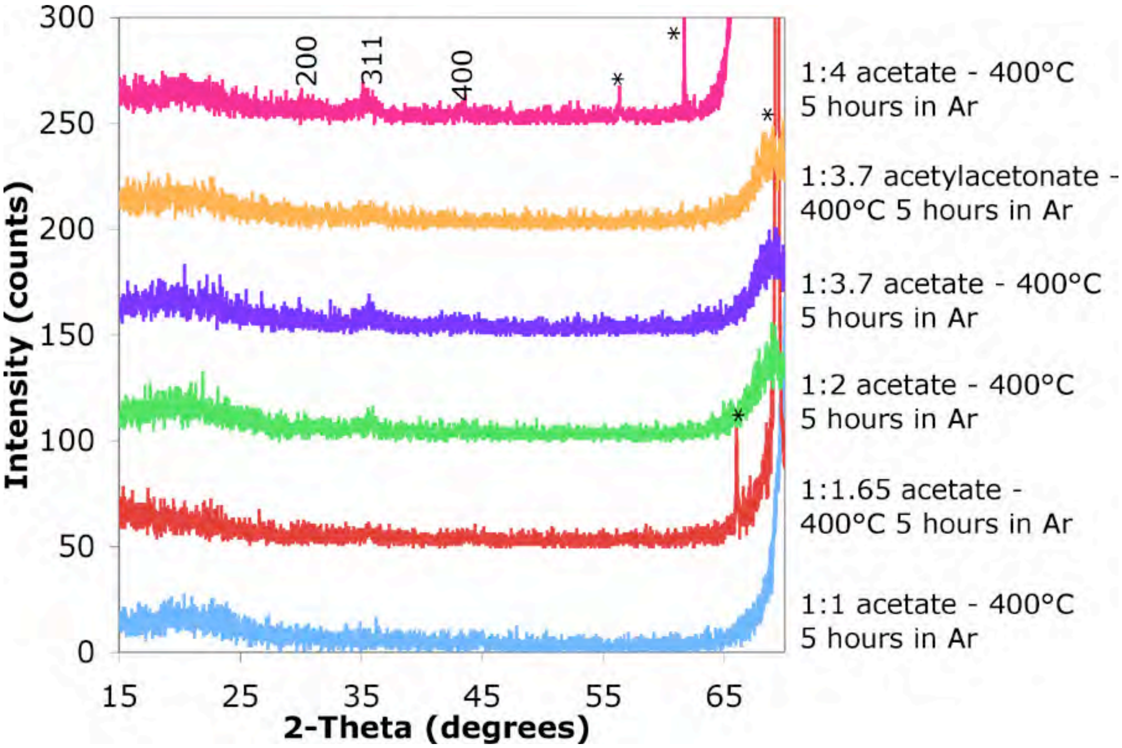

Figure 4.28: XRD patterns of films annealed for 5 hours at 400°C in argon. Indexed peaks refer to the spinel crystal structure. Films are approximately 230 nm thick. Peaks with an "*" are from the substrate.

The peaks for 1:4 films are very broad and weak, suggesting either incomplete crystallization or a very small crystallite size. It would be very interesting to analyze this film with TEM to determine the grain morphology, assess the possibility of an amorphous phase, and also to determine if compositional gradients exist. The compositions containing less manganese show even weaker and broader spinel peaks.

4.2.1.2.2 Films Annealed in an Oxygen Rich Atmosphere

For comparison to the films annealed in argon, films were also annealed in a tube furnace with flowing oxygen for 5 hours. As described by Wickham, the bixbyite and ilmenite phases should develop [35]. Films with Ni:Mn ratios of 1:2 (from the acetate route) were used for this study because they fall within the region of the phase diagram where both phases are present. The film annealed at 300°C and 400°C did not show any signs of crystallization as illustrated by Figure 4.29. The film annealed at 500°C shows precisely what the phase diagram maps, both bixbyite and ilmenite phases.

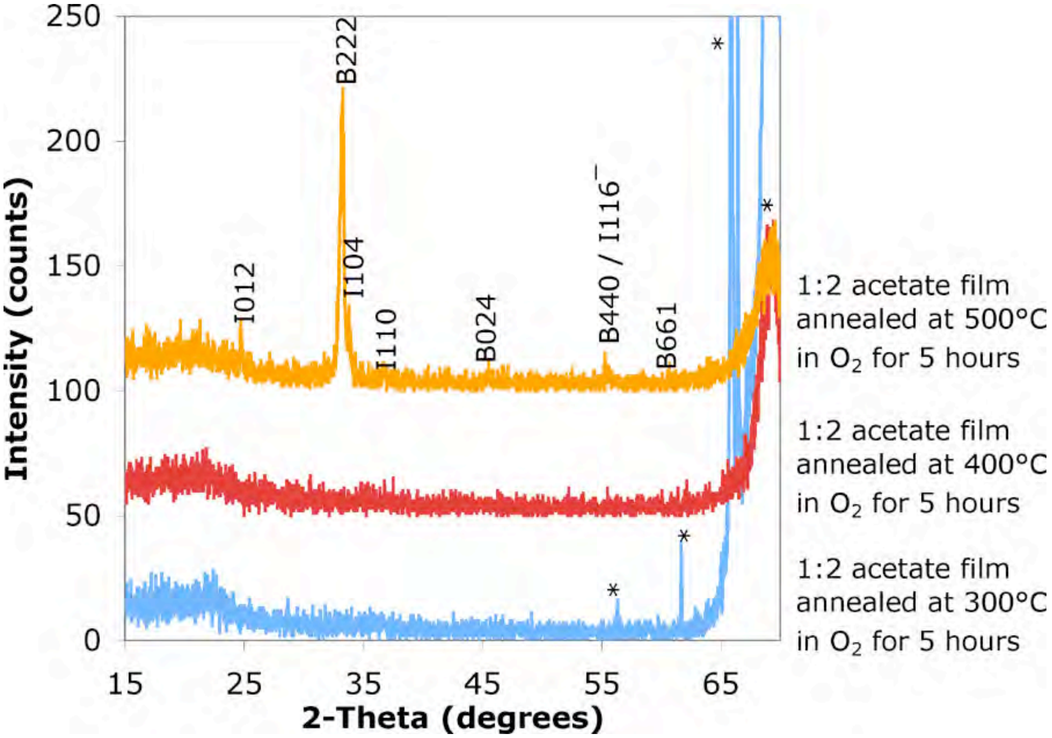

Figure 4.29: XRD patterns of Ni:Mn 1:2 acetate films annealed in oxygen for 5 hours at 300°C, 400°C, and 500°C. The two phases indexed are ilmenite (I) and bixbyite (B). Peaks with an "*" are from the substrate.

4.2.1.3 Lattice Parameters

The lattice parameters reported in this thesis were determined using the high temperature annealed films that showed the best crystallinity. The 311, 400, and 511 peaks of spinel were used for this measurement. A silicon powder standard (NIST 640C Si reference) was run along with the films for calibration purposes (a theta calibration with a parabolic fit using Jade 8 was performed to align the film patterns to the silicon standard). Selected peaks were fit using a pseudo-Voigt algorithm. Jade was also used to determine the lattice parameters from the peaks. Lattice parameters for films with Ni:Mn ratios of 6:1 to 1:9 (Mn contents between 0.14 and 0.9) annealed at 1030°C in air for one minute are plotted in Figure 4.30.

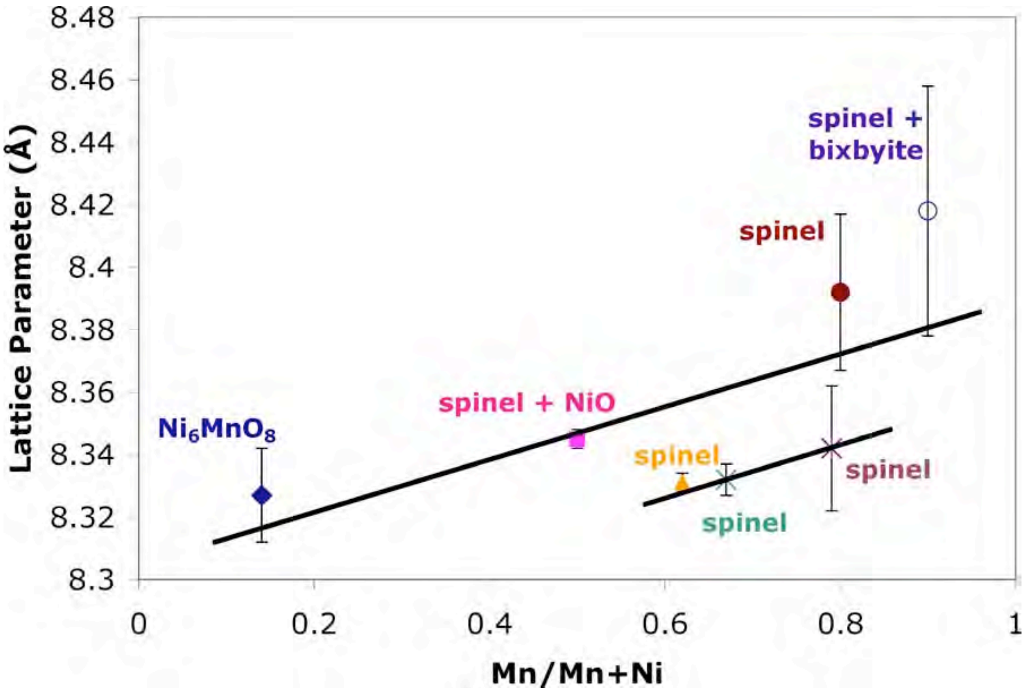

Figure 4.30: Lattice parameters reported with range bars representing the variations resulting from different peak profile fitting for films annealed at 1030°C in air for one minute. The lines are guides to the eye only.

Due to the poor crystallinity of the films, the few peaks present for analysis, and the current equipment, the consistency of profile fitting is low. The range bars shown for each data point in the plot represent the differences in the values of the calculated lattice parameters when the available peaks were fit at least four different times using the Jade 8 software. Thus, in some cases, the errors for the weak, broad peaks observed in the films is quite large. A higher resolution powder diffractometer should be used for analysis in the future.

An increase in lattice parameter is expected as the amount of manganese increases. This is due to the fact that for high spin Ni^{2+} and Mn^{3+} cations [36], the ionic radii is slightly larger for manganese. High spin Mn^{3+} in 6 coordination has a radius of 0.64 Å, Mn^{2+} in 4 coordination has a radius of 0.66 Å, while high spin Ni^{3+} in 6 coordination has a radius of 0.60 Å, and Ni^{2+} in 4 coordination has a radius of 0.55 Å. Sarrion et al. reports this trend as being linear between a manganese content of 0.50 and 0.81 [88]. The lattice parameters reported for samples sintered at 1433 K are higher than those seen here for films, ranging from 8.4 Å to 8.45 Å [88]. In contrast, Kukuruznyak et al. reports lattice parameters for $Ni_{0.48}Co_{0.24}Cu_{0.6}Mn_{1.68}O_4$ thin films annealed between 600°C and 800°C ranging from 8.322 Å to 8.363 Å [65]. The lattice parameters were reported to increase with an increase in anneal temperature. These values correspond more closely with the majority of the thin films processed in this thesis.

Vegard's law is not demonstrated with this set of seven films. This is most likely due to the fact that not all the films are single-phase spinel. The films at Mn/Mn+Ni = 0.9 exhibits both bixbyite and spinel phases and the 0.5 film showed both spinel and NiO phases. Thus, the Ni:Mn ratios within the spinel phase do not correspond to the global composition of the film. It would be useful to use a quantitative local composition analysis technique to allow Figure 4.30 to be re-plotted using the observed spinel composition on the x-axis.

Lattice parameter can be used to estimate site occupancy in the spinel structure. A few assumptions must first be made. Tang et al. reports the high temperature spinel that forms above 750°C has a cation distribution as follows, where ν is the inversion parameter [36].

$$Ni^{2+}_{1-\nu}Mn^{2+}_{\nu}[Ni^{2+}_{\nu}Mn^{3+}_{2-2\nu}Mn^{4+}_{\nu}]O_4$$

If this distribution of cations is assumed where Ni^{2+} and Mn^{2+} sit on tetrahedral sites and the bracketed cations sit on octahedral sites, the inversion parameter can be calculated using the experimental lattice constant, a, in Equation 4.1 [38].

$$a = 2.0995*d_A + (5.8182*d_B^2 - 1.4107d_A^2)^{1/2} \qquad \text{Equation 4.1}$$

The cation-oxygen distances in terms of inversion parameter are represented by d_A for the tetrahedrally coordinated cations, and d_B for the octahedrally coordinated cations. When calculated using the experimental results (Figure 4.30) the degree of inversion is greater than one, which is impossible. That is, the lattice parameters of both the films reported here and those prepared by Kukuruznyak et al. are too small to be accounted for by the inversion parameter. It has been shown with the presence of cation vacancies on the octahedral site, the lattice parameter decreases [38]. The octahedral vacancies are created to achieve electroneutrality when a Mn^{3+} cation occupies the tetrahedral site [38]. Thus, it is believed that the majority of the thin films processed in this thesis contain cation vacancies which cause smaller lattice constants. It is also possible that the spinel films are fully inverse.

4.3 Electrical Characterization

Microbolometer sensitivity is a function of the signal-to-noise ratio. In this section, the electrical characteristics of the films were investigated in order to assess both the electrical resistance and the TCR as a function of composition, phase assemblage, and processing temperature.

4.3.1 Ohmic Behavior of Electrodes

Prior to making electrical measurements, it was essential to demonstrate that ohmic contacts could be achieved (so that the measured TCR would correspond to the film, rather than the film/electrode interface). For this purpose, the current – voltage (I-V) behavior of Ni:Mn 1:4 acetate film with Au electrodes was investigated. Figure 4.31 shows a series of I-V data from room temperature to 100°C.

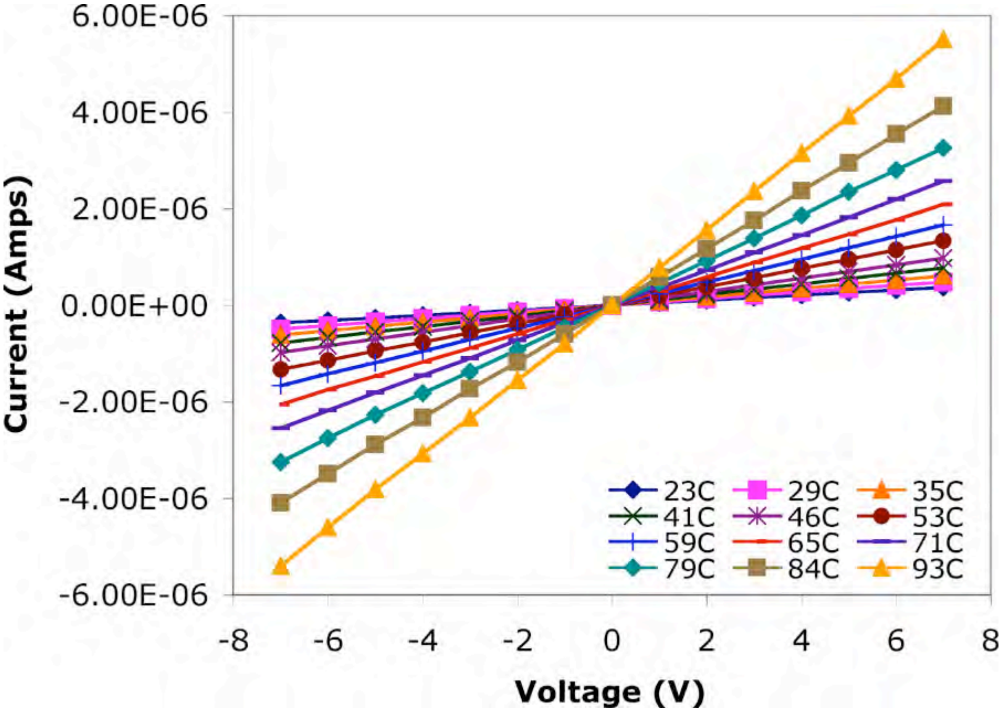

Figure 4.31: I-V curves as a function of temperature of a Ni:Mn 1:4 nickel manganite spinel film from an acetate solution, heat-treated at 930°C. Ohmic behavior was observed using gold electrodes.

I-V curve measurements were made between two strip electrodes with a gap of 200 μm. It is clear that the data are linear over a wide range of temperatures. Thus, the sputtered gold strip electrodes used for the electrical measurements of the films were found to have ohmic behavior using a two-probe setup.

For small polaron hopping, there is a finite time between the time the charge carrier hops between sites (jump time) and when the lattice distorts to accommodate the new location of the carrier due to the change in valence [89, 90, 91]. When the time between jumps is short compared to the time required for the lattice relaxation, the most likely jump direction for a displaced charge carrier is back to the previously occupied position, and the hopping is considered to be correlated [89, 90]. This process determines an upper limit of the drift velocity. If the carrier velocity approaches the lattice distortion velocity, the carrier mobility will be affected [89, 90]. It is believed that correlation between successive hops cannot be ignored for drift mobilities greater than about 0.1 $cm^2/V\ s$ [89]. In such a case, materials with a higher mobility will not display clear activation-type temperature dependence. [89]. When the material exhibits Ohmic behavior, no changes are occurring in carrier mobility [$cm^2/V\ s$] or in resistance as current and voltage increase. In effect, as current is increased (voltage increases), the drift velocity will increase if it is assumed there is no change in carrier density. As the electrical potential approaches the region where the jump times influence the drift mobility, the material should deviate from an Ohmic response. Over the potential range used in this thesis, -7 V to 7 V, all of the films exhibit Ohmic behavior. Thus, for this range the resistance does not change and the carrier mobility is constant. Also the materials studied exhibited a clear activation energy, as will be shown below in the collected data. A simple order-of-magnitude calculation using Equation 4.2 [4], suggests that the carrier mobilities in the nickel manganite films are many orders of magnitude below 0.1 cm^2/Vs, which is low enough for the materials to display clear activation-type temperature dependence.

$$\mu = [ed^2\nu \exp(q/k\mathrm{T})] / \mathrm{kT} \qquad \text{Equation 4.2}$$

Equation 4.2 relates the thermally activated mobility, μ, to the electronic charge of an electron, e, the distance between nearest neighbor octahedral cations, d, a frequency factor, ν, Boltzmann's constant, k, and the activation energy of the hopping mechanism, q. The frequency factor was estimated to be near phonon frequencies of 10^{13} Hz, the distance between octahedral sites in the spinel lattice is close to 2.86 Å, and the activation energy was estimated as 0.35 eV, which is a typical value found in the nickel manganite thin films synthesized in this thesis. The calculation was done at an absolute temperature, T, of 298K. The estimated mobility comes out to be on the order of 10^{-13} cm^2/V s, which is much less than 0.1 cm^2/V s. The mobility of the charge carriers was calculated a second way for comparison using Equation 4.3 [4]

$$1/\rho = ne\mu \qquad \text{Equation 4.3}$$

where the resistivity, ρ, of the material is related to the number of charge carriers per cm^3, n, the charge of an electron, e, and the carrier mobility, μ. The carrier concentration was estimated assuming that for the 32 octahedral sites in the spinel lattice, 16 are occupied with manganese cations [4]. A lattice parameter of 8.38 Å was used to calculate the volume of the cubic unit cell. The resistivity was estimated as 1000 Ωcm, as will be shown to be the magnitude for most nickel manganite thin films. The mobility was estimated to be on the order of 10^{-14} cm^2/V s, which is very similar to the estimation from the first equation. Thus, it appears to be reasonable to treat all of the nickel manganite films in this thesis as corresponding to simple uncorrelated electron hopping conductors.

To ensure the electrical measurements probed the thin film and not the substrate, TCR measurements were taken using different spacing for the top electrodes. All TCR values in this thesis were obtained by resistance measurements taken between room temperature and 100°C. Figure 4.32 shows the average TCR values obtained when testing between the initial strip (marked by the arrow in Figure 4.33) and each of the electrodes 1 through 5 as labeled.

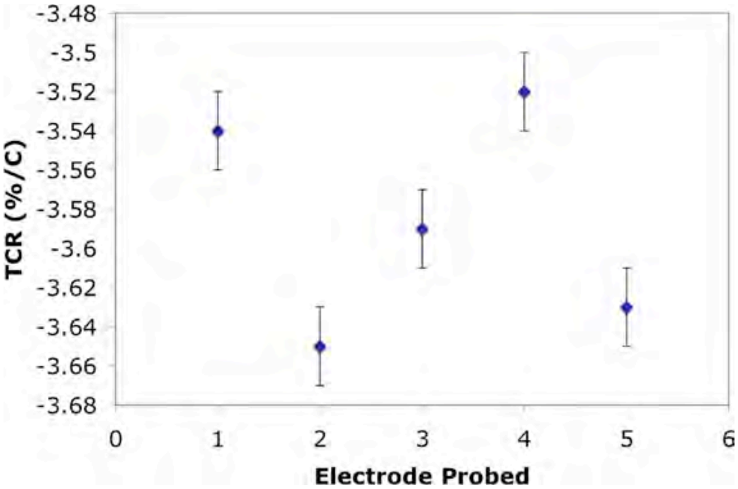

Figure 4.32: TCR values measured between each strip electrode with respect to the first

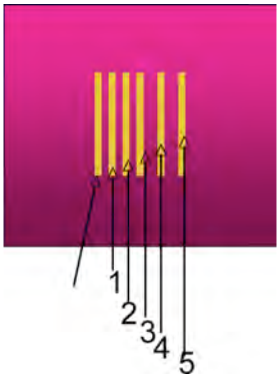

Figure 4.33: Image representing the electrodes used to take each of the five TCR measurements shown in Figure 4.32

The spacings between each set of electrodes used for the measurements are as follows, 200 μm, 600 μm, 1000 μm, 1600 μm, and 2200 μm. Error bars on the data were obtained from the slope of the lnR versus T curves used to obtain the TCR values as shown below.

The TCR values do not vary significantly. The average value was -3.56 %/K, with a standard deviation of ± 0.08 %/K. Therefore, it can be concluded that for all the I-V measurements the film is sampled and not the substrate. In addition, the scatter in the data suggests that the TCR values can be reliably measured within about 0.1 %/K.

4.3.2 TCR Measurements

A natural log (lnR) versus temperature (T) plot for a cubic nickel manganite spinel sample made from 1:4 acetate solution at 930°C is shown in Figure 4.34.

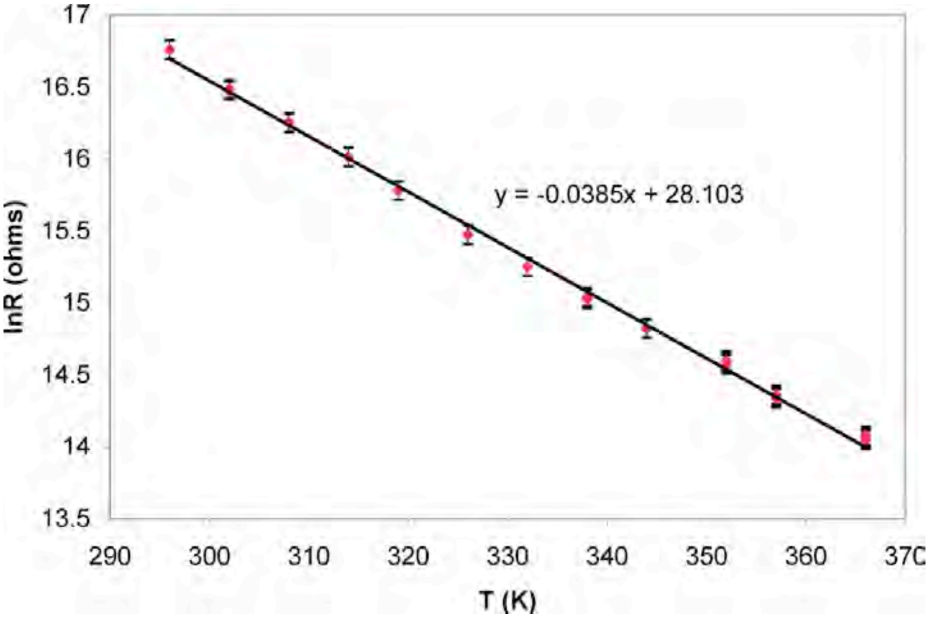

Figure 4.34: Plot of lnR versus T for a Ni:Mn 1:4 acetate film crystallized at 930°C to produce cubic spinel; the slope gives an average TCR value of -3.85 %/K with a 90 % confidence limit of 0.016 %/K.

The TCR value is obtained from the slope of this curve and it was found to be -3.85 %/K. This is an average TCR value determined over a range of temperature between 295 K and 365 K. Obtaining the TCR from this graph can be justified by taking the natural log of Equation 4.4, giving the activation energy, E_a, in terms of resistance, R.

$$R = R_o \exp(E_a/kT) \qquad \text{Equation 4.4}$$

After taking the natural log of both sides, Equation 4.5 is the resultant.

$$\ln R = \ln R_o + E_a/kT \qquad \text{Equation 4.5}$$

If the last term is multiplied by T/T and E_a/kT is assumed to be constant, Equation 4.6 shows the resultant.

$$\ln R = \ln R_o + T^*E_a/kT^2 \qquad \text{Equation 4.6}$$

If it is assumed that $TCR = -E_a/kT^2$ is nearly constant, then a plot of lnR vs. T enables a determination of the TCR. The activation energy can be determined from an Arrhenius plot of the lnR versus 1/T as illustrated in Figure 4.35.

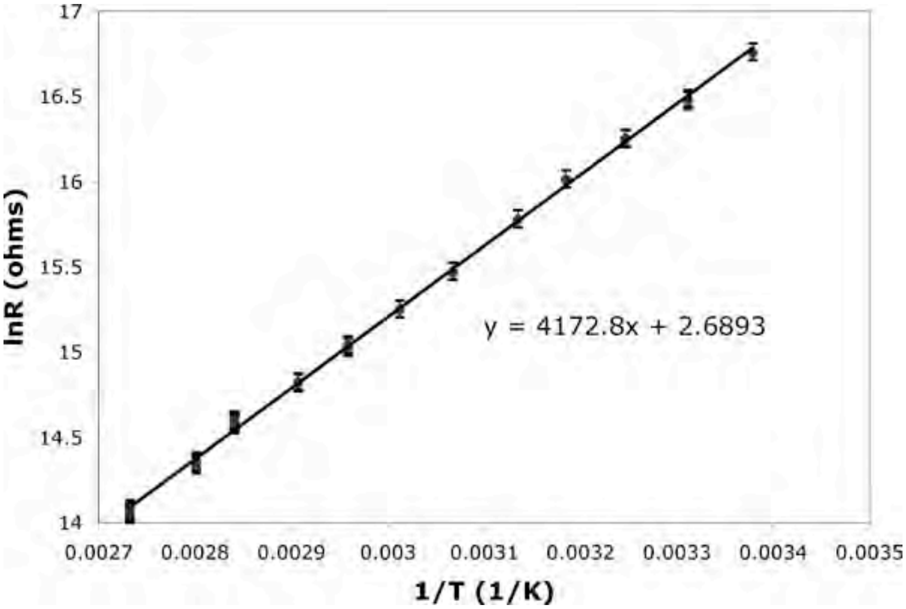

Figure 4.35: Arrhenius plot of lnR versus 1/T for a Ni:Mn 1:4 acetate film crystallized at 930°C to produce cubic spinel where the slope represents $B=E_a/k$. For this 150 nm film, $E_a = 0.36$ eV.

The positive slope of the Arrhenius plot provides the temperature constant, B. For this film the activation energy was found to be 0.36 eV (B = 4173 K). Using $E_a = 0.36$ eV to calculate TCR at 298 K yields -4.70 %/K as the value. This is much larger than the TCR determined by the lnR versus T slope. This is because when the TCR is found from the slope of lnR versus T, an average TCR over the temperature range is obtained.

The activation energies of the thin films in this thesis are close, but lower than those of the bulk thermistor samples, especially around x = 0.6 (Table 4.2).

Table 4.2: E_a values for bulk thermistors compared to films made in this thesis. The films were annealed at either 930°C or 430°C, except *=1030°C and **=530°C

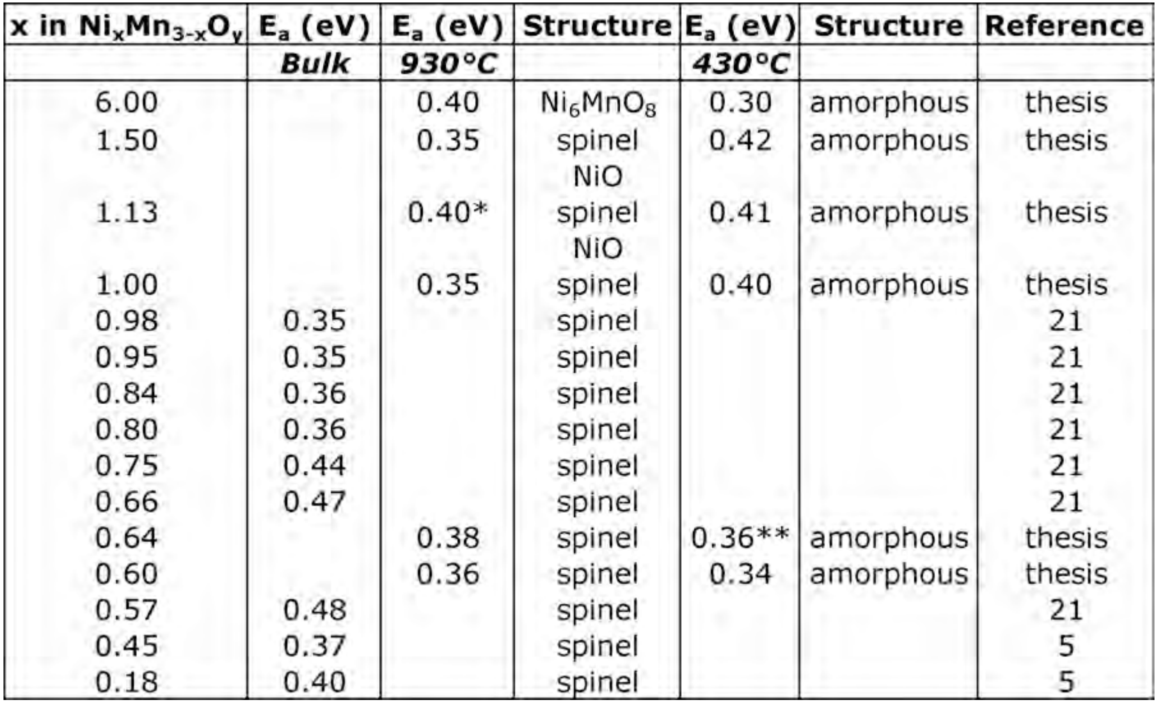

x in $Ni_xMn_{3-x}O_y$	E_a (eV)	E_a (eV)	Structure	E_a (eV)	Structure	Reference
	Bulk	***930°C***		***430°C***		
6.00		0.40	Ni_6MnO_8	0.30	amorphous	thesis
1.50		0.35	spinel NiO	0.42	amorphous	thesis
1.13		0.40*	spinel NiO	0.41	amorphous	thesis
1.00		0.35	spinel	0.40	amorphous	thesis
0.98	0.35		spinel			21
0.95	0.35		spinel			21
0.84	0.36		spinel			21
0.80	0.36		spinel			21
0.75	0.44		spinel			21
0.66	0.47		spinel			21
0.64		0.38	spinel	0.36**	amorphous	thesis
0.60		0.36	spinel	0.34	amorphous	thesis
0.57	0.48		spinel			21
0.45	0.37		spinel			5
0.18	0.40		spinel			5

This could be due to differences in vacancy concentrations for the thin films as compared to bulk samples. Appendices B-E reports the electrical data for the thin films made for this thesis.

A study was performed to determine the effect of the film annealing temperature on TCR. A range of temperatures was chosen between 430°C and 1030°C. As shown in the XRD data, films heat-treated at 430°C are X-ray amorphous while films annealed at 1030°C are highly crystalline. It is clear from Figure 4.36 that the highest average TCR values result from the highly crystalline films and the X-ray amorphous films.

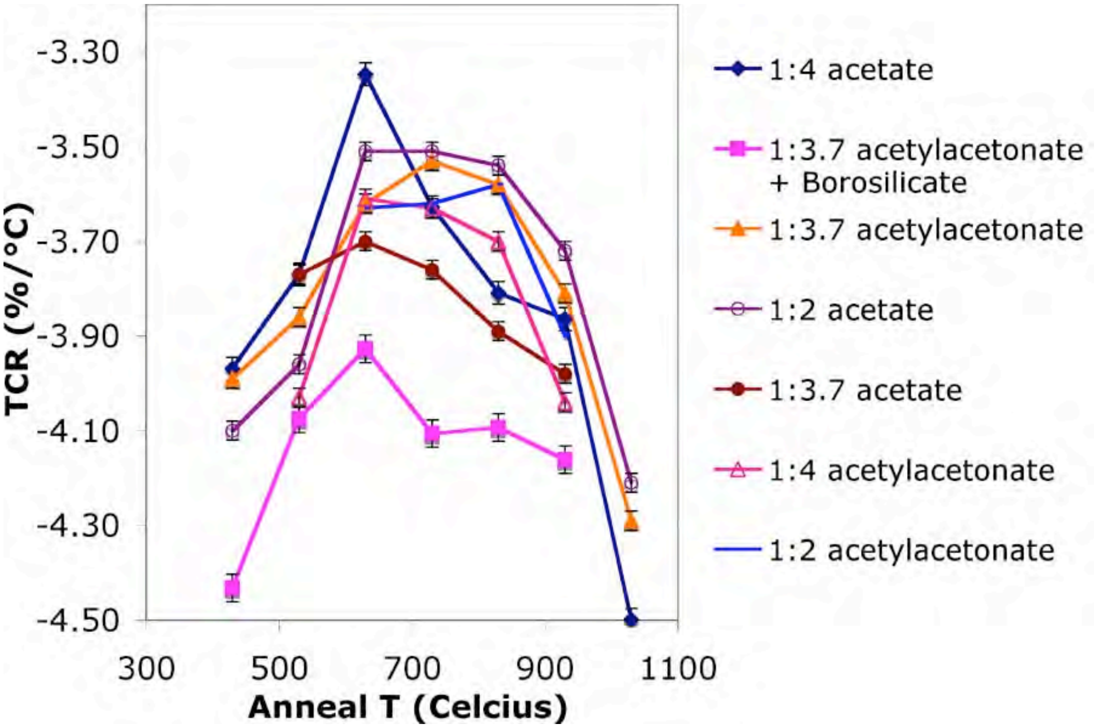

Figure 4.36: Average TCR values found over a temperature range between 295 K and 373 K as a function of annealing temperature for various nickel manganite compositions

It was also found that the TCR values and the film resistivity were correlated. That is higher resistivity values generally correspond to higher TCR values. This is shown in Figure 4.37.

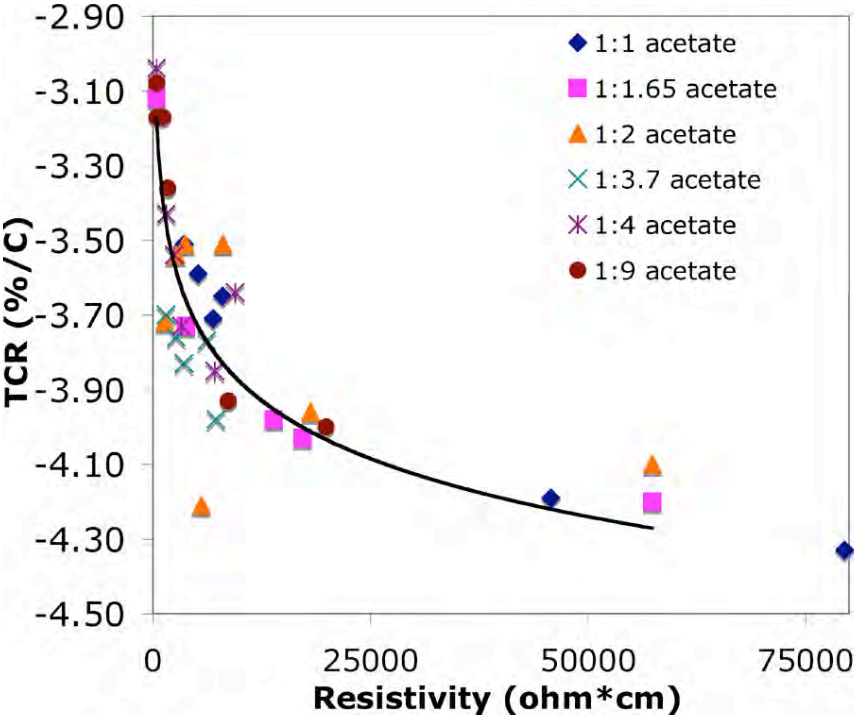

Figure 4.37: Average TCR values found over a temperature range between 295 K and 373 K with 90% confidence limit of ± 0.02 %/K as a function of resistivity; the trend line is only a guide to the eye.

In Figure 4.37, a few films exhibit high TCR, greater than -3 %/K, coupled with lower resistivities, around 400 Ωcm. The common factor between these films is their processing temperatures. They were annealed between 530°C and 730°C. The compositions vary, 1:9, 1:4, and 1:1.65. It has been shown the 1:9 and 1:4 films contain two phases, the bixbyite and the spinel. The bixbyite phase, as will be shown shortly, tends to exhibit lower TCR and resistivity values compared to the spinel phase. The combination of the two phases in a composite allows for a favorable balance between TCR and resistivity to be achieved. This correlation should be further explored in future work. Figure 4.38 focuses on the low resistivity films that contain multiple phases.

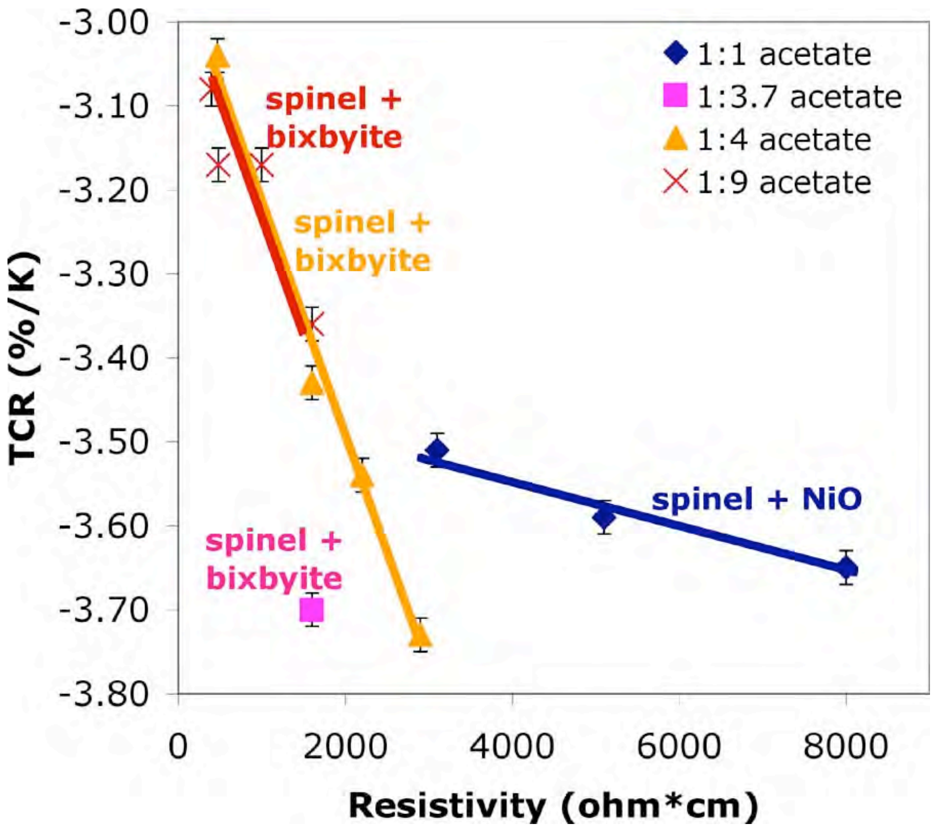

Figure 4.38: Average TCR values found over a temperature range between 295 K and 373 K with 90% confidence limit of ± 0.02 %/K as a function of resistivity for films exhibiting the bixbyite, spinel, and NiO phases

For films containing the bixbyite phase the trend between TCR and resistivity appears linear, and low resistivity films can be readily obtained. The slope of the TCR vs. resistivity curve is substantially different for the films containing spinel and rocksalt, and higher resistivities are generally obtained. This suggests that films containing bixbyite may be most useful for resistive bolometer applications, where lower resistivity films are generally desired.

When examining the lower resistivity films that appear to be single-phase spinel according to X-ray diffraction, the linear trend is less obvious (See Figure 4.39). The resistivities also tend to be above 2000 Ωcm. The outlying data point for the 1:1.65 composition suggests that there may be a second phase which was not detected in the X-ray diffraction patterns. If plotted in Figure 4.38, the 1:1.65 acetate film falls on the spinel and bixbyite curves, which enforces the point that this film most likely contains a second phase.

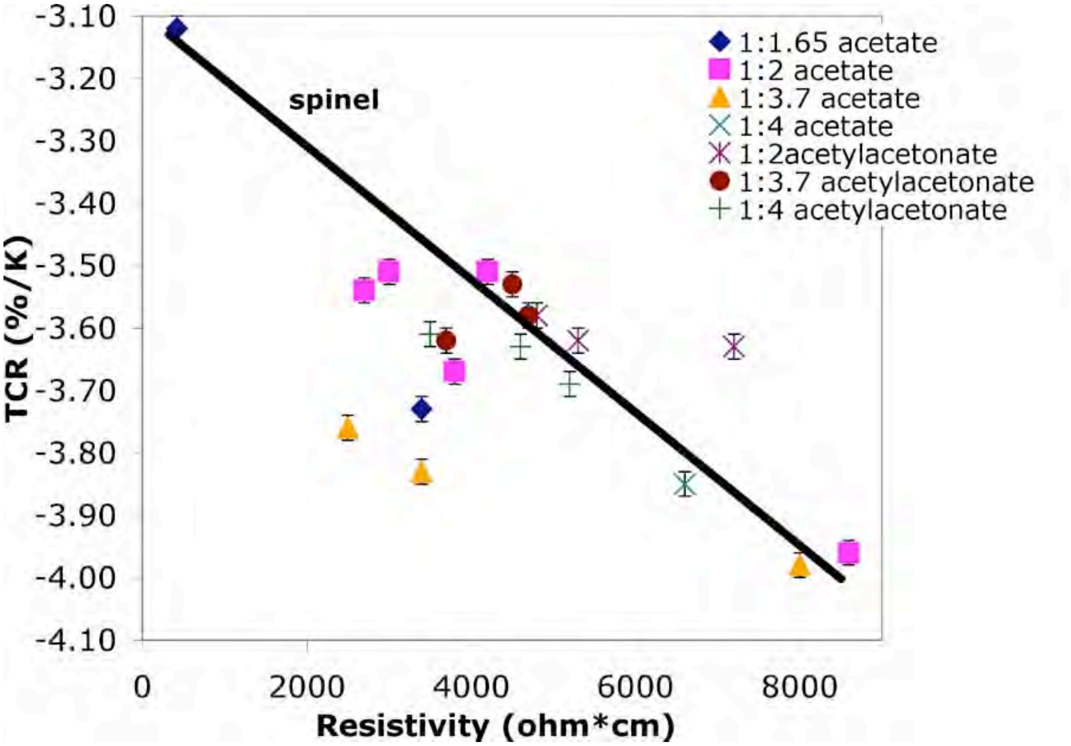

Figure 4.39: Average TCR values found over a temperature range between 295 K and 373 K with 90% confidence limit of ± 0.02 %/K as a function of resistivity for films exhibiting the spinel phase

The lowest resistivity films are the ones annealed between temperatures of 630°C and 830°C. The metastable spinel films that were annealed for 5 hours in Ar at 400°C show higher resistivities, but exhibit a similar trend with increasing TCR with resistivity. Figure 4.40 plots resistivity versus TCR for the metastable spinel films.

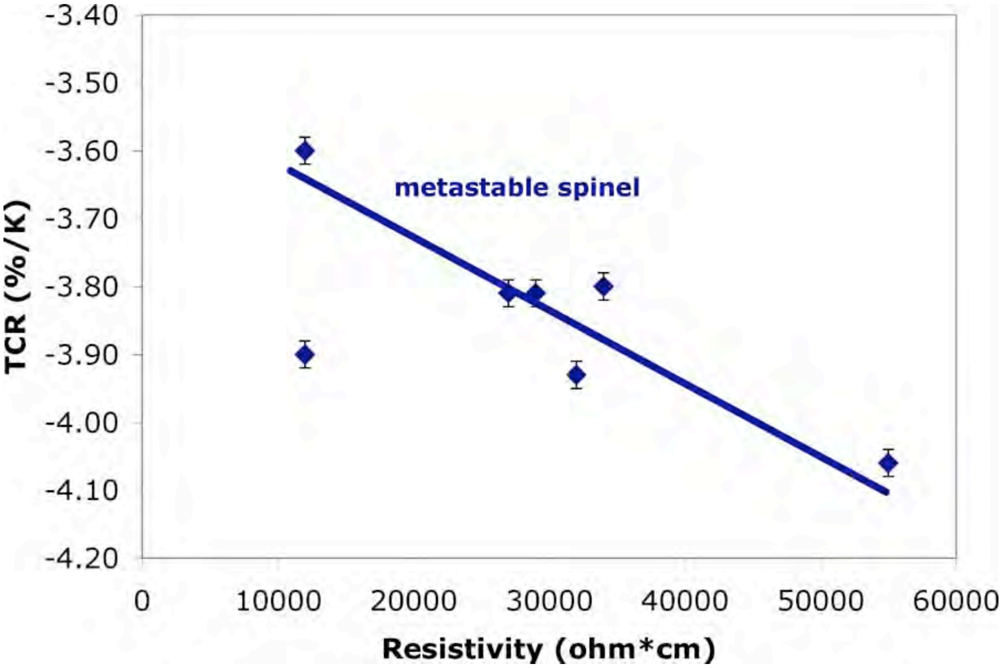

Figure 4.40: Average TCR values found over a temperature range between 295 K and 373 K as a function of resistivity for metastable spinel films that were annealed at 400°C in Ar for 5 hours

The resistivity measurements for these films were performed across the film using strip electrodes. If through-the-thickness measurements had been done, the conduction pathway would travel through single grains or grain boundaries due to the fact that the morphology for high temperature annealed films are a single grain thick. Due to the different pathways, differences in conductivity would be observed. By taking the measurements across the film, the conduction path consists of many grains and grain boundaries.

For the low temperature annealed films, in particular the metastable spinel films annealed in Ar for 5 hours at 400°C, the morphology is quite different. This could explain why the resistivity values increased. The film is made of layers of nano grains separated by an interface (the eight layers of solution that were spun on can be identified) as pictured in Figure 4.41.

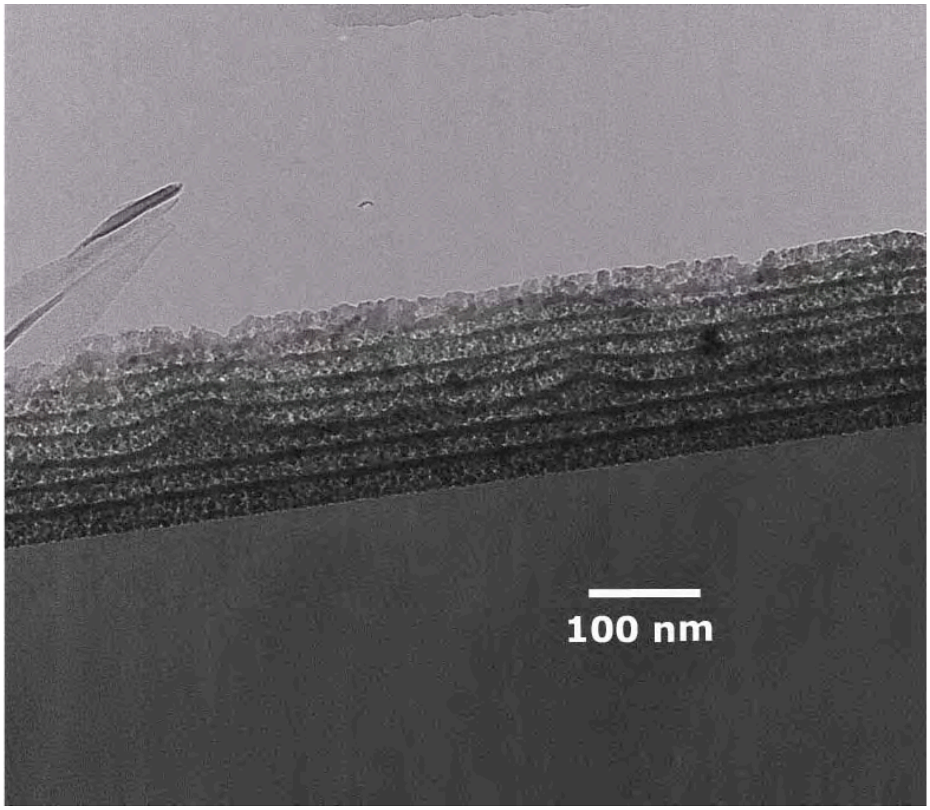

Figure 4.41: TEM image of a metastable spinel Ni:Mn 1:3.7 acetate film annealed at 400°C in Ar for 5 hours [compliments of David Saint-John]

Activation energy, E_a, follows the same trends as TCR as they are directly related to each other (Equation 3.3). This relationship is shown in Figure 4.42, which contains the data from all the films synthesized from the acetate solutions (compositions ranging from 6:1 to 1:9) and the acetylacetonate solutions (compositions ranging between 1:2 to 1:4).

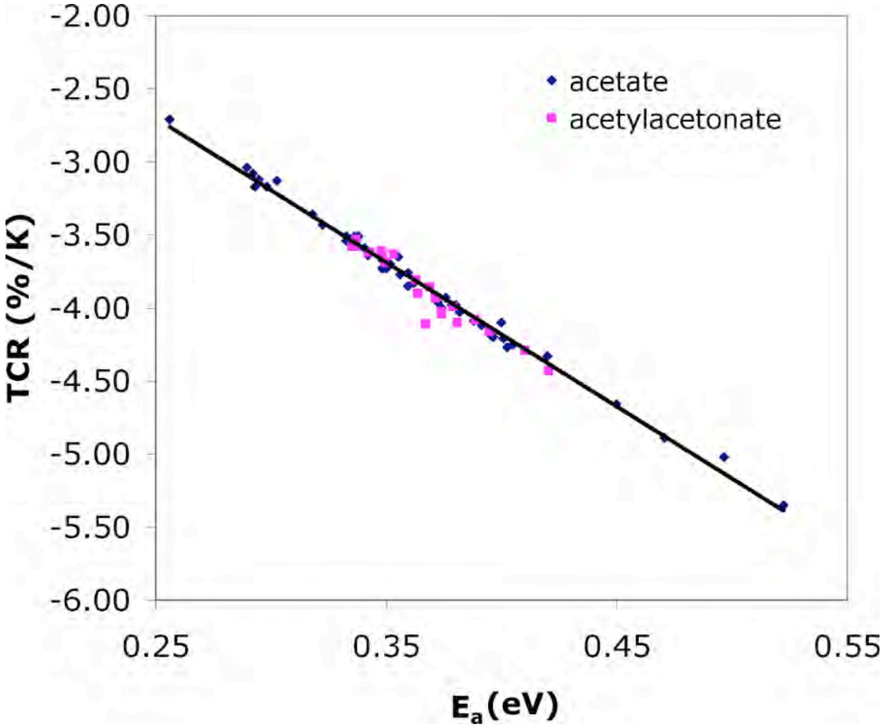

Figure 4.42: Average TCR values found over a temperature range between 295 K and 373 K as a function of E_a for acetate and acetylacetonate films (6:1 to 1:9) that were annealed in air for 1 minute between 430°C and 1030°C

Bulk thermistor properties were compared to thin films processed in the higher temperature region, where the spinel phase is thermodynamically stable. The electrical properties shown in Table 4.3 demonstrate that single-phase nickel manganite spinel films are comparable to those of the bulk.

Table 4.3: Electrical properties of bulk spinel ceramics (in black) [6] compared to experimental results from spinel thin films annealed at 930°C (in red). The TCR values reported are averages found over a temperature range between 295 K and 373 K with 90% confidence limit of ± 0.02 %/K.

Mn	Co	Ni	Cu	ρ at 298K (Ωcm)	E_a (eV)	TCR (%/K)
56	8	16	20	10	0.22	-2.90
65	9	19	7	100	0.17	-2.20
70	10	20		1000	0.31	-4.00
67		33		5600	0.35	-3.72
77		23		7200	0.38	-3.98
80		20		7100	0.36	-3.85
85		15		10000	0.37	-4.70
94		6		100000	0.40	-5.10

It is clear from the table that the resistivity and TCR values can be optimized based on composition. In particular, doping nickel manganites with cobalt and copper can lower the resistivity.

Figure 4.43 shows a comparison of films prepared from acetate-based and acetylacetonate-based solutions.

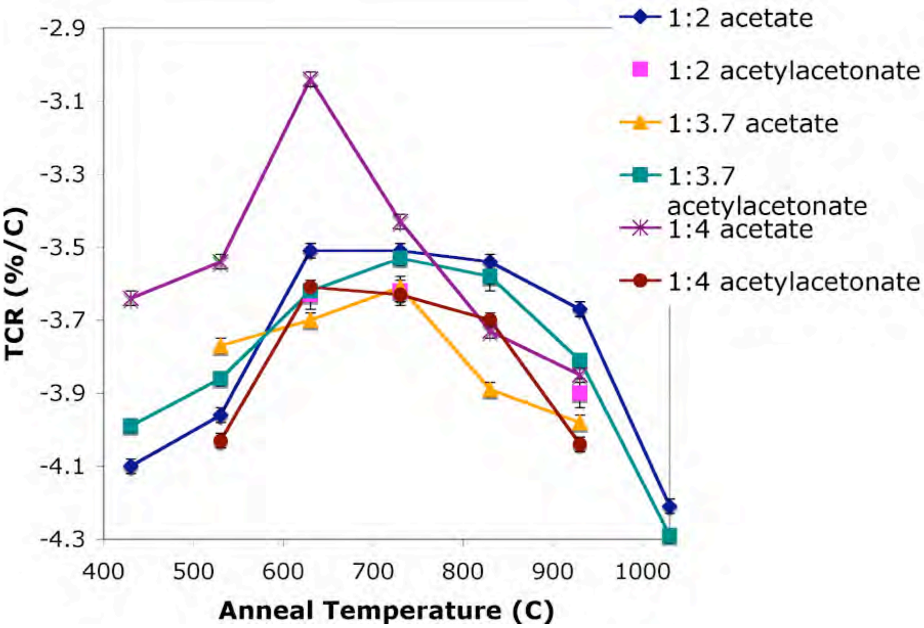

Figure 4.43: Average TCR values (over a temperature range between 295 K and 373 K) of samples made from acetate-based solutions compared to acetylacetonate solutions

While considerable scatter is observed, the majority of the acetylacetonate samples have a higher TCR value than the acetate-based samples. It was hypothesized that the differences observed between films of the same composition were associated with phase assemblage. That is, 1:4 films made from the acetylacetonate solution showed primarily the spinel phase, while some of those made from the acetate route possessed two phases. It was shown previously in section 4.2.1.1.3.2 that the pyrolysis procedures play a large role on the final annealing condition. When residual organics remain in the films a C rich atmosphere forms above the film during the anneal creating a reducing environment, which favors spinel formation. Infrared measurements could be used to identify when the organics are completely removed. Table 4.4 shows average TCR values of the single-phase acetylacetonate samples compared to the two-phase acetate samples for the 1:4 composition. The TCR values for the single-phase acetylacetonate films appear to be consistently higher than the two-phase films.

Table 4.4: Average TCR values found over a temperature range between 295K and 373K with ± 0.02 %/°C 90% confidence limits for the Ni:Mn 1:4 films

Anneal T (°C)	**TCR (%/°C)**	
	Acetate	***Acetylacetonate***
530	-3.54	-4.03
630	-3.04	-3.61
830	-3.43	-3.63

To judge what the presence of bixbyite does to the overall TCR value, 1:9 acetate films were synthesized within the bixbyite region of the phase diagram. Table 4.5 displays the average TCR values of films that are primarily bixbyite.

Table 4.5: Average TCR values for the 1:9 films found over a temperature range between 295 K and 373 K with ± 0.02 %/°C 90% confidence limits

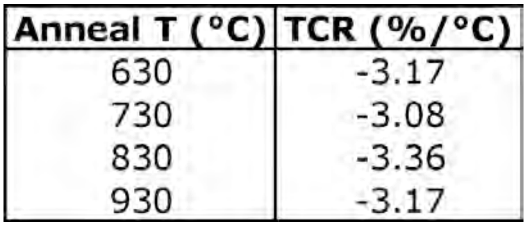

Anneal T (°C)	TCR (%/°C)
630	-3.17
730	-3.08
830	-3.36
930	-3.17

Table 4.6 compares the TCR and resistivity values for spinel films versus bixbite films to those of composite films.

Table 4.6: TCR and resistivity values for films annealed in air for one minute in the RTA between temperatures of 630°C and 930°C. The TCR values reported are averages found over a temperature range between 295 K and 373 K with 90% confidence limit of ± 0.02 %/K.

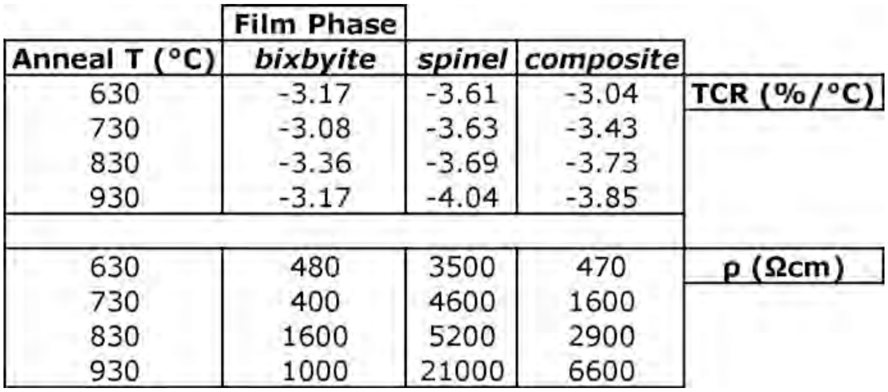

	Film Phase			
Anneal T (°C)	***bixbyite***	***spinel***	***composite***	
630	-3.17	-3.61	-3.04	**TCR (%/°C)**
730	-3.08	-3.63	-3.43	
830	-3.36	-3.69	-3.73	
930	-3.17	-4.04	-3.85	
630	480	3500	470	**ρ (Ωcm)**
730	400	4600	1600	
830	1600	5200	2900	
930	1000	21000	6600	

The TCR values for bixbyite films are consistently below those of the single-phase spinel films. This suggests that using composite mixing rules it may be possible to estimate the phase assemblage from TCR values.

Mixing rules were employed in an attempt to calculate the amount of different phases in a composite. Weiner's rule, which is derived based on an assumption of isolated spheres in a continuous matrix for a two-phase composite states (Equation 4.7) [92]:

$$(\sigma_m-\sigma_1) / (\sigma_m+2\sigma_1) = \phi_2 * [(\sigma_2-\sigma_1) / (\sigma_2+2\sigma_1)] \qquad \text{Equation 4.7}$$

The conductivity of the composite is given by σ_m, ϕ_2 is the volume fraction of the spheres, the conductivity of the matrix phase is represented by σ_1 and σ_2 is the conductivity for the sphere phase. Based on the measured conductivity values of single-phase films, the volume fraction of bixbyite in composite films was estimated using the mixing rules. The conductivity of bixbyite was found to be 1.17×10^{-3} $(\Omega\text{cm})^{-1}$ and the conductivity of spinel was found to be 2.19×10^{-5} $(\Omega\text{cm})^{-1}$. The volume fraction calculated for bixbyite in composite films do not match values determined by the lever rule as shown in Table 4.7.

Table 4.7: Volume fractions of bixbyite and spinel as calculated or determined by the mixing rule and the lever rule

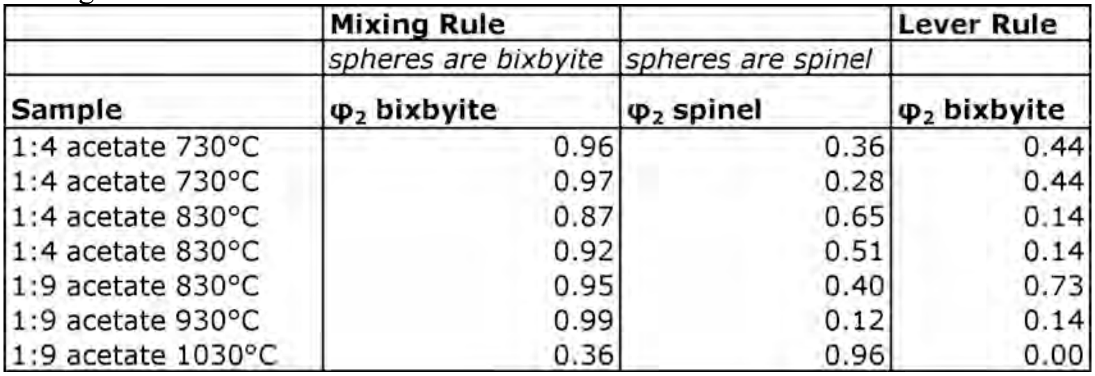

	Mixing Rule		**Lever Rule**
	spheres are bixbyite	*spheres are spinel*	
Sample	**φ_2 bixbyite**	**φ_2 spinel**	**φ_2 bixbyite**
1:4 acetate 730°C	0.96	0.36	0.44
1:4 acetate 730°C	0.97	0.28	0.44
1:4 acetate 830°C	0.87	0.65	0.14
1:4 acetate 830°C	0.92	0.51	0.14
1:9 acetate 830°C	0.95	0.40	0.73
1:9 acetate 930°C	0.99	0.12	0.14
1:9 acetate 1030°C	0.36	0.96	0.00

It can be concluded that Weiner's rule modeling the composite as spheres in a matrix is not an accurate representation of the actual spinel-bixbyite thin film composite.

Films annealed at 400°C in reducing atmospheres for 5 hours show comparable TCR values to those annealed at higher temperatures, but the resistivities are about an order of magnitude higher. For a variety of compositions, Table 4.8 displays the properties.

Table 4.8: Electrical properties of films annealed at 400°C in Ar for 5 hours. TCR values are averages found over a temperature range between 295 K and 373 K with a 90% confidence limit of ± 0.02 %/K.

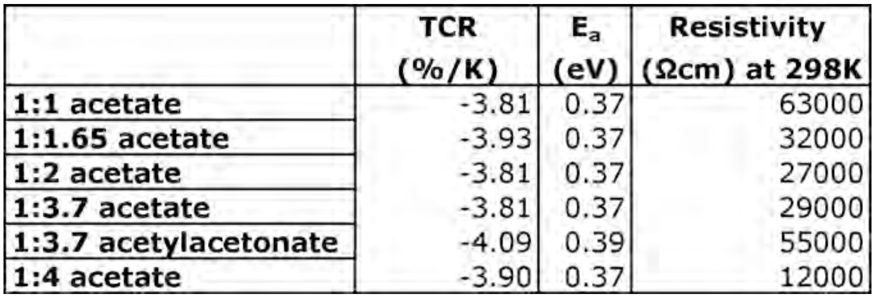

	TCR (%/K)	E_a (eV)	Resistivity (Ωcm) at 298K
1:1 acetate	-3.81	0.37	63000
1:1.65 acetate	-3.93	0.37	32000
1:2 acetate	-3.81	0.37	27000
1:3.7 acetate	-3.81	0.37	29000
1:3.7 acetylacetonate	-4.09	0.39	55000
1:4 acetate	-3.90	0.37	12000

As the Mn content increases, the TCR and E_a values remain fairly constant while the resistivity decreases, with the exception of the acetylacetonate film. For bulk nickel manganites, Gillot et al. reports a similar decrease in conductivity with decreasing Mn, due to an effective decrease in the carrier concentration [21]. In the bulk materials, a maximum in conductivity occurs at the composition, where the number of Mn^{3+} cations is equal to the number of Mn^{4+} cations on octahedral sites [21]. Gillot reports that for samples pretreated at 600°C the maximum in the conducitivity falls at x = 0.69 and for samples pretreated at 350°C, x = 0.74, where x is the amount of Ni in $Ni_xMn_{3-x}O_4$ [21]. The films in Table 4.7 range from x = 0.6 to 1.5. It is possible that a maximum exists, but in order to observe it compositions below x = 0.6 would need to be measured. It should also be noted that the finite level of cation vacancies observed in the thin films (See section 4.2.1.3) may also affect the composition of maximum conductivity.

Thus, it is believed that the conductivity of the metastable spinel films prepared here increases with Mn concentration due to the fact that if more Mn is present, there is a greater probability of having a Mn^{3+} and Mn^{4+} next to each other for hopping conduction. The amount of energy required to cause an electron to hop between the two cations doesn't appear to change with composition and therefore TCR also doesn't change. It should be noted that constant TCRs and activation energies are not observed for other sets of films processed at the same temperature because changing compositions at higher temperatures causes changes in phase as well.

The processing temperature for the metastable films is low enough to be compatible for integration into a microfabrication process. The stability of these properties will be shown in section 4.4.

4.3.3 Properties as a Function of Film Thickness

Thin film samples were made from three solutions: a 1:4 acetate solution, the 1:3.7 acetylacetonate solution doped with borosilicate, and the undoped 1:3.7 acetylacetonate solution. A study was done to determine if the thickness of the film affected the TCR value. Figure 4.44 shows average TCR values for the samples made from the three different solutions ranging from 6 to 16 spin-coated layers, (thicknesses between 100 nm and 350 nm). The data shows no specific pattern; no statistical difference in TCR was observed.

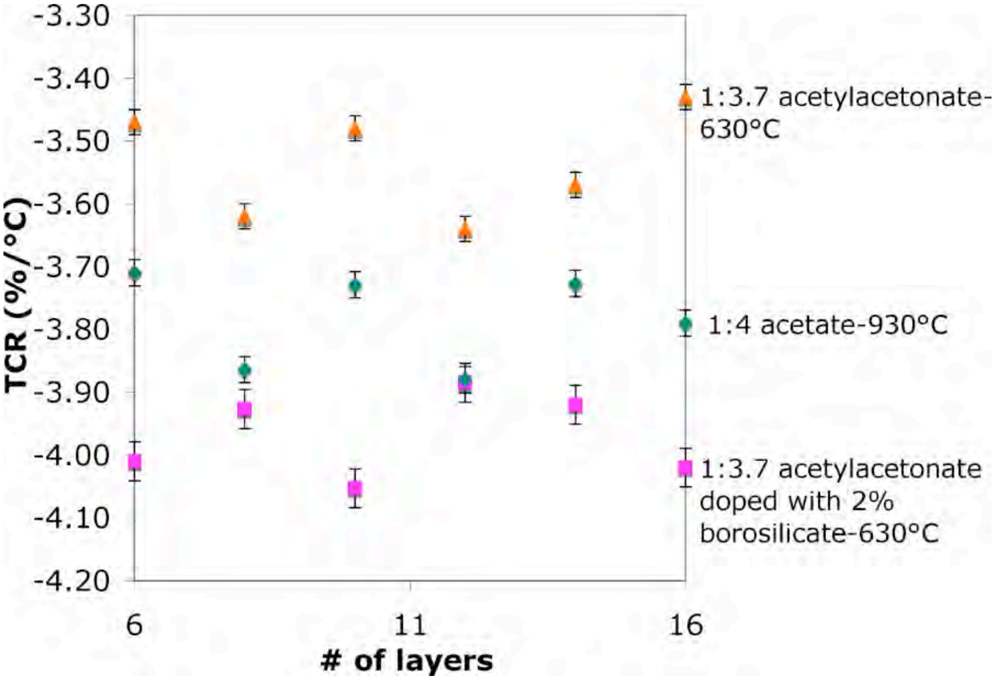

Figure 4.44: Average TCR values found over a temperature range between 295 K and 373 K for three different types of films varying in thickness between 100 nm and 350 nm

4.4 Stability of Film Properties

During the fabrication of the microbolometer, the CMOS (complementary metal oxide semiconductor) wafer undergoes back end-of-the-line semiconductor processes. It is known that VO_x films often undergo changes in their electrical properties during the relatively modest temperature and oxygen partial pressure excursions used during these steps [93]. One of the rationales for choice of nickel manganite as an alternative is based on the fact that it is a controlled valence semiconductor, in which the carrier concentration is largely fixed by the chemistry, rather than by reactions with the ambient gas phase. Consequently, it is important to understand how the crystalline and amorphous films react to different heat treatments to determine if these films are acceptable alternatives for microbolometer applications.

4.4.1 Well-Crystallized Films

Films crystallized at 630°C and 730°C/830°C were held at 600°C and 700°C respectively for 1, 5, and 15 hours in air or in flowing nitrogen to determine how the TCR changes with longer anneal times. Films made from the 1:4 acetate solution and annealed at 730°C and 830°C and films from the 1:3.7 acetylacetonate solution and annealed at 630°C were tested. The TCR and resistivity was measured soon after crystallization and then after about two months in ambient air. The values are shown in Table 4.9 and TCR is plotted in Figure 4.45.

Table 4.9: Average TCR values found over a temperature range between 295 K and 373 K (± 0.02 %/°C 90% confidence limits) and room temperature resistivity values of four different films before and after heat treatment

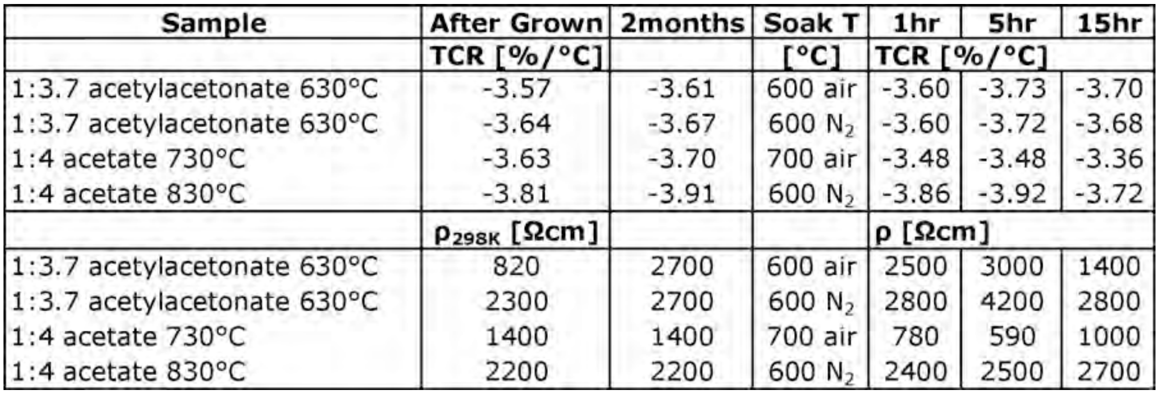

Sample	After Grown	2months	Soak T	1hr	5hr	15hr
	TCR [%/°C]		[°C]	TCR [%/°C]		
1:3.7 acetylacetonate 630°C	-3.57	-3.61	600 air	-3.60	-3.73	-3.70
1:3.7 acetylacetonate 630°C	-3.64	-3.67	600 N_2	-3.60	-3.72	-3.68
1:4 acetate 730°C	-3.63	-3.70	700 air	-3.48	-3.48	-3.36
1:4 acetate 830°C	-3.81	-3.91	600 N_2	-3.86	-3.92	-3.72
	ρ_{298K} [Ωcm]			ρ [Ωcm]		
1:3.7 acetylacetonate 630°C	820	2700	600 air	2500	3000	1400
1:3.7 acetylacetonate 630°C	2300	2700	600 N_2	2800	4200	2800
1:4 acetate 730°C	1400	1400	700 air	780	590	1000
1:4 acetate 830°C	2200	2200	600 N_2	2400	2500	2700

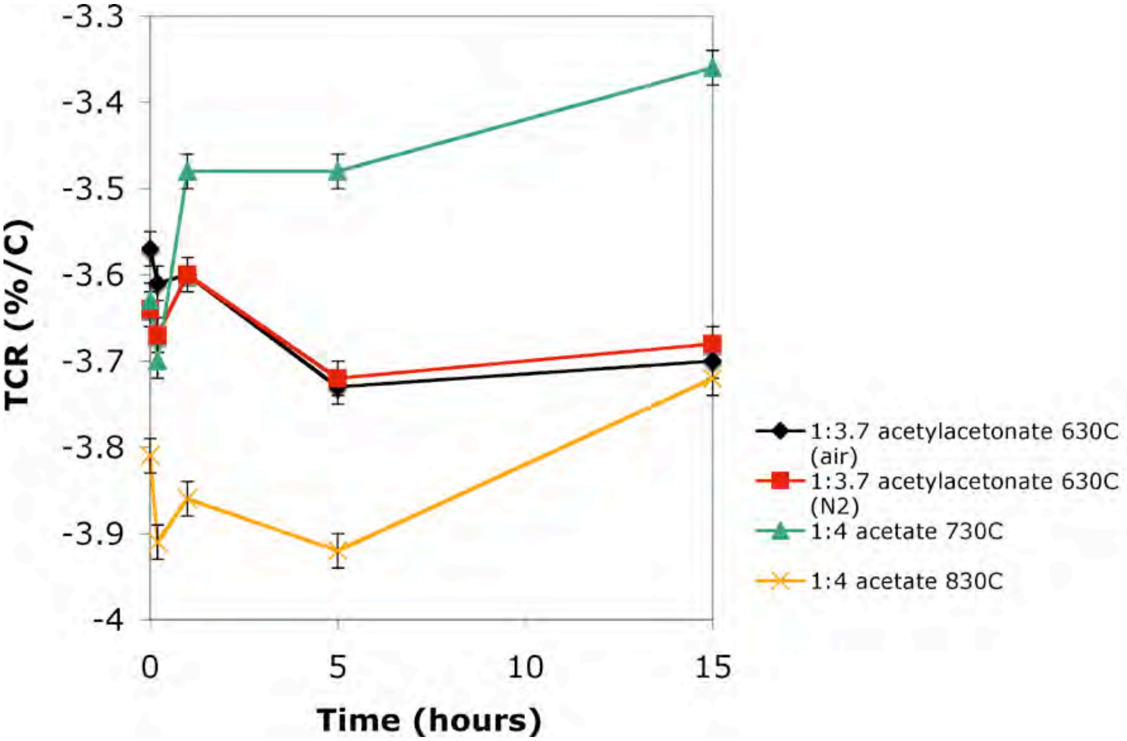

Figure 4.45: Stability of average TCR values found over a temperature range between 295 K and 373 K following high temperature treatments

There is no significant difference in TCR values associated with long-term exposures to ambient air for any of the films. No trend was observed for the fluctuation in resistivity. This suggests that the capping layers required in VO_x thermistor arrays (to prevent oxygen exchange with the ambient) will not be necessary for nickel manganite films. Moreover, only modest changes in properties were observed after extended exposures to temperatures close to those used to heat-treat the films. All four of these films were heat-treated in two-phase regimes on the phase diagram. It is possible that the small decrease in TCR for the films from acetate precursors during the heat-treatment could be due to the material approaching thermodynamic equilibrium. A second phase, bixbyite, could be crystallizing. Bixbyite has been shown to exhibit lower TCR than spinel material. In any event, the property changes are very small. In contrast, VO_x films exposed to comparable anneals undergo significant changes in properties and morphology [94].

Thus, crystalline nickel manganite films are substantially more stable than the VO_x currently employed in bolometer arrays.

4.4.2 Low-Temperature Processed Films

It is also interesting to consider whether the films processed at much lower temperatures will also have reasonable property stability. For this purpose, X-ray amorphous film that had been RTA annealed for 1 minute at 430°C, as well as crystalline films prepared by annealing at 400°C in a reducing ambient were investigated. Both sets of films were soaked at 400°C for 1, 5, and 15 hours in air. The average TCR values were measured after each treatment as shown in Figure 4.46.

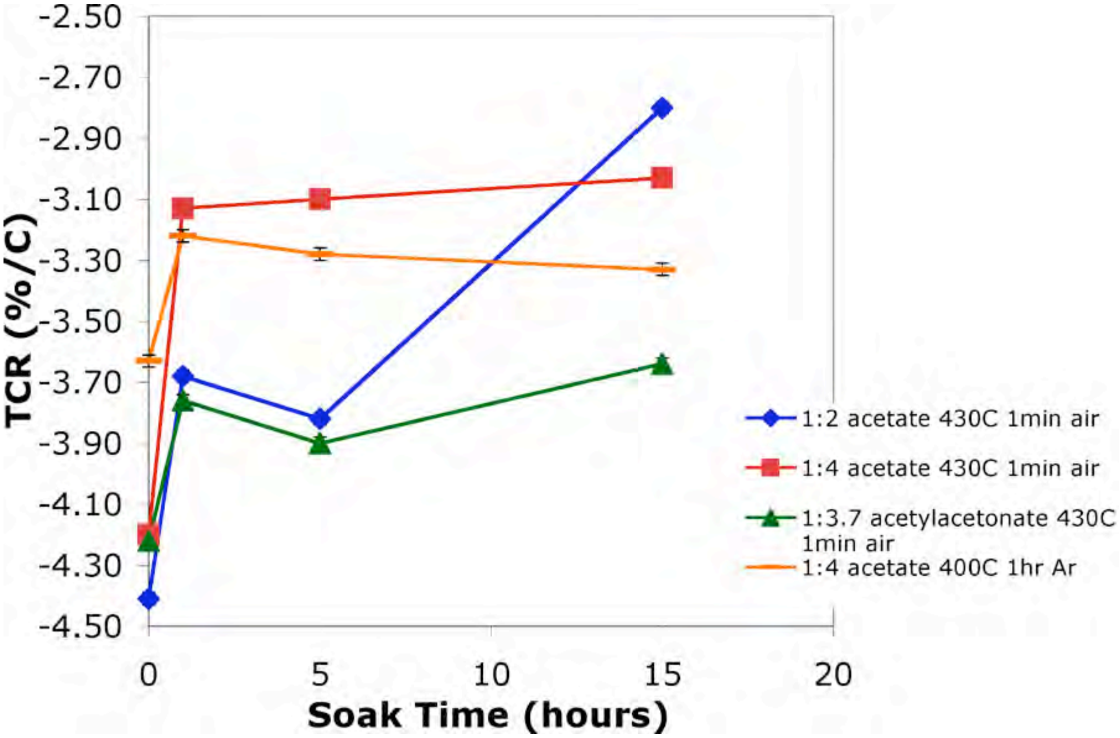

Figure 4.46: Average TCR values found over a temperature range between 295 K and 373 K of X-ray amorphous films heat-treated in air at 430°C for 1 minute and a crystalline film heat-treated in Ar at 400°C for 1 hour. Films were measured after various soak times at 400°C in air.

For the RTA'd films, three different compositions were studied, films with Ni:Mn ratios of 1:2 or 1:4 prepared from the acetate route, and films with Ni:Mn ratios of 1:3.7 from acetylacetonate solutions. In both cases, after the first hour anneal at 400°C, a large drop in TCR (between 0.4 and 1.1%/°C) was observed. After 5 and 15 hours there was less change. To determine the origin for the changes in TCR XRD analysis was performed after the three aging heat treatments. The results show that the bixbyite (B) phase and the ilmenite (I) phase, as shown in the Figure 4.47, were crystallized. The lower TCR values of these phases are responsible for the observed drop in TCR.

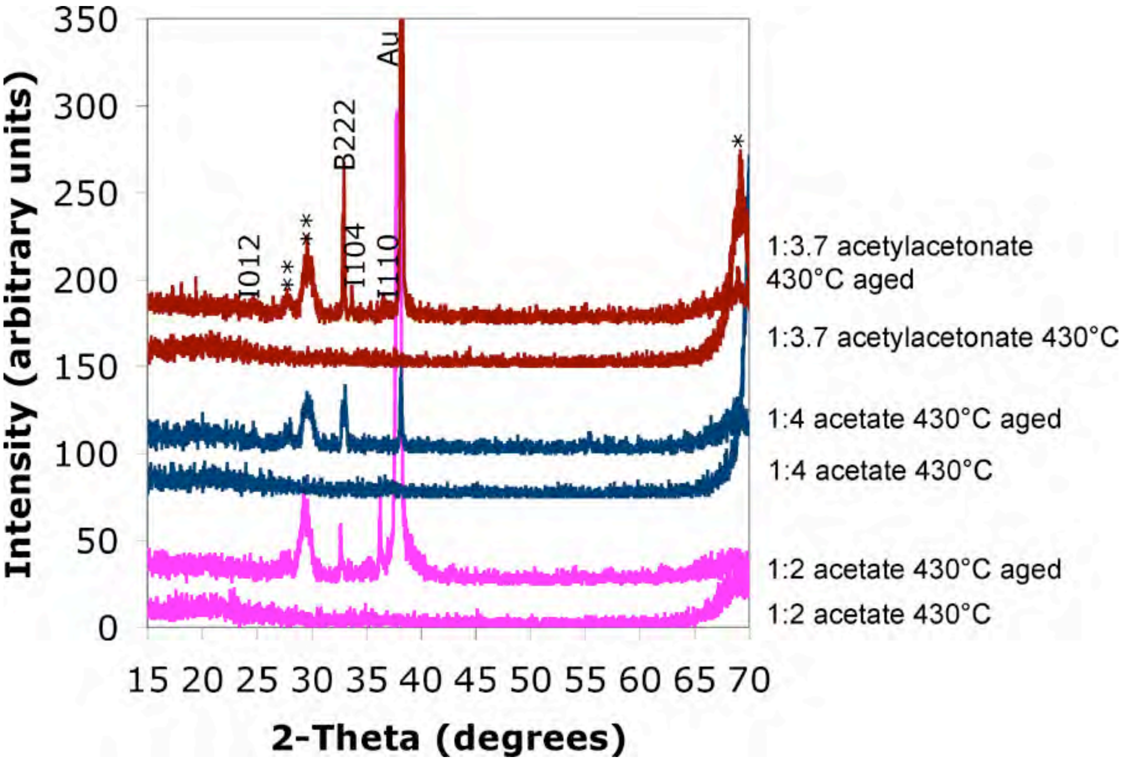

Figure 4.47: XRD patterns of the Ni:Mn 1:2 acetate 430°C, 1:4 acetate 430°C, 1:3.7 acetylacetonate 430°C. The amorphous films underwent the initial 1 minute anneal while the crystallized films underwent a series of aging heat treatments for 1 hour, 5 hours, and 15 hours at 400°C in air. The indexed peaks represent the ilmenite (I) and the bixbyite (B) phases. Peaks with an "*" are from the substrate, peaks with "**" are unknown, and "Au" are from the gold electrodes.

Before the 1:2 acetate film was aged it had a resistivity of 66000 Ωcm. After 15 hours at 400 °C, it dropped to 7400 Ωcm. The other films also underwent a similar decrease in resistivity after being aged at 400 °C. The 1:4 acetate films dropped from 16000 Ωcm to 500 Ωcm and the 1:3.7 acetylacetonate film decreased from 60000 Ωcm to 16000 Ωcm.

There are two possible reasons why the films appeared to be X-ray amorphous following the 430°C RTA anneal. First, it is possible that nuclei of the bixbyite and ilmenite phases were present in the X-ray amorphous films, but were not provided enough time and temperature for growth. The other possibility is that because of organics present, there was not sufficient oxygen present to allow the formation of these two phases. With longer anneal times the remaining organics from the pyrolysis are removed, leading to crystallization of the equilibrium phases. TEM analysis could confirm this.

In order to check the stability of the metastable spinel phase (for a film annealed at 400°C for 1 hour in Ar), it was also annealed at 400°C in air. A smaller drop in TCR can be seen in the metastable spinel film compared to the initially X-ray amorphous film annealed for 1 minute in air, Figure 4.48.

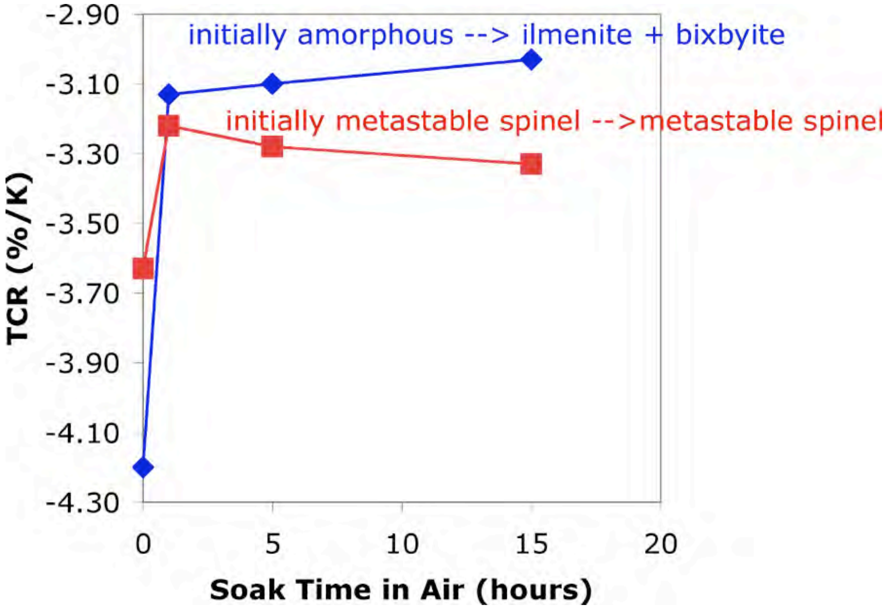

Figure 4.48: Average TCR values found over a temperature range between 295 K and 373 K of an X-ray amorphous films heat-treated in air at 430°C for 1 minute and a metastable spinel film heat-treated in Ar at 400°C for 1 hour. Films were measured after various soak times at 400°C in air.

After an initial drop in TCR of 0.4% after the first hour, the TCR value did not decrease further on subsequent annealing. This film shows no change in crystallinity after 21 hours at 400°C. The XRD patterns are shown in Figure 4.49. This suggests that the metastable spinel film is kinetically limited from transforming to the stable phase.

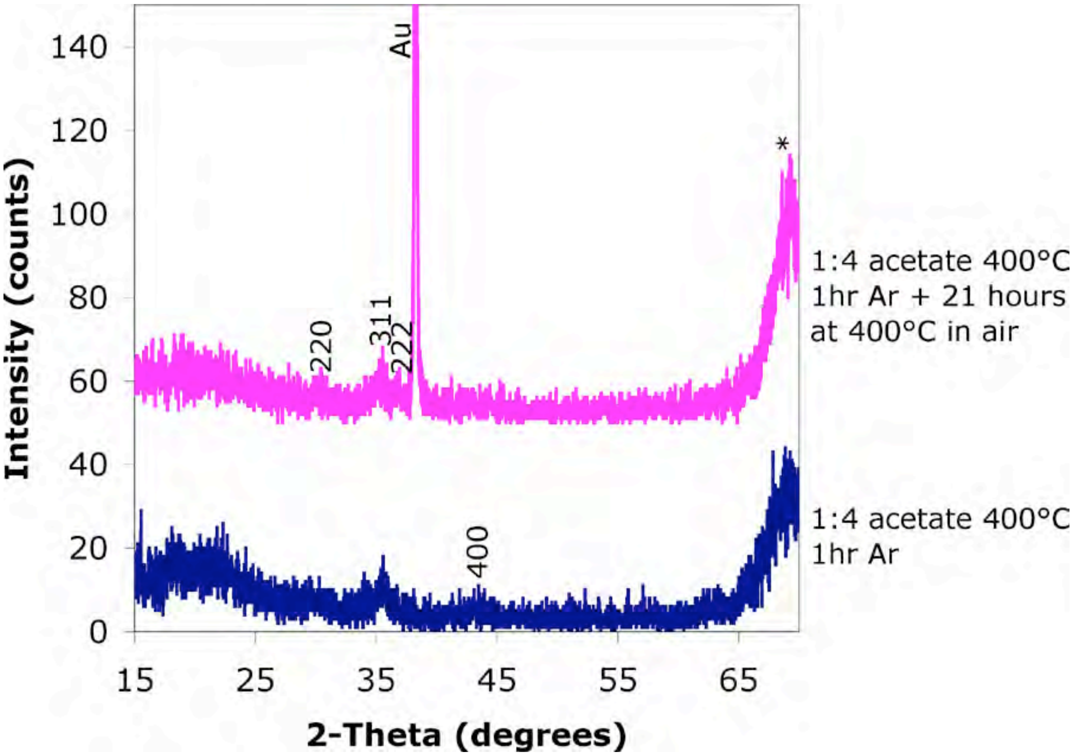

Figure 4.49: XRD patterns for Ni:Mn 1:4 acetate film annealed for 1 hour in Ar before and after heat-treatment for 21 hours at 400°C in air. The indexed peaks represent the spinel phase. Peaks with an "*" are from the substrate and "Au" are from the gold electrodes.

Because of the results obtained from the 400°C aging test, other samples, including the 1:1 line compound, were chosen for similar heat treatments. During the 400°C heat-treatment, the ilmenite phase crystallized in both the 1:1 and 1:1.65 compositions (See Figures 4.50 and 4.51).

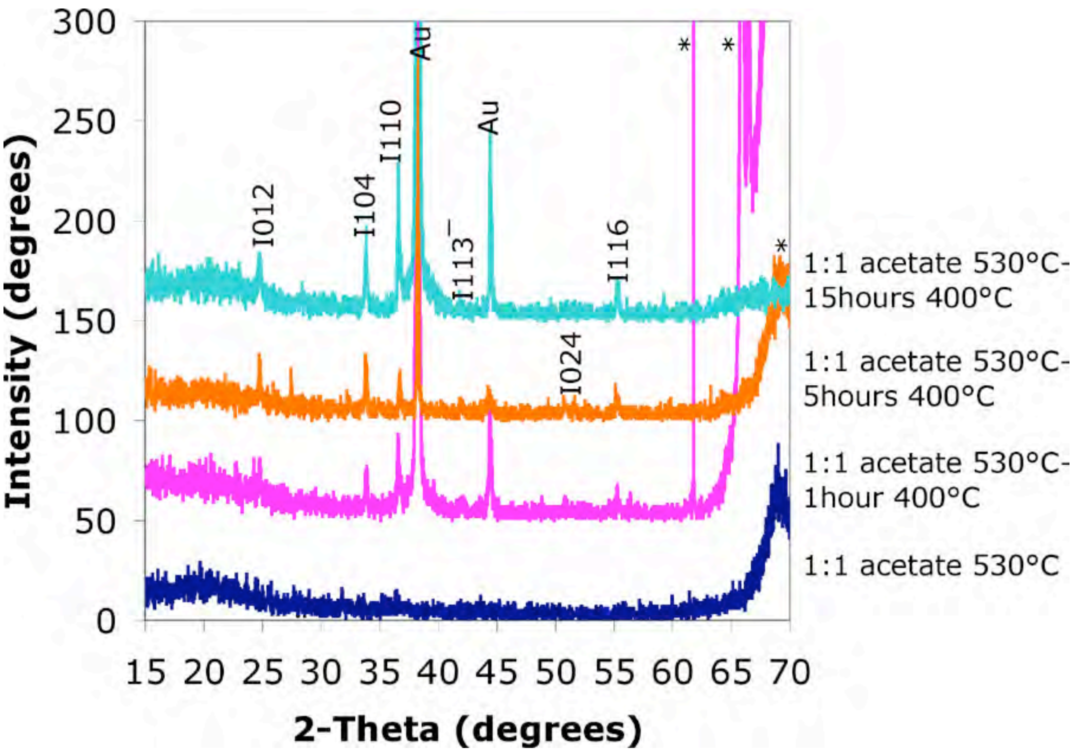

Figure 4.50: XRD patterns of the Ni:Mn 1:1 acetate film annealed at 530°C before and after aging for 1 hour, 5 hours, and 15 hours at 400°C in air. The indexed peaks refer to the ilmenite phases, "I". Peaks with an "*" are from the substrate and "Au" are from the gold electrodes.

According to the bulk phase diagram, ilmenite forms for the 1:1 Ni:Mn ratio between 400°C and 760°C. An increase in the crystallinity on annealing was also observed in the Ni:Mn 1:1 film from acetate precursors RTA annealed at 530°C film.

Annealing results for the Ni:Mn 1:1.65 films from acetate precursors RTA'd at are shown in Figure 4.51. Again, it is clear that the films crystallize given a sufficient thermal budget. This crystallization is the major reason for the observed change in the electrical properties.

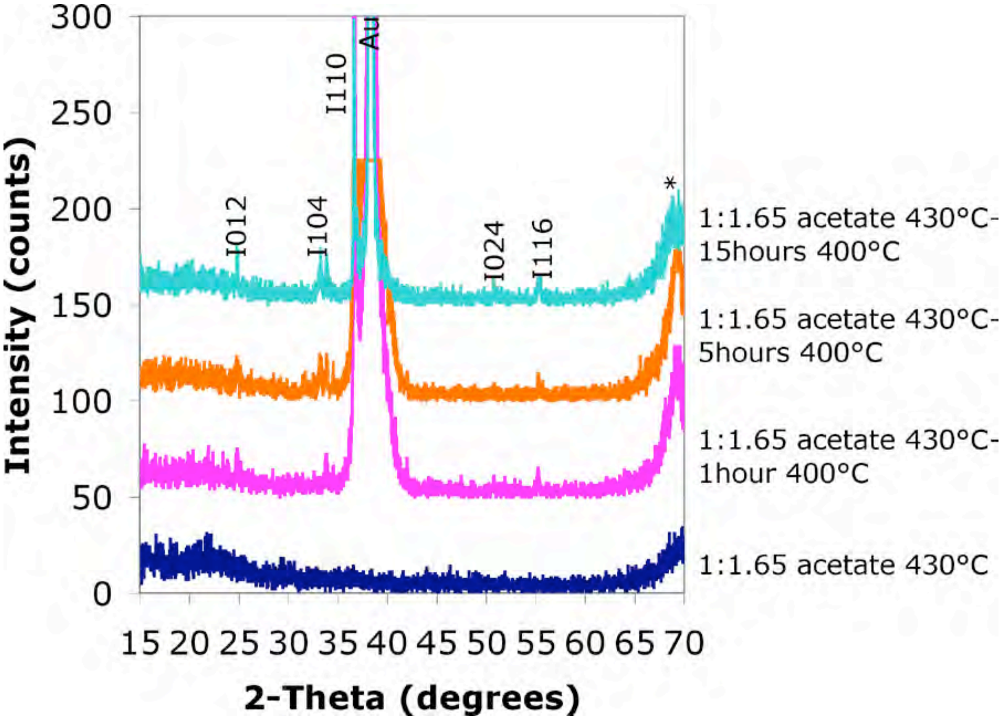

Figure 4.51: XRD patterns of the Ni:Mn 1:1.65 acetate film annealed at 430°C before and after aging for 1 hour, 5 hours, and 15 hours at 400°C in air. The indexed peaks refer to the ilmenite phases, "I". Peaks with an "*" are from the substrate and "Au" are from the gold electrodes.

The results for the metastable spinel films annealed in reducing atmospheres at 400°C are quite promising for microbolometer applications. Consequently, the aging behavior of some of the films was examined. The 1:4 acetate and 1:3.7 acetylacetonate films were aged at 150°C in a box oven in ambient air for various intervals up to 500 hours. The TCR values were obtained before the aging and then after various times approximately on a logarithmic scale. Table 4.9 displays the average TCR as a function of aging time at 150°C.

Table 4.9: Average TCR values found over a temperature range between 295 K and 373 K for spinel films annealed at 400°C for 5 hours in Ar after aging at 150°C for various times. Values are reported with a 90% confidence limit of ± 0.02 %/K.

		TCR (%/°C)							
Time (hours)		**1**	**4**	**14**	**44**	**138**	**298**	**490**	**537**
Sample	**1:4 acetate**	-3.73	-3.65	-3.76	-3.73	-3.73	-3.86	-3.79	-3.56
	1:3.7 acetylacetonate	-4.01	-4.04	-4.06	-4.06	-4.15	-4.00	-4.08	-4.12

The TCR does not appear to vary by any significant amount. 90% confidence limits were ± 0.02%/K error in the TCR value. There is also error that results from the gradual degradation of the gold electrodes with prolonged heat-treatment. Nonetheless, the changes observed are small enough to suggest excellent stability of the low temperature crystallized films during post-processing.

The aging coefficient of nickel manganite films was reported to range from 2% to 20% [58]. As mentioned in the Experimental Procedures chapter, the aging took place at 150°C in air for a period of approximately 500 hours. Room temperature (298 K) resistance measurements were taken at a variety of times to generate a plot of the change in resistance as a function of time. Resistances tend to increase over time and they tend to increase the most within the first 100-200 hours before leveling out. The aging coefficient is the percentage the resistance drifts with time. From the aging study it was found that the aging coefficient is 6.5% for the 1:4 acetate film annealed for 5 hours at 400°C in Ar as illustrated in Figure 4.52.

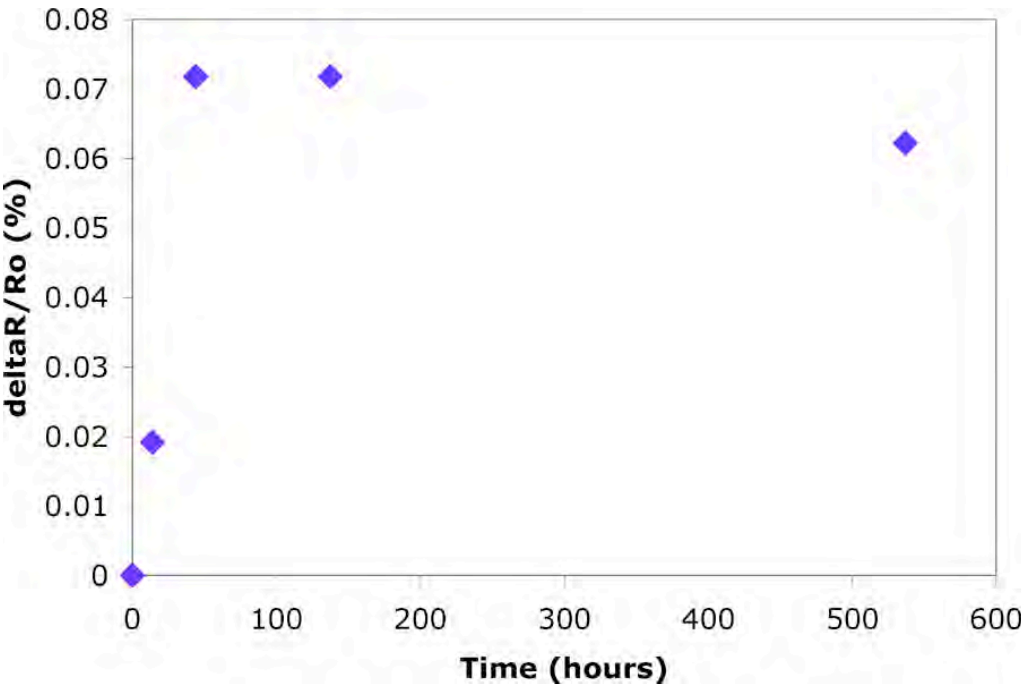

Figure 4.52: Drift in resistance of a Ni:Mn 1:4 acetate film annealed at 400°C in Ar for 5 hours after 537 hours of aging at 150°C in air

New electrodes were deposited after about 100 hours of aging due to degradation of the original electrodes. The aging coefficient is quite comparable to the values reported in the literature. The resistance appears to level out after about 100 hours.

4.4.3 Phase Stability during 600°C Anneals

In contrast to the amorphous films, which showed large changes in the electrical properties associated with crystallization at elevated temperatures, it was found that the metastable crystalline films were far more stable during high temperature annealing at 600°C (See Figures 4.53 to 4.55). XRD was used to observe how the phases will change with longer anneal times. The films 1:4 acetate grown at 430°C, 1:1.65 acetate grown at 630°C, and 1:9 acetate grown at 630°C were soaked in air in a tube furnace at 600°C for 24, 96, and 192 hours in air (the samples were exposed to the ramp rates of the heat treatments). These films were X-rayed after each soak. The samples originally crystallized at 630°C in a RTA for one minute showed no sign of changing phase. That is, the crystallized spinel phase is stable during subsequent heat treatment. However, the 1:4 acetate sample (which was X-ray amorphous after the 430°C RTA step) crystallized into the bixbyite phase when held at 600°C as shown in Figure 4.53.

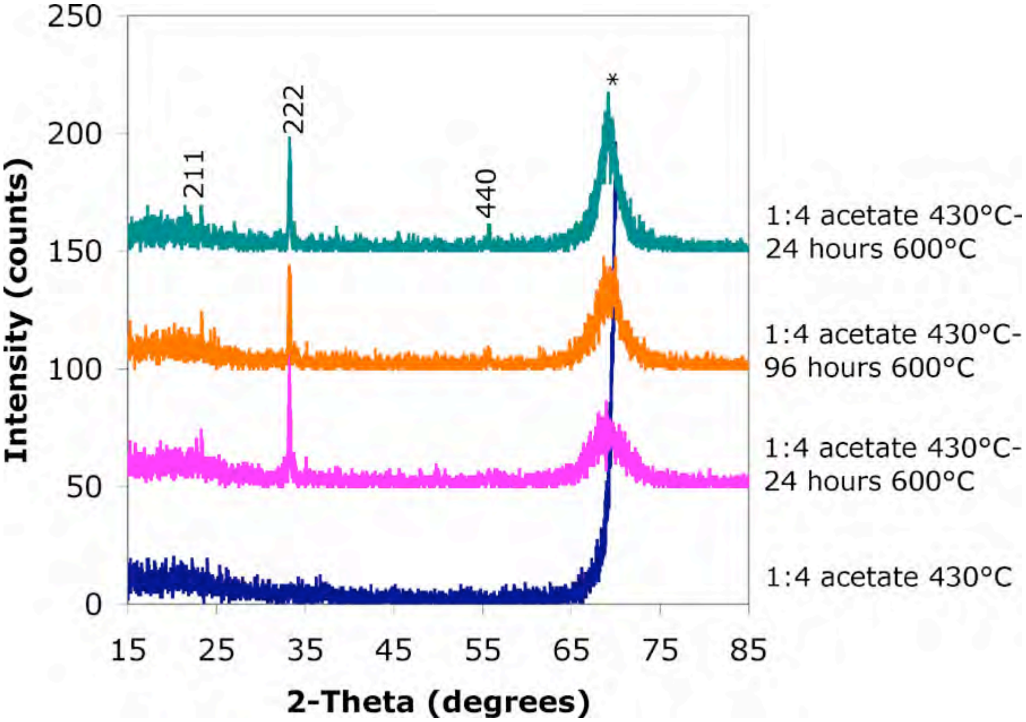

Figure 4.53: XRD patterns of a 1:4 acetate film RTA'd at 430°C and subjected to a series of heat treatments at 600°C for 24, 96, and 192 hours in air. Indexed peaks refer to the bixbyite phase and the one with an "*" is from the substrate.

No sign of the ilmenite phase was present, which should be the second phase present according to the phase diagram. As proven, ilmenite will form at lower temperatures during longer heat treatments. After the other heat treatments, the main bixbyite peak [222-as labeled in the Figure 4.53] at 33°2θ appears to decrease in intensity. This suggests that the bixbyite phase is slowly disappearing as the spinel phase forms.

However, in order for it to completely disappear, a higher temperature is required. According to the bulk phase diagram, a minimum temperature of 850°C is needed to crystallize spinel.

The 1:1.65 acetate sample shows spinel peaks after the first anneal at 630°C. After the first soak for 24 hours, the initial spinel peaks grow and sharpen as shown in Figure 4.54. As it is held at 600°C for longer times, the intensity of the spinel peaks remain relatively constant.

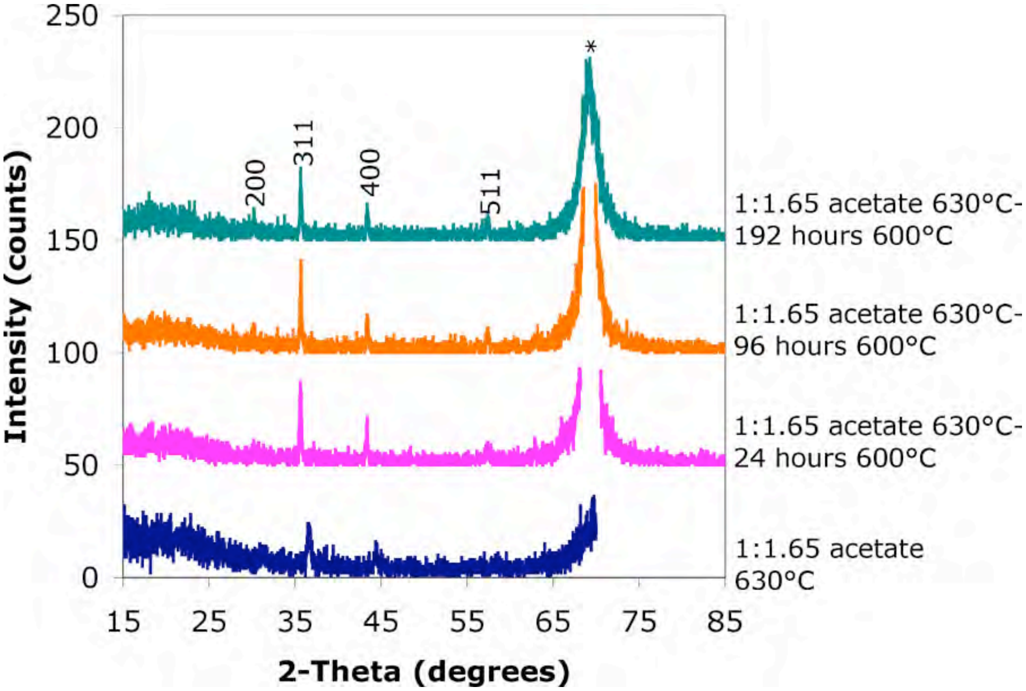

Figure 4.54: XRD patterns of 1:1.65 acetate film annealed at 630°C, subjected to a series of soaks at 600°C for 24, 96, and 192 hours in air. Indexed peaks refer to the spinel phase and the one with an “*” is from the substrate.

The 1:9 acetate sample crystallized the bixbyite phase at 630°C as illustrated in Figure 4.55.

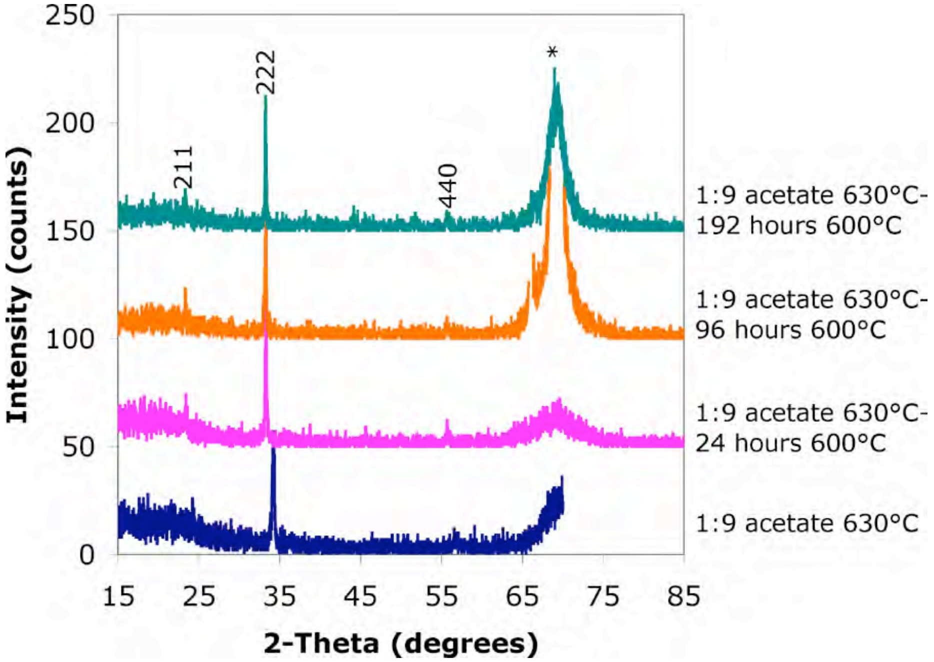

Figure 4.55: XRD patterns of Ni:Mn 1:9 acetate film annealed at 630°C, subjected to a series of soaks at 600°C for 24, 96, and 192 hours in air. Indexed peaks refer to the bixbyite phase and the one with an "*" is from the substrate.

As the sample was heat treated for long hours, the peak intensities did not show much change. This suggests that the film is quite stable.

4.4.4 Annealing of Films in Air at 300°C For Long Times

Nickel manganite films have been shown to crystallize in the cubic spinel phase at 400°C in argon. It has been reported previously, that it is possible to form cubic spinel *powder* as low as 300°C in air [38]. Thus, attempts were made to prepare films at 300°C. A set of pyrolyzed eight layer films were heat treated for up to 127.5 hours at 300°C in air. During this period of time, no onset of crystallization was observed by XRD before 100 hours as displayed in Figure 4.56.

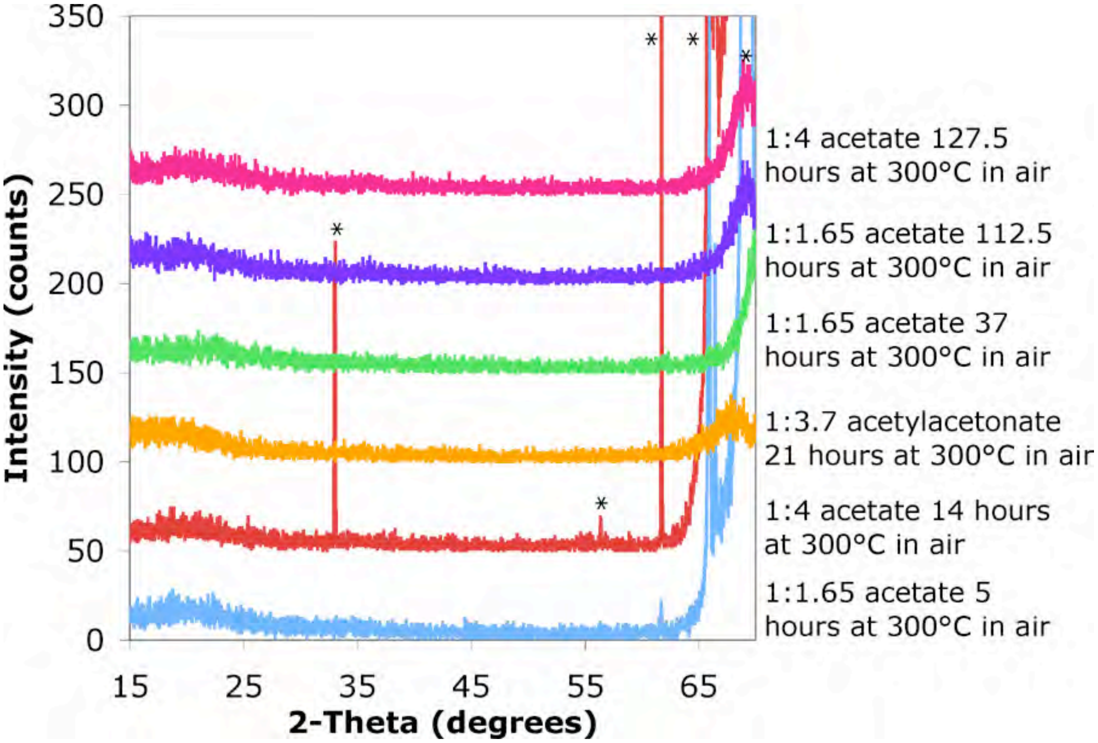

Figure 4.56: XRD patterns for the Ni:Mn 1:1.65 acetate film, 1:4 acetate film, 1:3.7 acetylacetonate film after heat treatments at 300°C in ambient air for 5, 14, 21, 37, 112.5 and 127.5 hours. Peaks marked with an "*" are from the substrate.

After 100 hours, very broad, weak peaks can be seen to begin forming. Further characterization, such as TEM, should be performed before drawing any conclusions in structure. The 1:1.65 and 1:4 films annealed for 112.5 and 127.5 hours are shown in Figure 4.57 with the two peaks labeled.

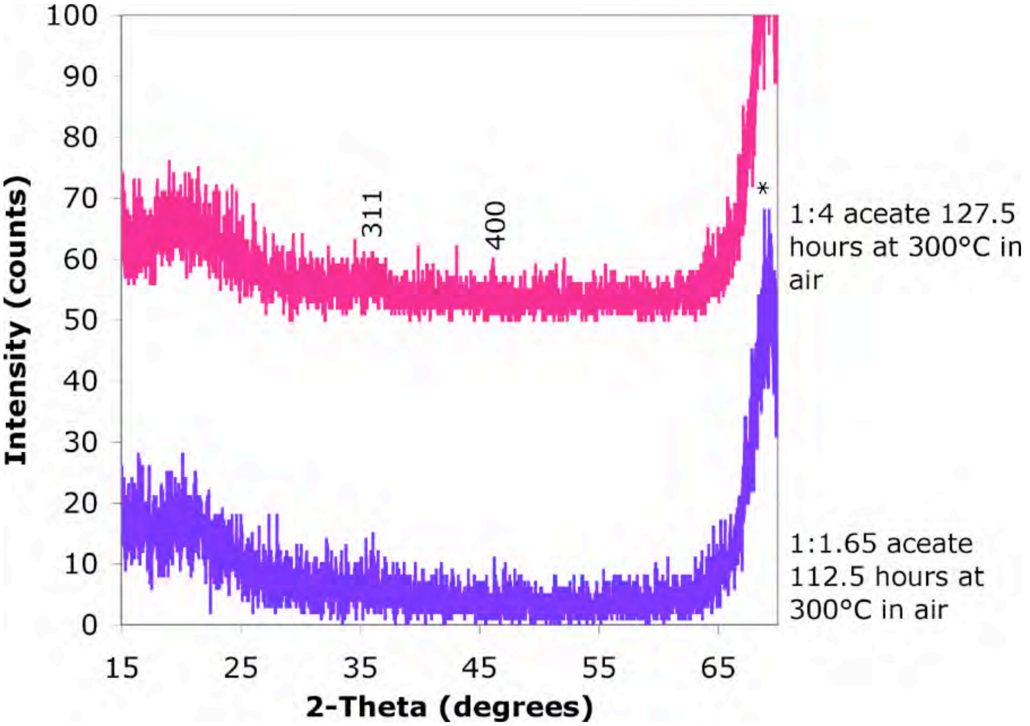

Figure 4.57: XRD patterns of Ni:Mn 1:1.65 acetate film annealed at 300°C in air for 112.5 hours and 1:4 acetate film annealed for 127.5 hours. Indexed peaks correspond to a cubic spinel phase and the one marked with an "*" is from the substrate.

The average TCR was measured after 37 hours, 112.5 hours, and 127.5 hours. The values are shown in Table 4.10.

Table 4.10: Average TCR values found over a temperature range between 295 K and 373 K for films annealed at 300°C in air: values were measured within a 90% confidence limit of ± 0.02 %/°C

Sample	**TCR (%/°C)**		
	37 hours	**112.5 hours**	**127.5 hours**
1:1 acetate	-3.98	-4.00	-4.27
1:1.65 acetate	-3.45	-4.03	-3.84
1:4 acetate	-4.07	-4.19	-4.09
1:3.7 acetylacetonate	-4.01	-4.33	-4.30

These 300°C annealed films show good electrical stability after long heat treatments. It is assumed that though these films may show good electrical stability, they may not have reached full density. SEM results show a film that has a thickness of about 290nm, which is almost double that of a film annealed at higher temperatures.

4.5 Spin Spray Results

Spin spray thermistor samples were synthesized using the apparatus from Kitano Seiki designed by Professor Manasori Abe. Spinel ferrite films hundreds of nm thick were grown at 90°C by this method. Figure 4.58 shows the XRD pattern for one of the $Fe_{3-x}O_4$ films.

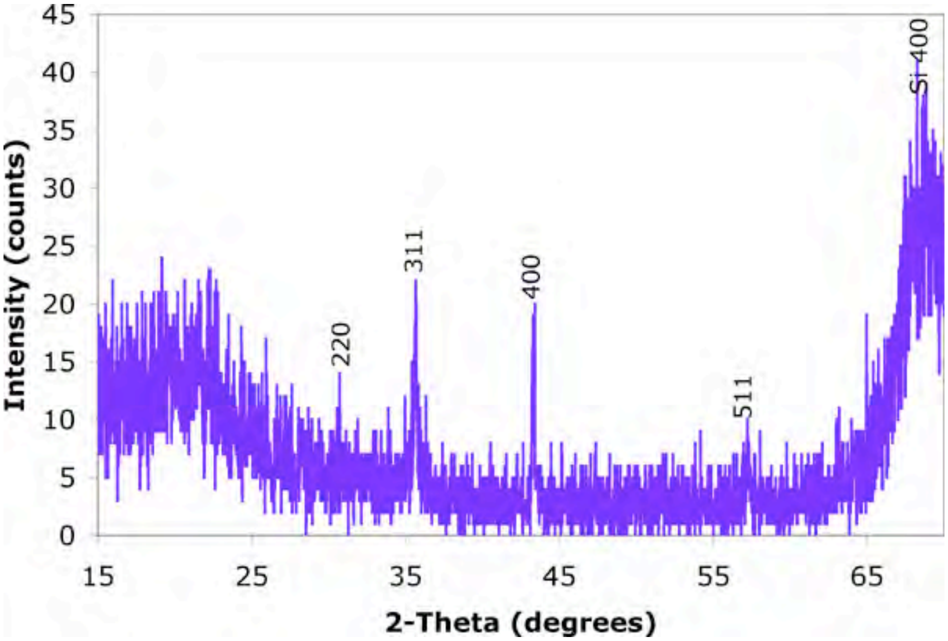

Figure 4.58: XRD pattern of a $Fe_{3-x}O_4$ ferrite spinel thin film grown by the spin spray process using a flow rate of 1.5 L/hr and was deposited for 46 minutes

It was found that changing the flow rate of solution from 0.6 and 3L/hr does not change the growth rate of the film substantially as shown in Table 4.11.

Table 4.11 Growth rates of films grown using various solution flow rates during spin spray deposition with a standard deviation of ± 0.3 Å/rotation

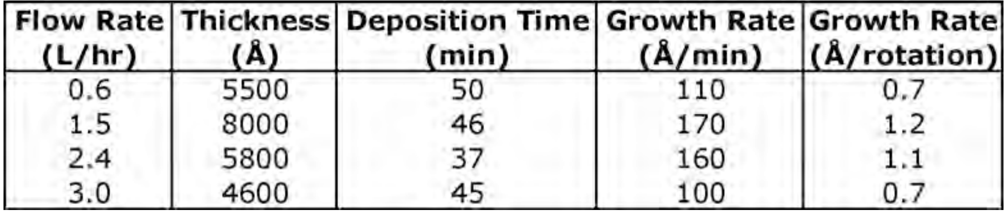

Flow Rate (L/hr)	Thickness (Å)	Deposition Time (min)	Growth Rate (Å/min)	Growth Rate (Å/rotation)
0.6	5500	50	110	0.7
1.5	8000	46	170	1.2
2.4	5800	37	160	1.1
3.0	4600	45	100	0.7

Error on the thicknesses and therefore on the growth rates is due to the fact that the film thickness varied by as much as 1000 Å across a film. If it is assumed that the film deposition is uniform (e.g. that it occurs in a layer-by-layer fashion), then a fraction of a monolayer of film is grown with each rotation of the substrate.

Other parameters of the deposition that were adjusted include the distance between the nozzle and the substrate, the substrate temperature, and the amount of oxidizer. It was found that the distance between the nozzle and the substrate affected the table (and hence the substrate) temperature. The closer the nozzle, the smaller the effective volume within the deposition chamber, the higher a temperature the system was able to maintain. This was found to be a more effective means of controlling the system temperature than was the equipment the set temperature (90°C to 120°C). For additional flexibility, it might be interesting in the future to consider pre-heating the solutions.

The oxidizer concentration was varied from 0.012 moles/L to 0.046 moles/L. Increase in the oxidizer concentration caused the resulting film to adhere poorly to the substrate and flake off. Therefore, for subsequent deposition, a concentration of 0.012 M was employed.

It has been reported in the literature that it is possible to perform spin-spray deposition from a single solution containing both the oxidizer and the cation source [94]. Attempts to reproduce this work ultimately led to solution precipitation. Thus, while films could be deposited in the short time before precipitation occurred, this was not regarded as a stable process. The optimized deposition procedures are given in Table 2.5.

Preliminary TCR measurements of the $Fe_{3-x}O_4$ spin spray films show lnR vs T curves with two different slopes. The break in the curve tells that the conduction mechanism is changing at a certain temperature. At lower temperatures the TCR values is lower than at higher temperatures because only thermal activation of the mobility of the charge carriers is causing conduction. At higher temperatures the slope is steeper, giving a higher TCR value because now conduction is influenced both by thermal activation of mobility and by the creation of charge carriers. Figure 4.59 shows the break in the curve with the two different slopes representing the two TCR values associated with each type of conduction.

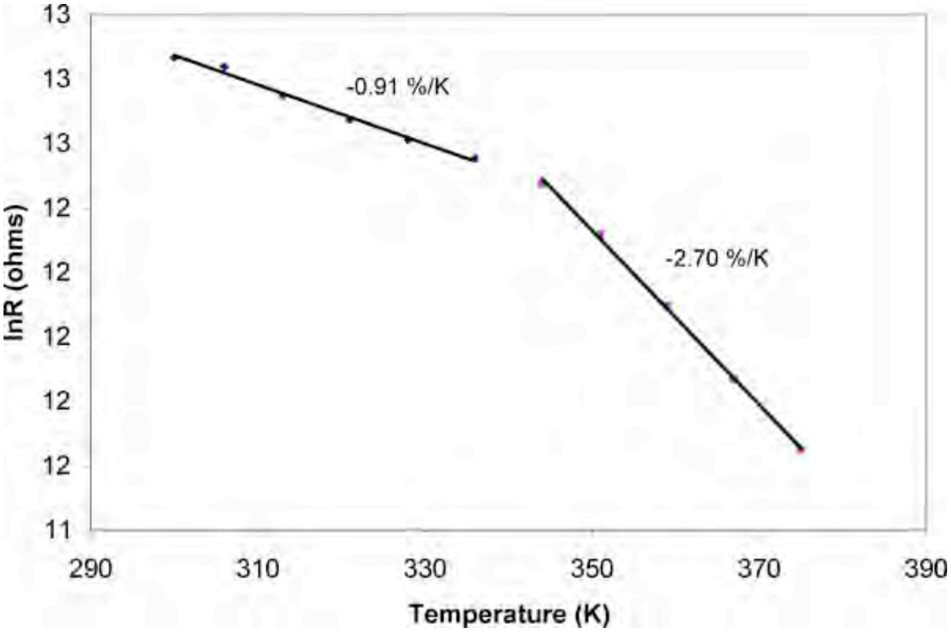

Figure 4.59: Resistance as a function of temperature for a $Fe_{3-x}O_4$ spinel film grown by spin spray

Figure 4.60 shows a SEM image of a cross section of the film. The microstructure of the $Fe_{3-x}O_4$ spin spray film appears to be columnar.

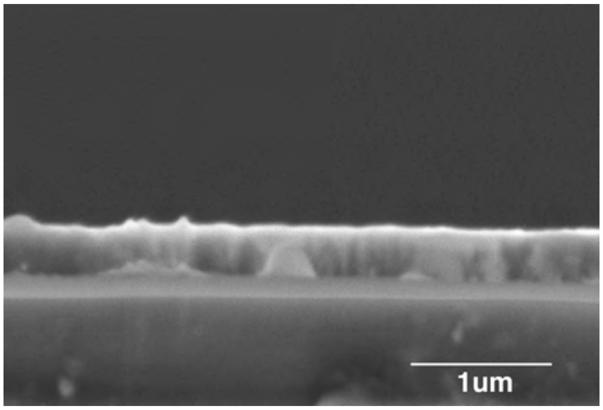

Figure 4.60: SEM image of the cross section of a ferrite spinel spin spray film

Chapter 5

CONCLUSIONS AND FUTURE WORK

5.1 Conclusions

Nickel manganite thin films have been explored for use in uncooled resistive bolometer applications. Films with Ni:Mn ratios ranging from 6:1 to 1:9 were prepared by chemical solution deposition, and were heat-treated at temperatures between 300°C and 1030°C. It was found that the spinel phase could be crystallized in two different regimes: in the thermodynamically stable phase for processing temperatures above 600°C, and as a metastable phase when films were processed around 400°C in a reducing ambient.

The engineering side of this project was to determine whether the processing window for nickel manganite films would enable them to be used for infrared detector arrays. This necessitates that the material must be processed at temperatures low enough to be compatible with the CMOS process, exhibit high TCR coupled with low noise to provide sensitivity to the detector, and show excellent property stability over a wide range of conditions. This work has shown that spinel nickel manganite thin films can be processed at 400°C, maintain stability, and still have a TCR above -3 %/K. The compositions showing TCR values between -3.8 %/K and -4.1 %/K include 1:4, 1:3.7, 1:2, 1:1.65, and 1:1.

It was found that annealing thin films in argon at 400°C for five hours produces crystalline spinel films with good stability in the electrical properties. In particular, Ni:Mn 1:4 acetate films aged at 150°C for over 500 hours showed an increase in resistance of only 6.5%. There was no significant change in TCR (-3.73 ± 0.09 %/K). This particular composition shows excellent promise for surviving the fabrication and packaging procedures required to make a pixel array. The resistivity of the five compositions annealed at 400°C is about an order of magnitude larger than films annealed at higher temperatures (10000 Ωcm+).

Films annealed at 300°C do not show the onset of crystallization until after 100 hours, although reasonable stability (± 0.3 %/K) in the properties was obtained after 30 hours of annealing at 300°C in Ar. The compositions tested include, 1:4, 1:3.7, 1:1.65, and 1:1. TCR values of these films ranged from -3.5 %/K to -4.3 %/K.

Films annealed over 630°C also show excellent structural and property stability when subjected to harsh heat treatments in different atmospheric conditions (air and N_2). Prolonged annealing of such films only leads to an improvement in crystallinity with time. Films of the 1:3.7 composition annealed at 630°C show the spinel structure and when aged at 600°C in air or N_2 for 21 hours show an average TCR value of -3.67 %/K with a standard deviation of ± 0.06 %/K.

Thin films annealed within the high temperature spinel region of the phase diagram show similar properties to those of bulk materials. In particular, TCR values between -3 %/K and -4.5 %/K with resistivities in the 1000 Ωcm range were obtained. The obtained TCR was not a function of the film thickness.

The TCR values, activation energies, and resistivities are correlated. Higher TCR films show higher resistivity and activation energies. This is a common trend seen in thermistor materials [4].

The experimental lattice parameters of the CSD films were too small to account for via the inversion parameter alone. It can be concluded that the films synthesized between 930°C and 1030°C are likely to be cation deficient.

The decomposition of the spinel phase into a rocksalt structure often occurs during the process of bulk nickel manganite thermistors. It has been concluded that because it is possible to densify the films *completely within the spinel phase field* (unlike bulk ceramics, where higher temperatures often lead to decomposition), thin films with the correct composition should be inherently more stable. In contrast, films processed in a phase region where the rocksalt structure, NiO, and spinel should coexist shows inhomogeneity in film composition indicating the presence of two phases. It is suggested that the NiO phase cannot be detected using XRD either because the NiO lattice is coherent with that of the spinel phase, and or because of the extremely fine size of the NiO crystallites (on the order of 10s of nanometers).

The pyrolysis procedures used to prepare thin films can influence phase formation. If organics remain in the film after pyrolysis, a low local pO_2 above the film prohibits the formation of thermodynamically stable (air environment) phases. A metastable spinel phase is favored in reducing atmospheres. Longer, multistep pyrolysis procedures are more likely to eliminate the organics within the film, leading to a thermodynamically stable assemblage of phases. Using rapid pyrolysis procedures allows a small amount of organics to remain, which promoted the formation of single-phase spinel films.

It was found that the morphology of nickel manganite films is columnar for films from both acetate-based films and acetylacetonate solutions. While films processed at elevated temperatures had high densities, those prepared using only low temperature anneals (e.g. 300°C) were substantially thicker, suggesting incomplete densification.

As predicted based on the phase diagram, films with very high Mn concentrations processed under oxidizing conditions showed the bixbyite structure. Such films showed lower TCR and resistivities compared to spinel films. Weiner's mixing rule for the conductivity of composite conductors did not predict the volume fraction of each phase in bixbyite-spinel composite films.

Initial experiments on spin spray deposition of ferrite spinels demonstrated that this process is promising for processing materials at 90°C. The resulting crystalline film shows columnar morphology and exhibits a TCR that changes around 340°C due to a change in the conduction mechanism.

5.2 Future Work

The processing and characterization of nickel manganite thin films has been explored in this thesis. Much has been learned about how processing effects the material properties, but many questions remain. This section describes experiments that would provide knowledge on this system and answer questions that have arisen from the current research. The work up to this point has proved that the nickel manganite materials are promising potential candidates for uncooled microbolometer applications. The future work discussed here will focus both on the engineering aspect of the project and the science of this materials system.

The question as to why NiO can be detected by TEM, but not by XRD analysis needs to be answered. It was hypothesized that either the NiO phase is coherently strained to the spinel phase or the NiO crystallite size is too small to be detected by X-rays. As a first approach to estimating this, the NiO would be treated as a film. The critical thickness of the film required for coherency could then be estimated using the Matthews-Blakeslee criterion. Dislocations contain excess energy while releasing stored energy from strain [95]. If there is more energy in the dislocation then is released, the dislocation will not form [95]. Thinner films with smaller burger's vectors are more likely to have dislocations form, hence more likely to be coherently strained [95].

TEM analysis was performed on the Ni:Mn 1:1 acetate films in order to identify the presence of the NiO, rock salt phase. The 1:1.65 acetate films fall within the same phase region where spinel and NiO coexist. XRD only shows the spinel phase present for both compositions. It would be interesting to also perform TEM on the 1:1.65 film to see if TEM is necessary to detect second phases.

It was also demonstrated that high TCR values were correlated with a high resistivity. In the bulk thermistor material, dopants are added in order to adjust the electrical properties. Both cobalt and copper have been shown to drop resistivity values, as well as TCR [6]. Studying the effects of these dopants in the thin films can help to better understand how to engineer properties. Also the annealing atmosphere has been reported to affect resistivity [33]. Inert atmospheres crystallize materials with higher resistivities, as shown in this thesis [33]. Further investigation on processing-property relationship should be studied to develop optimum parameters to engineer the desired thermistor material.

The bixbyite phase of the nickel manganite system demonstrates lower TCR and lower resistivities compared to the spinel phase. Composite films might be useful in achieving a compromise between the total resistivity and TCR. Development of a more appropriate mixing rule would be useful in designing a phase assemblage. If it is found that the electrical resistivity cannot be lowered sufficiently using bixbyite, then it might be interesting to examine composition films in which metal particles (e.g. Ag) were dispersed.

Another factor that should be investigated is the electrical noise in nickel manganite films. The noise of a material could be affected by microstructure, processing conditions (temperature and environment), and composition. It is necessary for application in a microbolometer to determine if films processed at low temperature will show similar noise values to films annealed at higher temperatures.

In order for the nickel manganite spinels to be used in a microbolometer application, a low processing temperature is necessary. Stability tests on the films annealed at 400°C and below will give critical information on how the material changes. Heat treatments at 400°C in both air and reducing atmospheres for long times should be performed. It is likely that the films annealed at 300°C for over 100 hours will undergo a phase change when heat-treated at a higher temperature than 400°C. Determination of an optimum anneal time and temperature to produce a stable film at the lowest possible temperature is needed.

TEM analysis on the low temperature annealed films can test for phase homogeneity and grain size. The films show weak crystallinity and therefore will probably have a small crystallite size. The literature indicates that low temperature spinel is a defect spinel. Rietveld refinement should be used to analyze the site occupancy of the defect spinel structure in both the high and low temperature annealed films. XPS (X-ray photoelectron spectroscopy) can also be utilized to find out the oxidation states of the cations in the spinel structure.

The knowledge gained from studying this system can be implemented to design a processing route that is more compatible with the existing microfabrication process, sputter deposition. CSD processing routes are used in order to study a wide range of compositions quickly and inexpensively. From past experience the understanding gained from this work can be translated into another deposition technique, such as sputtering. The low temperature processing of a single-phase spinel in an inert atmosphere should be achievable if a sputter technique is implemented.

The occurrence of oriented films is unexplained. The majority of the films in this thesis exhibited peak intensities similar to those of bulk materials. The Ni:Mn 1:2 acetylacetonate films were an exception. Figure 6.1 shows acetylacetonate-based films heat-treated between 530°C and 930°C.

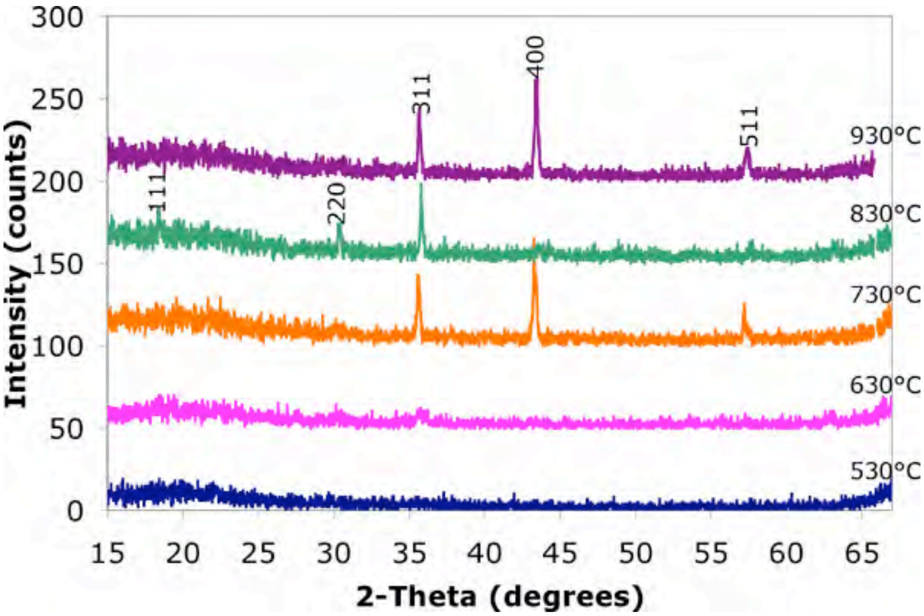

Figure 6.1: XRD patterns of films made from 1:2 acetylacetonate solutions and heat-treated at temperatures ranging from 530°C to 930°C for one minute in the RTA. The indexed diffraction peaks correspond to a cubic spinel.

Some films showed a comparatively stronger 400 spinel peak than would be characteristic of a random ceramic. This preferred orientation clearly cannot arise from any sort of structure match with the substrates, since the SiO_2 was amorphous. The origin of the preferred orientation is not known, but could possibly be influenced by the chemical composition, the degree of inversion, or the separation distance between dopants (nickel in this case) [96]. These three factors contribute to variation of the overall surface free energy of the material, which influences the equilibrium grain morphology [97]. When and how this occurs remains a question. This set of films should be remade and characterized to determine if it is a reoccurring trend in this particular composition or if something occurred during the processing of these films. The variable that caused the anisotropy needs to be found.

Optimization of the spin spray deposition process should be pursued. The next major step is to try to incorporate different material systems, especially the nickel manganites, into the process. Of particular interest in the long term would be development of an improved understanding of the mechanisms governing the process, as well as means of designing in compositional flexibility. Either real-time analysis (e.g. with spectroscopic ellipsometry) or ex-situ characterization (e.g. with AFM or SEM) of the deposition could determine if the film is growing in a layer-by-layer growth mode or in clusters. Understanding the effect of pH during the reaction on the deposition process will help in ascertaining the compositional flexibility achievable using this deposition method. Likewise, the effect of surface termination on spin spray deposition should be investigated for a variety of substrates.

REFERENCES

[1] J. Caniou. Passive Infrared Detection Theory & Applications. Dordrecht, The Netherlands: Kluwer Academic Publishers, 1999.

[2] X.-M. Liu, H.-J. Fang, and L.-T. Liu. "Study on new structure uncooled a-Si microbolometer for infrared detection," Microelectronics Journal. 38 (2007): 735–739.

[3] P. Umadevi and C. L. Nagendra. "Preparation and characterization of transition metal oxide micro-thermistors and their application to immersed thermistor bolometer infrared detectors," Sensors and Actuators A. 96 (2002): 114-124.

[4] E. D. Macklen. Thermistors. Scotland: Electrochemical Publications LTD, 1979.

[5] R. J. Choudhary, A. S. Ogale, S. R. Shinde, S. Hullavarad, S. B. Ogale, and T. Venkatesan. "Evaluation of manganite films on silicon for uncooled bolometric applications," Applied Physics Letters. 84 (2004): 3846-3848.

[6] A. J. Moulson and J. M. Herbert. Electroceramics 2nd Edition. West Sussex, England: John Wiley and Sons Ltd., 2003.

[7] D. Gutierrez, O. Peña, P. Duran, and C. Moure. "Crystal structure, electrical conductivity, and Seebeck coefficient of $Y(Mn,Ni)O_3$ solid solution," Journal of the European Ceramic Society. 22 (2002): 567-572.

[8] A. Veres, J. G. Noudem, S. Fourrez, and G. Bailleul. "The influence of iron substitution to manganese on the physical properties of $YMnO_3$," Solid State Sciences. 8 (2006): 137-141.

[9] A. Rogalski. Infrared Photon Detectors. Bellingham, Washington: SPIE Optical Engineering Press, 1995.

[10] R. J. Keyes, ed. Topics in Applied Physics-Optical and IR Detectors. Vol. 19. New York: Springer-Verlag, 1980.

[11] R. De Waard and E. M. Wormser. "Description and properties of various thermal detectors," Proceedings of the IRE. Sept (1959): paper 4.1.3.

[12] P. Guggilla, A. K. Batraa, J. R. Currieb, M. D. Aggarwala, M. A. Alimc, and R. B. Lala. "Pyroelectric ceramics for infrared detection applications," Materials Letters. 60 (2006): 1937-1942.

[13] Paul W. Kruse. Uncooled Thermal Imaging-Arrays, Systems, and Applications. Bellingham, WA: SPIE Press, 2001.

[14] A. J. Syllaios, T. R. Schimert, R. W. Gooch, W. L. McCardel, B. A. Ritchey, J. H. Tregilgas. “Amorphous Silicon Microbolometer Technology,” Mat. Res. Soc. Symp. Proc. 609 (2000): A14.4.1-A14.4.6.

[15] A. R. Jha. Infrared Technology Applications to Electro-optics, Photonic Devices, Sensors. New York: John Wiley and Sons Inc., 2000.

[16] MICRO-EPSILON <www.micro-epsilon.us/>.

[17] R. P. Turner. ABC’s of Thermistors. Indianapolis, Indiana: Howard W. Sams & Co. Inc., 1970.

[18] R. C. Buchanan. Ceramic Materials for Electronics 3rd Ed. New York: Marcel Dekker, 2004.

[19] A. R. West. Basic Solid State Chemistry 2nd Ed. West Sussex, England: John Wiley and Sons, Ltd., 1999.

[20] G. D. C. Csete de Gyorgyfalva, A. N. Nolte, and I. M. Reaney. “Correlation between microstructure and conductance in NTC thermistors produced from oxide powders,” Journal of the European Ceramic Society. 19 (1999): 857-860.

[21] B. Gillot, R. Legros, R. Metz, and A. Rousset. “Electrical conductivity of copper and nickel manganites in relation with the simultaneous presence of Mn^{3+} and Mn^{4+} ions on octahedral sites of the spinel structure,” Solid State Ionics. 51 (1992): 7-9.

[22] E.G. Larson, R.J. Arnott, and D.G. Wickham. “Preparation, semiconduction and low-temperature magnetization of the system $Ni_{1-x}Mn_{2+x}O_4$,” Journal of Physics and Chemistry of Solids 23 (1962): 1771-1781.

[23] N. M. Tallan, ed. Electrical Conductivity in Ceramics and Glass Part A. New York: Marcel Dekker, Inc., 1974.

[24] C. Kittel. Introduction to Solid State Physics 7th ed. New York: John Wiley & Sons, Inc., 1996.

[25] J. B. Goodenough and A. L. Loeb. “Theory of ionic ordering, crystal distortion, and magnetic exchange due to covalent forces in spinels,” Physical Review. 98

[26] H. Bottger. Hopping Conduction in Solids. Berlin: Akademie-Verlag, 1985.

[27] S. Fritsch, J. Sarrias, M. Brieu, J. J. Couderc, J. L. Baudour, E. Snoeck, A. Rousset. "Correlation between structure, the microstructure, and the electrical properties of nickel manganite negative temperature coefficient (NTC) thermistors," Solid State Ionics. 109 (1998): 229-237.

[28] R. Schmidt, A. Basu, and A.W. Brinkman. "Production of NTCR thermistor devices based on $NiMn_2O_{4+\delta}$," Journal of the European Ceramic Society. 24 (2004): 1233-1236.

[29] R. Dannenberg, S. Baliga, R. J. Gambino, A. H. King, and A. P. Doctor. "Resistivity, thermopower and the correlation to infrared active vibrations of $Mn_{1.56}Co_{0.96}Ni_{0.48}O_4$ spinel films sputtered in an oxygen partial pressure series," Journal of Applied Physics. 86 (1999): 514-523.

[30] E. Elbadraoui, J.L. Baudour, F. Bouree, B. Gillot, S. Fritsch, and A. Rousset. "Cation distribution and mechanism of electrical conduction in nickel-copper manganite spinels," Solid State Ionics. 93 (1997): 219-225.

[31] D. A. Kukuruznyak, S. W. Han, M. H. Lee, K. A. Omland, M. C. Gregg, E. A. Stern, and F. S. Ohuchi. "Controlled coordination and oxidation states of copper and manganese cations in complex nickel-copper-cobalt-manganese oxide thin films," J. Vac. Sci. Technolo. A. 19 (2001): 1023-1928.

[32] A. Veres, J. G. Noudem, O. Perez, S. Fourrez, and G. Bailleul. "Manganese based spinel-like ceramics with NTC-type thermistor behavior," Solid State Ionics. 178 (2007): 423-428.

[33] P. Fau, J. P. Bonino, J. J. Demai, and A. Rousset. "Thin films of nickel manganese oxide for NTC thermistor applications," Applied Surface Science. 65/66 (1993): 319-324.

[34] R. Metz. "Electrical properties of N.T.C. thermistors made of manganite ceramics of general spinel structure: $Mn_{3-x-x'}M_xN_{x'}O_4$ (0<x+x'<1;M and N being Ni, Co or Cu). Aging phenomenon study," Journal of Materials Science. 35 (2000): 4705-4711.

[35] D. G. Wickham. "Solid-Phase Equilibria in the System NiO-Mn_2O_3-O_2," J. Inorg. Nucl. Chem. 26 (1964): 1369-1377.

[36] X. Tang, A. Manthiram, and J. Goodenough. "$NiMn_2O_4$ Revisited," Journal of the Less-Common Metals. 156 (1989): 357-368.

[37] C. Chanel, S. Fritsch, C. Drouet, A. Rousset, M. Marinez Sarrion, L. Mestres, and M. Morales. "Synthesis, thermogravimetric and high temperature X-ray diffraction analyses of zinc-substituted nickel manganites," Materials Research Bulletin. 35 (2000): 431-439.

[38] J. deVidales, R. Rojas, E. Vila, and O. Garcia-Martinez. “Low temperature synthesis of tetragonal nickel manganite spinels: thermal behavior and reactivity,” Materials Research Bulletin. 29 (1994): 1163-1173.

[39] E. Zhecheva and R. Stoyanova. “Lithium doping of cobalt-nickel spinel oxides at low temperature,” Materials Science Forum. 152-153 (1994): 323-326.

[40] R. Schmidt, A. Basu, and A.W. Brinkman. “Small polaron hopping in spinel manganates,” Physical Review B. 72 (2005): 115101-1 – 115101-9.

[41] B. Boucher, R. Buhl, and M. Perrin. “Etude cristallographique du manganite spinelle cubique $NiMn_2O_4$ par diffraction de neutrons,” Acta Crystallographica Section B – Structural Crystallography and Chrystal Chemistry. B 25 (1969): 2326-2333.

[42] A. Feltz, J. Topfer, and F. Schirrmeister. “Conductivity data and preparation routes for $NiMn_2O_4$ thermistor ceramics,” Journal of the European Ceramic Society. 9 (1992): 187-191.

[43] M. Pernet, J. Joubert, and B. Ferrand. “Etude par diffraction neutronique de l’ilmenite ferrimagnetique $NiMnO_3$,” Solid State Communications. 16 (1975): 503-308.

[44] A. Feltz and J. Topfer. “Investigations on electronically conducting oxide systems XXVI. Preparation and properties of Ni_6MnO_8 and $NiMnO_{3-\delta}$ (δ~0.02),” Journal of Alloys and Compounds. 196 (1993): 75-79.

[45] T. Swoboda, R. Toole, and J. Vaughan. “Net Magnetic Compounds of the Ilmenite Type Structure,” Journal of Physics and Chemisty of Solids. 5 (1958): 293-298.

[46] D. Mehandjiev, E. Zhecheva, G. Ivanov, and R. Ioncheva. “Preparation and catalytic activity of nickel-manganese oxide catalysts with an ilmenite-type structure in the reactions of complete oxidation of hydrocarbons,” Applied Catalysis A. 167 (1998): 277-282.

[47] D. Mehandjiev, A. Naydenov, and G. Ivanov. “Ozone decomposition, benzene and CO oxidation over $NiMnO_3$-ilmenite and $NiMn_2O_4$-spinel catalysts,” Applied Catalysis A. 206 (2001): 13-18.

[48] P. Porta and G. Minelli. “Structural, magnetic, and optical investigation of Ni_6MnO_8,” Journal of Solid State Chemistry. 92 (1991): 202-207.

[49] S. Geller. “Structures of α-Mn_2O_3, $(Mn_{0.983}Fe_{0.017})_2O_3$ and $(Mn_{0.37}Fe_{0.63})_2O_3$ and Relation to Magnetic Ordering,” Acta Crystallographica. B27 (1971): 821-828.

[50] D. Saha, A. Sharma, A. Sen, and H. Maiti. “Preparation of bixbyite phase $(Mn_xFe_{1-x})_2O_3$ for NTC thermistor applications,” Materials Letters. 55 (2002): 403-406.

[51] S. Geller and G. Espinosa. “Magnetic and Crystallographic Transitions in Sc^{3+}, Cr^{3+}, and Ga^{3+} Substituted Mn_2O_3,” Physical Review B. 1 (1971): 3763-3769.

[52] M. Regulski, R. Przenioslo, I. Sosnowska, D. Hohlwein, and R. Schneider. “Neutron diffraction study of the magnetic structure of α-Mn_2O_3,” Journal of Alloys and Compounds. 362 (2004): 236-240.

[53] C. Xu, K. Miyazaki, and T. Watanabe. “Humidity sensors using manganese oxides,” Sensors and Actuators B. 46 (1998): 87-96.

[54] G. D. C. Csete de Gyorgyfalva and I. M. Reaney. “Decomposition of $NiMn_2O_4$ spinel: an NTC thermistor material,” Journal of the European Ceramic Society. 21 (2001): 2145-2148.

[55] G. Ashcroft, I. Terry, and R. Gover. “Study of the preparation conditions for $NiMn_2O_4$ grown from hydroxide precursors,” Journal of the European Ceramic Society. 26 (2006): 901-908.

[56] P. Castelan, B. Ai, A. Loubiere, A. Rousset, and R. Legros. “Ageing study of NTC thermistors by thermopower measurements,” Sensors and Actuators A. 33 (1992): 119-122.

[57] O. Shpotyuk, M. Vakiv, O. Mrooz, I. Hadzaman, J. Plewa, H. Uphoff, and H. Altenburg. “Aging phenomena in $Cu_{0.1}Ni_{0.8}Co_{0.2}Mn_{1.9}O_4$ NTC ceramics,” Key Engineering Materials. 206-213 (2002): 1317-1320.

[58] D. A. Kukuruznyak, J. G. Moyer, and F. S. Ohuchi. “Improved aging characteristics of NTC thermistor thin films fabricated by a hybrid sol-gel-MOD process,” J. Am. Ceram. Soc. 89 (2006): 189-192.

[59] J.-F. Gao, D.-L. Fang, Z.-B. Wang, P.-H. Yang, and C.-S. Chen. “Preparation and electrical properties of copper-nickel manganite ceramic derived from mixed oxalate,” Sensors and Actuators A. 135 (2007): 472-475.

[60] V. Balitska, B. Butkievich, O. Shpotyuk, and M. Vakiv. “On the analytical description of aging kinetics in ceramic manganite-based NTC thermistors,” Microelectronics Reliability. 42 (2002): 2003-2007.

[61] W. Groen, C. Metzmacher, P. Huppertz, and S. Schuurman. “Aging of NTC ceramics in the system Mn-Ni-Fe-O,” Journal of Electroceramics. 7 (2001): 77-87.

[62] C. Metzmacher, W. Groen, and I. Reaney. “Microstructure and electrical properties of Mn-Ni-In spinels,” Physica Status Solidi a. 181 (2000): 369-386.

[63] M. Vakiv, O. Shpotyuk, V. Balitska, B. Butkiewicz, and L. Shpotyuk. “Aging behavior of electrical resistance in manganite NTC ceramics, “ Journal of the European Ceramic Society. 24 (2004): 1243-1246.

[64] B. Gillot, M. Kharroubi, R. Metz, R. Legros, and A. Rousset. “Electrical properties and cationic distribution in cubic nickel manganite spinels $Ni_xMn_{3+x}O_4$, $0.57<x<1$,” Solid State Ionics. 44 (1991): 275-280.

[65] D. A. Kukuruznyak, S. A. Bulkley, K. A. Omland, F. S. Ohuchi, and M.C. Gregg. “Preparation and properties of thermistor thin-films by metal organic decomposition,” Thin Solid Films. 385 (2001): 89-95.

[66] M. Parlak, T. Hashemi, M. Hogan, and A. Brinkman. “Effect of heat treatment on nickel manganite thin film thermistors deposited by electron beam evaporation,” Thin Solid Films. 345 (1999): 307-311.

[67] H. Kozuka and S. Sakka. Handbook of Sol-Gel Science and Technology: Processing, Characterization, and Applications – Volume 1: Sol-Gel Processing. Norwell, MA: Kluwer Academic Publishers, 2005.

[68] P. Clem. “Solution deposition of $YBa_2Cu_3O_{7-d}$ coated conductors.” Second-Generation HTS Conductors. A. Goyal. Norwell, MA: Kluwer Academic Publishers, 2005. 179-194.

[69] B. Lee and S. Komarneni. Chemical Processing of Ceramics 2nd Ed. Boca Raton, FL: Taylor and Francis, 714-742, 2005.

[70] R. W. Schwartz. “Chemical solution deposition of perovskite thin films," Chem. Mater. 9 (1997): 2325-2340.

[71] K. Knoth, S. Engel, C. Apetrii, M. Falter, B. Schlobach, R. Huhne, S. Oswald, L. Schultz, and B. Holzapfel. “Chemical solution deposition of $YBa_2Cu_3O_{7-X}$ coated conductors.” Current Opinion in Solid State and Materials Science. 10 (2006): 205-216.

[72] J. Livage. “The sol-gel route to advanced materials,” Materials Science Forum. 152-155 (1994): 43-54.

[73] B. I. Lee and E. J. A. Pope, eds. Chemical Processing of Ceramics. New York, New York: Marcel Dekker, Inc., 1994.

[74] J. Reed. Principles in Ceramics Processing 2nd Ed. New York: John Wiley and Sons, Inc., 1995.

[75] "Advanced ceramics: chemical precursors and processing." Encyclopedia Britannica. 15th ed. 2002.

[76] P. M. Pimentel, A. E. Martinelli, D. M. A. Melo, A. M. G. Pedrosa, J. D. Cunha, and C. N. S. Junior. “Pechini synthesis and microstructure of nickel-doped copper chromites,” Materials Research. 8 (2005): 221-224.

[77] M. Abe. “A soft solution processing technique for preparing ferrite films and their applications,” MRS Bulletin. (2000): 221-224.

[78] T. H. Hai, H. T. B. Van, T. C. Phong, A. Mansanori. “Spinel ferrite thin-film synthesis by spin-spray ferrite plating,” Physica B. 327 (2003) 194-197.

[79] C. M. Fau, H. S. Hsu, Y. C. Chao, N. Matsushita, and M. Abe. “High-frequency transport properties of spin-spray plated Ni-Zn ferrite thin films,” Journal of Applied Physics. 93 (2003): 7127- 7129.

[80] N. Matsushita, T. Nakamura, and M. Abe. “Spin-sprayed Ni-Zn-Co ferrite films with high μ_r”>100 in extremely wide frequency range 100MHz-1GHz,” Journal of Applied Physics. 93 (2003): 7133-7135.

[81] K. Kondo, T. Chiba, S. Yoshida, S. Okamoto, Y. Shimada, N. Matsushita, and M. Abe. “FMR study on spin-sprayed Ni-Zn-Co films with high permeability usable for GHz noise suppressors,” IEEE Transactions on Magnetics. 41 (2005): 3463-3465.

[82] N. Matshushita, T. Abe, K. Kondo, S. Yoshida, and M. Abe. “Highly resistive Mn-Zn ferrite films prepared from aqueous solution for GHz conducted noise suppressors,” Journal of Applied Physics. 97 (2005): 10G106-1 – 10G106-3.

[83] M. Abe, T. Itoh, Y. Tamaura, M. Gomi. “Ferrite-organic multilayer film for microwave monolithic integrate circuits prepared by ferrite plating based on the spray-spin-coating method,” Journal of Applied Physics. 63 (1988): 3774-3776.

[84] N. Matsushita, C. P. Chong, T. Mizutani, M. Abe. “High-rate low-temperature (90C) deposition of Ni-Zn ferrite films highly permeable in gigahertz range,” IEEE Transactions on Magnetics. 38 (2002): 3156-3158.

[85] J. Goldstein, D. Newbury, D. Joy, C. Lyman, P. Echlin, E. Lifshin, L. Sawyer, and J. Michael. Scanning Electron Microscopy and X-Ray Microanalysis 3rd Edition. New York: Springer Science + Business Media, Inc., 2003.

[86] “Ion Beam Sputtering: Practical Applications to Electron Microscopy,” *Applications Laboratory Report* 91 from South Bay Technologies. 1-5.

[87] O. Gyrdasova, G. Bazuev, V. Krasil'nikov, and V. Sharov. "Synthesis of $NiMnO_3$ ilmenite by thermal decomposition of double oxalates and their hydrazine compounds," Russian Journal of Inorganic Chemistry. 48 (2003): 1310-1315.

[88] M. Sarrion and M. Sanchez. "Preparation and Characterization of Thermistors with Negative Temperature Coefficient, $Ni_xMn_{3-x}O_4$ ($1 \geq x \geq 0.56$), from Formate Precursors," Journal of Materials Chemistry. 3 (1993): 273-277.

[89] D. Emin. "Correlated Small-Polaron Hopping Motion," Physical Review Letters. 25 (1970): 1751-1755.

[90] D. Emin. "Lattice Relaxation and Small-Polaron Hopping Motion," Physical Review B. 4 (1971): 3639-3651.

[91] T. Holstein. "Studies of Polaron Motion Part 1. The Molecular-Crystal Model," Annals of Physics. 281 (2000): 706-724.

[92] D. McLachlan, M. Blaszkiewicz, and R. Newnham. "Electrical resistivity of composites," Journal of the American Ceramics Society. 73 (1990): 2187-2203.

[93] J. Li, N. Yuan, J. Xie. "Annealing characteristics of the vanadium oxide films prepared by modified ion beam enhanced deposition," Applied Surface Science. 243 (2005): 437-442.

[94] J. Miyasaka, M. Tada, M. Abe, and N. Matsushita. "$Fe_3O_{4-\partial}$ films prepared by "one-liquid" spin spray ferrite plating for gigahertz-range noise suppressors," Journal of Applied Physics. 99 (2006): 08M916-1 – 08M916-3.

[95] E. D. Smith. Thin-Film Deposition, Principles and Practices. Boston, Massachusetts: McGraw-Hill, Inc., 1995.

[96] G. Fu, A. Polity, N. Volbers, B. Meyer. "Annealing effects on VO_2 thin films deposited by reactive sputtering," Thin Solid Films. 515 (2006): 2519-2522.

[97] J. Ziolkowski. "The morphological diagram of spinels," Journal of Solid State Chemistry. 121 (1996): 388-393.

APPENDICES

Appendix A: Example Batch Calculations for CSD

Batching calculations for a 30mL solution of a 1:4 ratio mixture:

0.03L * 0.3mole/L * 1/5 * 248.86g/mole = 0.4479g Ni-acetate
0.03L * 0.3mole/L * 4/5 * 245.09g/mole = 1.7647g Mn-acetate

Batching calculations for a 30mL solution of a 1:2 ratio mixture:

0.03L * 0.3mole/L * 1/3 * 248.86g/mole = 0.7466g Ni-acetate
0.03L * 0.3mole/L * 2/3 * 245.09g/mole = 1.4705g Mn-acetate

Appendix B: Electrical Data for Films Made From Acetate Precursors

The table contains electrical data from films made from acetate precursors and annealed for one minute in the RTA in air at temperatures ranging from 430°C to 1030°C. The error from the TCR comes from 90% confidence limits taken from the slopes of the lnR versus T curves. The TCR values are averages over the temperature range from 295 K to 373 K. The resistance and resistivity values are given at 298 K. Error reported with activation energies come from 90% confidence limits that were taken from the slope of the lnR versus 1/T plots. Thicknesses of the films were estimated from SEM micrographs. These films were annealed at temperatures over 700°C. Therefore, the resistivity values are estimates for the lower temperature annealed films. The phases identified come from XRD and TEM analysis. The Ni:Mn is listed as the ideal compositional ratio.

		T	TCR	Error	R_{298K}	E_a	B	Error	Thick	ρ	Phase
Ni	Mn	(°C)	(%/°C)	(%/°C)	(Ω)	(eV)	(K)	(K)	(nm)	(Ωcm)	
6	1.00	430	-3.13	0.09	1.02E+10	0.30	3510	10	150	3800000	amorphous
6	1.00	530	-4.66	0.03	2.59E+10	0.45	5220	10	150	9700000	Ni_6MnO_8
6	1.00	630	-4.89	0.03	2.04E+11	0.47	5460	20	150	77000000	Ni_6MnO_8
6	1.00	730	-4.12	0.02	4.49E+09	0.39	4540	10	150	1700000	Ni_6MnO_8
6	1.00	830	-5.02	0.02	6.59E+10	0.50	5760	20	150	25000000	Ni_6MnO_8
6	1.00	930	-4.27	0.02	1.02E+10	0.40	4670	20	150	3800000	Ni_6MnO_8
6	1.00	1030	-5.35	0.03	2.99E+11	0.52	6060	40	150	110000000	Ni_6MnO_8
1	1.00	430	-4.33	0.02	2.12E+08	0.42	4870	10	150	80000	amorphous
1	1.00	530	-4.19	0.02	1.20E+08	0.40	4590	10	150	45000	spinel
1	1.00	630	-3.71	0.02	1.78E+07	0.35	4070	10	150	6700	spinel
1	1.00	730	-3.51	0.02	8.35E+06	0.33	3860	10	150	3100	spinel+NiO
1	1.00	830	-3.59	0.02	1.36E+07	0.34	3950	10	150	5100	spinel+NiO
1	1.00	930	-3.65	0.02	2.14E+07	0.36	4120	10	150	8000	spinel+NiO
1	1.00	1030	-4.09	0.02	2.91E+08	0.39	4500	10	150	110000	spinel+NiO
1	1.65	430	-4.25	0.01	1.40E+08	0.41	4700	10	150	53000	amorphous
1	1.65	530	-4.03	0.02	4.55E+07	0.38	4430	10	150	17000	spinel
1	1.65	630	-3.98	0.02	3.71E+07	0.38	4410	10	150	14000	spinel
1	1.65	730	-3.12	0.01	1.13E+06	0.29	3420	10	150	420	spinel
1	1.65	830	-3.73	0.02	9.18E+06	0.35	4060	10	150	3400	spinel
1	1.65	930	-2.71	0.02	8.99E+07	0.26	2970	40	150	34000	spinel
1	1.65	1030	-4.20	0.02	1.52E+08	0.40	4600	10	150	57000	spinel
1	2.00	430	-4.10	0.02	4.16E+07	0.40	4640	10	150	16000	amorphous
1	2.00	530	-3.96	0.01	2.29E+07	0.37	4320	10	150	8600	spinel
1	2.00	630	-3.51	0.02	1.11E+07	0.34	3920	10	150	4200	spinel
1	2.00	730	-3.51	0.02	7.91E+06	0.34	3900	10	150	3000	spinel
1	2.00	830	-3.54	0.02	7.15E+06	0.34	3910	10	150	2700	spinel
1	2.00	930	-3.67	0.01	1.02E+07	0.35	4040	10	150	3800	spinel
1	2.00	1030	-4.21	0.02	1.20E+08	0.40	4650	10	150	45000	spinel
1	3.70	430									
1	3.70	530	-3.77	0.02	1.81E+07	0.36	4130	10	150	6800	amorphous
1	3.70	630	-3.70	0.02	4.27E+06	0.35	4080	10	150	1600	spinel+bixbyite
1	3.70	730	-3.76	0.02	6.56E+06	0.36	4170	10	150	2500	spinel
1	3.70	830	-3.83	0.01	9.17E+06	0.36	4200	10	150	3400	spinel
1	3.70	930	-3.98	0.02	2.14E+07	0.38	4390	10	150	8000	spinel
1	3.70	1030									
1	4.00	430	-3.64	0.02	2.36E+07	0.34	3970	10	150	8900	amorphous
1	4.00	530	-3.54	0.02	5.91E+06	0.33	3860	10	150	2200	spinel+bixbyite
1	4.00	630	-3.04	0.01	1.26E+06	0.29	3360	10	150	470	spinel+bixbyite
1	4.00	730	-3.43	0.01	4.15E+06	0.32	3740	10	150	1600	spinel+bixbyite
1	4.00	830	-3.73	0.02	7.71E+06	0.35	4040	10	150	2900	spinel+bixbyite
1	4.00	930	-3.85	0.02	1.77E+07	0.36	4170	10	150	6600	spinel
1	4.00	1030	-4.50	0.02	2.43E+08		4770	10	150	91000	spinel
1	9.00	430	-3.93	0.02	2.39E+07	0.38	4360	10	150	9000	amorphous
1	9.00	530	NA								bixbyite
1	9.00	630	-3.17	0.01	1.29E+06	0.29	3400	10	150	480	bixbyite
1	9.00	730	-3.08	0.01	1.10E+06	0.29	3390	10	150	400	bixbyite
1	9.00	830	-3.36	0.01	4.30E+06	0.32	3690	10	150	1600	bixbyite
1	9.00	930	-3.17	0.01	2.62E+06	0.30	3460	10	150	1000	bixbyite+spinel
1	9.00	1030	-4.00	0.02	4.46E+07	0.37	4340	10	150	17000	bixbyite+spinel

Appendix C: Electrical Data for Films Made From Acetylacetonate Precursors

The table contains electrical data from films made from acetylacetonate precursors and annealed for one minute in the RTA in air at temperatures ranging from 430°C to 1030°C. Some films were doped with 2% borosilicate as labeled. The error from the TCR comes from 90% confidence limits taken from the slopes of the lnR versus T curves. The TCR values are averages retrieved between 295 K and 373 K. The resistance values are normalized to 298 K. Error reported with activation energies come from 90% confidence limits that were taken from the slope of the lnR versus 1/T plots. Thicknesses of the films were estimated after a few films were measured in the SEM. These films were annealed at temperatures over 700°C. Therefore, the resistivity values are estimates for the lower temperature annealed films. Resistivity values are calculated using the normalized resistance value for 298 K. The phases identified come from XRD and TEM analysis. The Ni:Mn is listed as the ideal compositional ratio.

Borosilicate Dopant	Ni	Mn	T (°C)	TCR (%/°C)	Error (%/°C)	R_{298K} (Ω)	E_a (eV)	B (K)	Error (K)	Thick (nm)	ρ (Ωcm)	Phase
	1	2.00	430	NA								
	1	2.00	530	NA								
	1	2.00	630	-3.63	0.02	1.92E+07	0.35	4100	10	150	7200	spinel
	1	2.00	730	-3.62	0.01	1.41E+07	0.34	3970	10	150	5300	spinel
	1	2.00	830	-3.58	0.02	1.28E+07	0.34	3910	10	150	4800	spinel
	1	2.00	930	-3.90	0.02	4.68E+07	0.36	4220	10	150	18000	spinel
	1	2.00	1030							150		
	1	3.70	430	-3.99	0.01	1.29E+08	0.38	4400	10	150	48000	amorphous
	1	3.70	530	-3.86	0.01	4.87E+07	0.37	4280	10	150	18000	spinel
	1	3.70	630	-3.62	0.02	9.94E+06	0.34	3980	10	150	3700	spinel
	1	3.70	730	-3.53	0.02	1.21E+07	0.34	3910	10	150	4500	spinel
	1	3.70	830	-3.58	0.01	1.25E+07	0.34	3890	10	150	4700	spinel
	1	3.70	930	-3.81	0.02	7.85E+08	0.36	4210	10	150	290000	spinel
	1	3.70	1030	-4.29	0.02	5.54E+08	0.41	4760	10	150	210000	spinel
yes	1	3.70	430	-4.43	0.02	7.75E+08	0.42	4880	20	150	290000	spinel
yes	1	3.70	530	-4.08	0.03	3.76E+08	0.39	4510	10	150	140000	spinel
yes	1	3.70	630	-3.93	0.03	1.58E+08	0.37	4310	10	150	59000	spinel
yes	1	3.70	730	-4.11	0.02	1.18E+08	0.37	4260	10	150	44000	spinel
yes	1	3.70	830	-4.10	0.03	1.42E+08	0.38	4420	10	150	53000	spinel
yes	1	3.70	930	-4.16	0.03	2.08E+08	0.39	4580	10	150	78000	spinel
yes	1	3.70	1030	NA						150		
	1	4.00	430	-4.22	0.02	1.52E+08				150	57000	amorphous
	1	4.00	530	-4.03	0.01	5.77E+07	0.37	4340	10	150	22000	spinel
	1	4.00	630	-3.61	0.01	9.43E+06	0.35	4040	10	150	3500	spinel
	1	4.00	730	-3.63	0.02	1.23E+07	0.35	4040	20	150	4600	spinel
	1	4.00	830	-3.69	0.02	1.39E+07	0.35	4060	10	150	5200	spinel
	1	4.00	930	-4.04	0.02	5.67E+07	0.37	4340	10	150	21000	spinel
	1	4.00	1030	NA								

Appendix D: Electrical Property Data for Low Temperature Annealed Films

The table below contains electrical data from films made from acetate and acetylacetonate precursors and annealed for different times in a tube furnace in air, argon, and oxygen at temperatures ranging from 300°C to 500°C. The error from the TCR comes from 90% confidence limits taken from the slopes of the lnR versus T curves. The TCR values are averages retrieved between 295 K and 373 K. The resistance values are normalized to 298 K. Error reported with activation energies come from 90% confidence limits that were taken from the slope of the lnR versus 1/T plots. Thicknesses of the films were estimated after a few films were measured in the SEM. These films were annealed at temperatures over 700°C. Therefore, the resistivity values are estimates for the lower temperature annealed films. Resistivity values are calculated using the normalized resistance value for 298 K. The phases identified come from XRD analysis. The Ni:Mn is listed as the ideal compositional ratio.

Solution			T	Anneal	Atmosphere	TCR	Error	R_{298K}	E_a	B	Error	Thick	ρ	Phase
	Ni	Mn	(°C)	Time (hr)		(%/°C)	(%/°C)	(Ω)	(eV)	(K)	(K)	(nm)	(Ωcm)	
acetate	1	4.00	400	18.0	Ar	-3.76	0.02	1.43E+07	0.35	4050	10	230	8200	spinel
acetate	1	4.00	400	5.0	Ar	-3.90	0.02	2.09E+07	0.37	4250	10	230	12000	spinel
acetate	1	4.00	400	1.0	Ar	-3.60	0.02	2.03E+07	0.34	4000	10	230	12000	spinel
acetylacetonate	1	3.70	400	5.0	Ar	-4.06	0.02	9.50E+07	0.39	4510	10	230	55000	spinel
acetate	1	3.70	400	5.0	Ar	-3.81	0.02	5.05E+07	0.37	4270	10	230	29000	spinel
acetate	1	2.00	400	5.0	Ar	-3.81	0.02	4.65E+07	0.37	4330	10	230	27000	spinel
acetate	1	1.00	400	5.0	Ar	-3.81	0.02	1.09E+08	0.37	4310	10	230	63000	spinel
acetate	1	1.65	400	5.0	Ar	-3.93	0.02	5.62E+07	0.37	4290	10	230	32000	spinel
acetate	1	2.00	500	5.0	O_2	-3.54	0.02	8.95E+06	0.35	4050	10	230	5100	ilmenite
acetate	1	4.00	350	5.0	Ar	-3.80	0.02	5.84E+07	0.37	4310	10	230	34000	spinel
acetate	1	3.70	350	10.0	Ar	-3.75	0.02	4.08E+07	0.36	4150	10	230	23000	spinel
acetate	1	1.00	300	37.0	air	-3.98	0.02	2.02E+08	0.40	4640	10	290	150000	amorphous
acetate	1	1.00	300	112.5	air	-4.02	0.02	1.47E+08	0.39	4520	10	290	11000	spinel
acetate	1	1.00	300	127.5	air	-4.27	0.02	2.19E+08	0.41	4740	10	290	16000	spinel
acetate	1	1.65	300	37.0	air	-4.01	0.02	1.36E+08	0.40	4630	10	290	99000	amorphous
acetate	1	1.65	300	112.5	air	-4.33	0.02	1.58E+08	0.42	4850	10	290	110000	spinel
acetate	1	1.65	300	127.5	air	-4.30	0.02	1.64E+08	0.41	4780	10	290	120000	spinel
acetate	1	4.00	300	37.0	air	-3.45	0.02	4.56E+07	0.34	3890	10	290	33000	amorphous
acetate	1	4.00	300	112.5	air	-4.03	0.02	6.02E+07	0.38	4370	10	290	44000	spinel
acetate	1	4.00	300	127.5	air	-3.84	0.02	4.98E+07	0.36	4150	10	290	36000	spinel
acetylacetonate	1	3.70	300	37.0	air	-4.07	0.02	2.06E+08	0.40	4660	10	290	150000	amorphous
acetate	1	3.70	300	112.5	air	-4.19	0.02	1.97E+08	0.41	4710	10	290	140000	spinel
acetate	1	3.70	300	127.5	air	-4.30	0.02	NA						

Appendix E: Electrical Property Data for Aged Low Temperature Annealed Films

The table contains electrical data from films made from acetate and acetylacetonate precursors and annealed for different times in a tube furnace in air and argon, at temperatures ranging from 300°C to 500°C. The films were then aged in air either at 150°C or 400°C for different times. The error from the TCR comes from 90% confidence limits taken from the slopes of the lnR versus T curves. The TCR values are averaged between 295 K and 373 K. The resistance values are normalized to 298 K. Error reported with activation energies come from 90% confidence limits that were taken from the slope of the lnR versus 1/T plots. Thicknesses of the films were estimated after a few films were measured in the SEM. These films were annealed at temperatures over 700°C. Therefore, the resistivity values are estimates for the lower temperature annealed films. Resistivity values are calculated using the normalized resistance value for 298 K. The phases identified come from XRD analysis. The Ni:Mn is listed as the ideal compositional ratio.

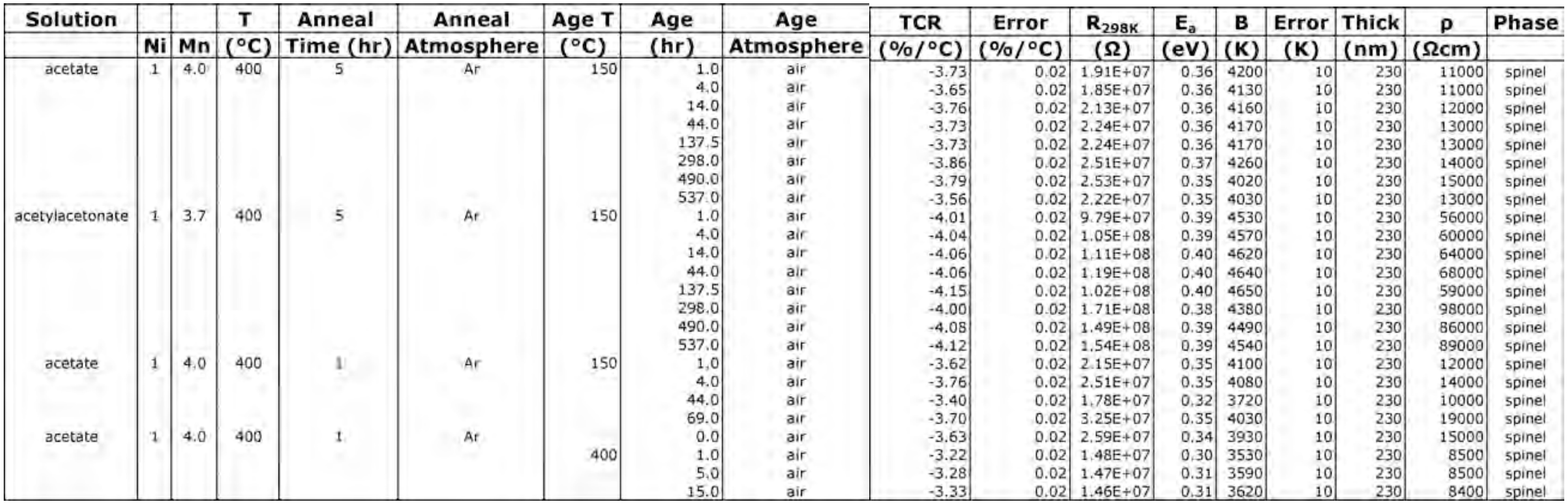

Solution			T	Anneal	Anneal	Age T	Age	Age	TCR	Error	R_{298K}	E_a	B	Error	Thick	ρ	Phase
	Ni	Mn	(°C)	Time (hr)	Atmosphere	(°C)	(hr)	Atmosphere	(%/°C)	(%/°C)	(Ω)	(eV)	(K)	(K)	(nm)	(Ωcm)	
acetate	1	4.0	400	5	Ar	150	1.0	air	-3.73	0.02	1.91E+07	0.36	4200	10	230	11000	spinel
							4.0	air	-3.65	0.02	1.85E+07	0.36	4130	10	230	11000	spinel
							14.0	air	-3.76	0.02	2.13E+07	0.36	4160	10	230	12000	spinel
							44.0	air	-3.73	0.02	2.24E+07	0.36	4170	10	230	13000	spinel
							137.5	air	-3.73	0.02	2.24E+07	0.36	4170	10	230	13000	spinel
							298.0	air	-3.86	0.02	2.51E+07	0.37	4260	10	230	14000	spinel
							490.0	air	-3.79	0.02	2.53E+07	0.35	4020	10	230	15000	spinel
							537.0	air	-3.56	0.02	2.22E+07	0.35	4030	10	230	13000	spinel
acetylacetonate	1	3.7	400	5	Ar	150	1.0	air	-4.01	0.02	9.79E+07	0.39	4530	10	230	56000	spinel
							4.0	air	-4.04	0.02	1.05E+08	0.39	4570	10	230	60000	spinel
							14.0	air	-4.06	0.02	1.11E+08	0.40	4620	10	230	64000	spinel
							44.0	air	-4.06	0.02	1.19E+08	0.40	4640	10	230	68000	spinel
							137.5	air	-4.15	0.02	1.02E+08	0.40	4650	10	230	59000	spinel
							298.0	air	-4.00	0.02	1.71E+08	0.38	4380	10	230	98000	spinel
							490.0	air	-4.08	0.02	1.49E+08	0.39	4490	10	230	86000	spinel
							537.0	air	-4.12	0.02	1.54E+08	0.39	4540	10	230	89000	spinel
acetate	1	4.0	400	1	Ar	150	1.0	air	-3.62	0.02	2.15E+07	0.35	4100	10	230	12000	spinel
							4.0	air	-3.76	0.02	2.51E+07	0.35	4080	10	230	14000	spinel
							44.0	air	-3.40	0.02	1.78E+07	0.32	3720	10	230	10000	spinel
							69.0	air	-3.70	0.02	3.25E+07	0.35	4030	10	230	19000	spinel
acetate	1	4.0	400	1	Ar		0.0	air	-3.63	0.02	2.59E+07	0.34	3930	10	230	15000	spinel
						400	1.0	air	-3.22	0.02	1.48E+07	0.30	3530	10	230	8500	spinel
							5.0	air	-3.28	0.02	1.47E+07	0.31	3590	10	230	8500	spinel
							15.0	air	-3.33	0.02	1.46E+07	0.31	3620	10	230	8400	spinel